



저작자표시-비영리-변경금지 2.0 대한민국

이용자는 아래의 조건을 따르는 경우에 한하여 자유롭게

- 이 저작물을 복제, 배포, 전송, 전시, 공연 및 방송할 수 있습니다.

다음과 같은 조건을 따라야 합니다:



저작자표시. 귀하는 원저작자를 표시하여야 합니다.



비영리. 귀하는 이 저작물을 영리 목적으로 이용할 수 없습니다.



변경금지. 귀하는 이 저작물을 개작, 변형 또는 가공할 수 없습니다.

- 귀하는, 이 저작물의 재이용이나 배포의 경우, 이 저작물에 적용된 이용허락조건을 명확하게 나타내어야 합니다.
- 저작권자로부터 별도의 허가를 받으면 이러한 조건들은 적용되지 않습니다.

저작권법에 따른 이용자의 권리는 위의 내용에 의하여 영향을 받지 않습니다.

이것은 [이용허락규약\(Legal Code\)](#)을 이해하기 쉽게 요약한 것입니다.

[Disclaimer](#)

Doctoral Thesis

Engineering of Hybrid Materials
for Self-Powered Flexible Sensors

Young-Eun Shin

Department of Energy Engineering

Graduate School of UNIST

2020

Engineering of Hybrid Materials for Self-Powered Flexible Sensors

Young-Eun Shin

Department of Energy Engineering

Graduate School of UNIST

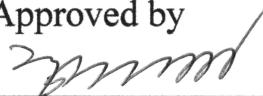
Engineering of Hybrid Materials for Self-Powered Flexible Sensors

A thesis/dissertation
submitted to the Graduate School of UNIST
in partial fulfillment of the
requirements for the degree of
Doctor of Philosophy

Young-Eun Shin

06. 12. 2020

Approved by



Advisor

Hyunhyub Ko

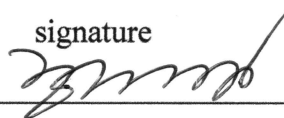
Engineering of Hybrid Materials for Self-Powered Flexible Sensors

Young-Eun Shin

This certifies that the thesis/dissertation of Young-Eun Shin is approved.

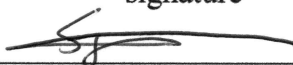
06. 12. 2020

signature



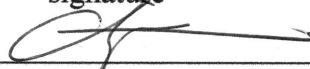
Advisor: Hyunhyub Ko

signature



Seok Ju Kang

signature



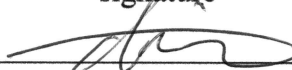
Han Gi Chae

signature



Chang Young Lee

signature



Moon Kee Choi

Abstract

Along with the 4th industrial revolution, the great advance in wearable electronics has led a new paradigm in our life. Especially, wearable sensor technology has received great attention as promising candidates to improve the quality of life by realizing the “Internet of Things” which can be utilized in daily healthcare, intelligent control, daily activity monitoring, and human-machine interface systems. The ideal wearable devices require several characteristics providing light weight, flexible, unobtrusive, autonomously powered for the convenience of user and sustainable uses. Although various emerging technologies have been suggested to meet these requirements, there are still challenges for highly flexible and unobtrusive forms, multifunctionality, and sustainable uses, which are directly related to widespread practical applications. In response to these requirements, several approaches to explore functional materials and to design the effective structures for advanced sensor performances with sustainable uses, high sensitivity, and multifunctionality. For sustainable uses, self-powered sensing system can be developed by triboelectric/piezoelectric/pyroelectric effect, which can rule out any problems with power sources. For wearable and flexible form factors, textile and extremely thin films, which are mountable and attachable on the human body, are used instead of conventional obtrusive devices, improving the wearing sensing of devices. Moreover, the selection of multifunctional materials and modification of material characteristics can realize multifunctionality which can respond to different stimuli (pressure and temperature) simultaneously. Furthermore, soft/hard and organic/inorganic hybrid materials can be used for effective design of high performance wearable sensor by distribution control in dissimilar materials, which is attributed to effectively localized strain and large contrast of dielectric properties. Therefore, self-powered wearable sensors can be developed with functional materials, unique design and novel approach for characteristic modification, which can provide a promising platform to realize ideal wearable sensors for future applications such as daily healthcare, intelligent control, daily activity monitoring, and human-machine interface systems.

In this thesis, we suggest the strategy for advanced sustainable wearable sensors with better wearing sensation, multimodality, and enhanced sensory functions through structure design and modification of material characteristics. Firstly, we briefly summarize the fundamental working principles, the latest research trends, and potential applications in Chapter 1. In Chapter 2, we demonstrate as-spun P(VDF) fiber-based self-powered textile sensors with high sensitivity, mechanical stability, and washing durability. In Chapter 3, we introduce multimodal wearable sensors without signal interference based on triboelectric and pyroelectric effect, which is attributed to controllable polarity of P(VDF-TrFE) *via* ferroelectric polarization. In Chapter 4, we suggest a novel method for high performance of triboelectric sensors based on alternating P(VDF-TrFE)/BaTiO₃ multilayer nanocomposites, which is attributed to the efficient stress concentration and large contrast of dielectric properties. Lastly, we summarize this thesis with future prospects in Chapter 5.

Contents

Abstract	1
Contents	3
List of Figures	5
List of Tables	14
Nomenclature	15
 Chapter 1. Introduction	 17
1.1 Wearable sensors	20
- Fiber/textile-based sensors	20
- Thin film-based skin-attachable sensors	20
1.2 Working mechanisms of self-powered wearable sensors	22
1.2.1 Working principle for mechanical stimuli	22
- Triboelectric effect	22
- Piezoelectric effect	23
1.2.2 Working principle for temperature	23
- Pyroelectric effect	23
- Thermoelectric effect	24
1.3 Ferroelectric polymer-based self-powered sensors	26
1.3.1 Piezoelectric devices based on ferroelectric polymer	26
1.3.2 Pyroelectric devices based on ferroelectric polymer	27
1.3.3 Triboelectric devices based on ferroelectric polymer	28
1.4 Applications of self-powered wearable sensors	32
- Healthcare	32
- Biometric security systems	32
1.5 Challenges of current self-powered wearable sensors	34
 Chapter 2. Self-powered textile sensors with programmable stitch patterns based on PVDF fibers for realization of practical uses	 36
2.1 Introduction	36
2.2 Experimental details	39
2.3 Results and discussion	40
2.4 Conclusions	64

Chapter 3. Triboelectric/pyroelectric multimodal sensors with decoupled pressure and temperature multiple stimuli via ferroelectric polarization -----	65
3.1 Introduction -----	65
3.2 Experimental details -----	67
3.3 Results and discussion -----	68
3.4 Conclusions -----	98
 Chapter 4. Alternating PVDF-TrFE/BaTiO ₃ multilayer nanocomposites for enhanced triboelectric performances -----	99
4.1 Introduction -----	99
4.2 Experimental details -----	101
4.3 Results and discussion -----	103
4.4 Conclusions -----	126
 Chapter 5. Summary and future perspective -----	127
References -----	129
Appendix A: list of achievements -----	150
Acknowledgements -----	152

List of Figures

Chapter 1.

Figure 1.1. Recent advances in wearable electronics with the fourth industrial revolution. (left) History of industrial revolution; 1st revolution with mechanization, 2nd revolution with mass production, 3rd revolution with automation, 4th revolution with cyber physical system. (right) various future wearable electronics. Reproduced from Ref.[25-34].

Figure 1.2. Summarized key requirements for advanced wearable tactile sensors on the aspects of functionality and sensing capability. (Digital free images, Reproduced from Ref.[35])

Figure 1.3. Research strategies to achieve the required technologies for advanced wearable sensors in terms of (a) materials (*J. Mater. Chem. A* **2017**, 5, 3091.; *Chem. Soc. Rev.* **2019**, 48, 1194.), (b) structures (*Nature* **2019**, 569, 698.; *Nat. Mater.* **2013**, 12, 938.; *Adv. Mater.* **2018**, 30, 1803388.), sensing target stimuli (*Nature* **2018**, 555, 83.; *Nat. Biomed. Eng.* **2018**, 2, 687.; *Nat. Electron.* **2018**, 1, 183.; *Adv. Mater.* **2019**, 1905527.), and working mechanism (*Adv. Mater.* **2019**, 31, 1802898.).

Figure 1.4. Wearable flexible sensors. (a-c) fiber/textile based sensor; (a) integration of sensor in the commercial textiles (*Adv. Mater.* **2017**, 29, 1703700.), (b) woven sensor based on functional fibers (*ACS Nano* **2015**, 9, 6394.), (c) knitted sensor based on functional fibers (*ACS Nano* **2017**, 11, 9490.). (d-g) thin-film based skin-attachable sensors; (d) tattoos-like attachable sensor by transfer method (*Science* **2011**, 333, 838.), (e) highly stretchable body-attachable sensor based on organic materials (*Nature* **2013**, 499, 458.), (f) highly sensitive attachable sensors with microstructures (*Nat. Commun.* **2013**, 4, 1.), (g) sustainable wearable sensor based on triboelectric effect (*Adv. Mater.*, **2014**, 26, 5851.).

Figure 1.5. Working mechanism of self-powered wearable sensors; (a) Triboelectric, (b) Piezoelectric (*Chem. Soc. Rev.* **2019**, 48, 1787.), (c) Pyroelectric (*Chem. Soc. Rev.* **2019**, 48, 1787.), (d) Thermoelectric effect.

Figure 1.6. Schematics of representative ferroelectric polymer, PVDF. (a) Chin conformation for the α and β phases of PVDF (OMNEXUS home page, <https://omnexus.specialchem.com/selection-guide/polyvinylidene-fluoride-pvdf-plastic>, accessed: May 2020.). (b) D-E loops and domain structures of ferroelectric and paraelectric states (*Polymer* **2012**, 53, 728). (c) Electrical poling procedure of ferroelectrics; i. Initially random arrangement of domains, ii. Aligned domains under the applied electric field, iii. A remnant polarisation under removing the electric field (*J. Mater. Chem. A* **2017**, 5, 3091.).

Figure 1.7. PVDF and its copolymer-based self-powered sensors. (a-c) High performance of piezoelectric sensors with (a) composite materials (*ACS Nano* **2014**, 8, 2766.), (b) micropatterned structure (*Adv. Funct. Mater.* **2015**, 25, 3203.), and (c) textile form (*Energy Environ. Sci.* **2014**, 7, 1670.). (d-f) Enhanced pyroelectric sensing performances with (d, e) effective thermal energy absorption (*Adv. Energy Mater.* **2015**, 5, 1401891.; *Adv. Mater.* **2014**, 26, 765.), and (f) material modification (*Adv. Funct. Mater.* **2017**, 27, 1700702.). (g-i) Performance-modulated triboelectric sensors with (g) microstructures (*ACS Nano* **2018**, 12, 3964), (h) composite materials (*Adv. Energy Mater.* **2017**, 7, 1600988.), and (i) ferroelectric polarisation (*Adv. Funct. Mater.* **2016**, 26, 3067.).

Figure 1.8. Applications based on self-powered wearable sensors; daily healthcare for (a) pulse pressure detection (*Nat. Biomed. Eng.* **2018**, 2, 687.) and (b) real-time gait patterns monitoring (*ACS Nano* **2018**, 12, 4045.), biometric security systems with (c) voice patterns (*Sci. Adv.* **2018**, 4, eaas8772.) and (d) fingerprint (*Nat. Commun.* **2018**, 9, 1.).

Figure 1.9. Summary of this thesis; engineering of hybrid materials for self-powered flexible sensors (*J. Mater. Chem. A* **2018**, 6, 22879.; *Nano Energy* **2020**, 104671.).

Chapter 2.

Figure 2.1. PVDF stitch-based triboelectric textile sensors. (a) Schematic illustration of the fabrication procedure of textile sensors by a sewing machine. (b–c) Photographic and SEM images of PVDF-based stripe stitch; (d, g) SEM images of the twisted 5-ply PVDF threads composed of mono fibers of diameter $\sim 50\ \mu\text{m}$. Photographic images of (e–f) PVDF-based embroidery, (h) PVDF-based embroidered line stitches, and (i) PVDF-based letter stitches. (j–m) Photographic images of textile sensor demonstrating effects of different mechanical forces, including folding, stretching, twisting, and crumpling.

Figure 2.2. A schematic illustration of the lab scale dry-jet wet spinning procedure.

Figure 2.3. Mechanical characteristics of dry-jet wet-spun PVDF in this work; (a) Strain-stress curves, and (b) comparison of tensile modulus and strength based on this work and previous reports.

Figure 2.4. Working mechanism and triboelectric output performances of the PVDF stitch-based textile sensor. (a) Photographic and (b) optical cross-section images of the textile sensor. SEM images of (c) the nylon fabric for a positive triboelectric object and (d) PVDF stitch for a negative triboelectric object. (e) Schematic illustration of triboelectric charge generation and electron flow mechanism between the PVDF stitch and nylon fabric. Triboelectric output (f) current and (g) voltage under 9.8 N.

Figure 2.5. Triboelectric output current profiles of PVDF stitch textile sensor with relative contact-separation motion to different materials.

Figure 2.6. Evaluation of the PVDF stitch-based textile sensor for self-powered force sensing and washing durability. (a) A photographic image of the PVDF stitch for force sensing; the red rectangular region is under pressure (area $3 \times 10 \text{ mm}^2$) (scale bar: 10 mm). (b) Triboelectric output current as a function of time under different applied pressures. (c) Linear fitting between the triboelectric current variations and the applied pressure (326 Pa to 326 kPa). (d) A photographic image of the PVDF for the embroidery stitch washing durability test (scale bar: 10 mm). (e) Triboelectric output current of the device after 50 cycles of washing. (f) Linear fitting between the triboelectric current retention ratio and the number of washing times.

Figure 2.7. Evaluation of the PVDF stitch-based textile sensor for self-powered force sensing; (a) Triboelectric output voltage as a function of time at different pressures applied on the device. (b) Linear fitting between the triboelectric voltage variations and the applied pressure (326 Pa ~ 326 kPa).

Figure 2.8. Triboelectric output signals in the low-pressure region (a) Triboelectric output current as a function of time and (b) the applied pressures from 326 Pa to 3.26 kPa in the low-pressure region.

Figure 2.9. Comparison of the detectable pressure range of the results achieved in this work with previously reported triboelectric pressure sensor.

Figure 2.10. Washing durability of PVDF stitch textile sensor; Demonstration of the washing environment with commercial detergent by magnetic stirring.

Figure 2.11. Evaluation of the PVDF stitch-based textile sensor for mechanical stability. (a, b) Triboelectric output current of the device after 100 cycles of mechanical deformation by folding and twisting. (c, d) Linear fitting between the triboelectric current retention ratio and the number of mechanical deformation times.

Figure 2.12. Experimental image of contact-separation motion between PVDF stitch and nylon fabric.

Figure 2.13. Outstanding triboelectric output performance of the PVDF stitch-based textile sensor. Comparison of the output currents from the PVDF stitch-based device with (a) PVDF film and (b) other commercial thread stitch. (c) The output current independent of the supportive stitch and substrate fabric.

Figure 2.14. Comparison of both types of PVDF sensor. (a, b) Photographic images of (a) the stitch-based sensor and (b) the film-based sensor.

Figure 2.15. Real-time detection of different body motions and hand gestures using the self-powered PVDF-textile sensor. (a) A schematic illustration of the working mechanism of the PVDF stitch-based textile sensor attached to the joint pad. (b) Photographic images and intrinsic output current signals obtained by detecting various motions of the wrist, elbow, ankle, and knee; the body motion monitoring patch ($40 \times 60 \text{ mm}^2$) was composed of 3-lines of stitch with $3 \times 45 \text{ mm}^2$. (c, d) Photographic images and intrinsic output current signals by detecting (c) various body motions (the wrist, elbow, ankle, and knee) and (d) various hand gestures for different numbers; the smart glove was composed of 6-lines of stitch with $3 \times 50 \text{ mm}^2$. (e) Demonstration of the self-powered human-system interaction interface with Morse codes by touching the triboelectric stitch with finger, representing a word “UNIST.”

Figure 2.16. Working mechanism of PVDF stitch-based textile sensor as a body-motion sensor; Schematic illustration of triboelectric charge generation and electrons flow mechanism with single electrode system.

Figure 2.17. Real-time detection of body motion with different strength; (a) Output current signals from wrist movements with weak and strong motion. (b) Output current signals from elbow movements with weak and strong motion.

Figure 2.18. Self-powered foot pressure mapping based on the PVDF stitch sensor array. (a) A schematic illustration of the PVDF stitch sensor array device. (b) Photograph of 3×4 pixel arrays of PVDF stitch sensor with fish-shaped embroidery; the foot pressure sensor ($150 \times 230 \text{ mm}^2$) was composed of 12 pixels with $10 \times 30 \text{ mm}^2$. (c) Schematics of walking motions on PVDF stitch sensor array and their corresponding contour mapping images.

Figure 2.19. Real-time detection of pulse pressure using the self-powered PVDF-textile sensor. (a) Photographic images of the fashionable garment-type triboelectric sensor with arbitrary stitch patterns for pulse pressure detection; the pulse pressure sensor ($70 \times 30 \text{ mm}^2$) was composed of 11 diamond patterned stitches ($20 \times 5 \text{ mm}^2$). (b) Real-time monitoring of the pulse pressure and (c) expanded pulse wave consisting of three peaks corresponding to the pulse pressure (P_1) and reflected wave pressures from the hand (P_2) and lower body (P_3). (d–e) Variation in the pulse pressure wave before and after physical exercise.

Figure 2.20. Comparison of augmentation index (AI_r) before and after physical exercise.

Chapter 3.

Figure 3.1. Structural and PFM analysis of P(VDF-TrFE) film. (a) FT-IR result for the β phase of P(VDF-TrFE) (b) XRD result for the β phase (110/200) of P(VDF-TrFE). (c-e) PFM images of P(VDF-TrFE) film with different direction of bias. (c) Topology, (d) phase, and (e) amplitude images of P(VDF-TrFE) films; the white dotted square indicates positively (negatively) poled area by applying + 20 V (−20 V).

Figure 3.2. Switchable triboelectric polarity of identical P(VDF-TrFE) film by electrical polarization. (a) Schematic illustration of P(VDF-TrFE) films with different surface charge depending on the direction of dipoles. (b) Output current and voltage of surface charge-tuned P(VDF-TrFE) films. (c) KPFM images of the different surface charge potential distribution of non-, negatively and positively poled P(VDF-TrFE). (d) Modified triboelectric series with surface-charge-tuned P(VDF-TrFE) by ferroelectric polarization.

Figure 3.3. Triboelectric charge density of the polarization-tuned PVDF-TrFE films; (a) negatively, (b) positively polarized films.

Figure 3.4. Evaluation for the duration of the tuned triboelectric performances. Triboelectric output current right after and 24 h after electrical poling from (a) negatively polarized and (b) positively polarized PVDF-TrFE films.

Figure 3.5. Comparison of triboelectric and piezoelectric output performances under the same pressure with 98 kPa.

Figure 3.6. Identification of charges from both surfaces of P(VDF-TrFE) film with different polarization conditions. (a) Schematic procedure illustration of measurement of opposite bottom surface of P(VDF-TrFE) film. Output current of top surface of (b) non poled, (c) negatively poled, and (d) positively poled P(VDF-TrFE) films. Output current of bottom surface of (e) non poled, (f) negatively poled, and (g) positively poled P(VDF-TrFE) films.

Figure 3.7. Triboelectric working mechanism and output performances of the inversely polarized P(VDF-TrFE) based sensor. (a) Schematic illustration of triboelectric charge generation and electron flow mechanism between the inversely polarized P(VDF-TrFE) films. Triboelectric output (b) current and (c) voltage under 98 kPa. (d) Triboelectric output current as a function of time under different applied pressures. (e) Linear fitting between the triboelectric current variations and the applied pressure (98 Pa to 98 kPa).

Figure 3.8. Evaluation of surface charge tuned P(VDF-TrFE) based triboelectric sensor for self-powered force sensing and output power performances. (a) Triboelectric output voltage as a function

of time under different applied pressures. (b) Linear fitting between the triboelectric voltage variations and the applied pressure (98 Pa to 98 kPa). (c) Triboelectric output variations of current density, voltage, and power density with an external load resistance from 103Ω to 109Ω . (d) Rectified triboelectric voltage connected with rectifier and the inset image of capability for lighting LED driven by self-powered triboelectric sensor.

Figure 3.9. Pyroelectric working mechanism and performances of the inversely polarized P(VDF-TrFE) based sensor. (a) Schematic illustration of pyroelectric charge generation and electron flow mechanism between the inversely polarized P(VDF-TrFE) films. Pyroelectric output currents from (b) heating and (c) cooling states. (d) Pyroelectric output current as a function of time under different applied temperatures (ΔT) from -20 to 20 °C. (e) Linear fitting between the pyroelectric current variations and the applied temperatures.

Figure 3.10. Highly responsive pyroelectric performance under real-time temperature gradient. (a, b) Pyroelectric output current as a function of time under gradually (a) decreased temperature ($5\text{ °C} < \Delta T < 20\text{ °C}$) and (b) increased temperature ($-20\text{ °C} < \Delta T < -5\text{ °C}$).

Figure 3.11. Evaluation of the pyroelectric performances of the inversely polarized P(VDF-TrFE)-based sensors with different distances between the sensor and thermal source. (a) Pyroelectric output current as a function of time under different distances. (b) Comparison of pyroelectric performances from different distances.

Figure 3.12. Pyroelectric output performances depending on the device compositions. Pyroelectric output signals under different temperature from (a-c) standard device composed of positively and negatively polarized P(VDF-TrFE) films as a bottom and top components, respectively, and (d-f) device with non-polarized films. Opposite directional pyroelectric signals from (g-i) reverse connection and (j-l) opposite composition of device compared to ones from standard device in forward connection.

Figure 3.13. Comparison of triboelectric and pyroelectric performances from different compositions of P(VDF-TrFE) based sensors. (a) Schematic illustration of diverse devices composed with two P(VDF-TrFE) films; non poled, negatively poled, and positively poled P(VDF-TrFE) films. Output currents of different composition of (b) triboelectric and (d) pyroelectric devices based on surface charge-tuned P(VDF-TrFE) films. (c) Triboelectric and (e) pyroelectric output currents as a function of time with different composition of devices.

Figure 3.14. Comparison of triboelectric performances from different compositions of P(VDF-TrFE) based sensors. (a) Output voltages of different composition of triboelectric devices based on surface

charge-tuned P(VDF-TrFE) films. (b) Triboelectric output voltages as a function of time with different composition of devices.

Figure 3.15. KPFM of various combinations before and after contact-separation with different compositions of P(VDF-TrFE) films; (a) both non polarized films, (b) both negatively polarized films and (c) oppositely polarized films (negatively and positively poled films).

Figure 3.16. Pyroelectric coefficient with different combinations of sensors.

Figure 3.17. Working mechanism of multimodal sensing performance of inversely polarized P(VDF-TrFE) based sensors. (a) Schematic illustration of both triboelectric and pyroelectric charge generation and electron flow mechanism between the inversely polarized P(VDF-TrFE) films. Multimodal output currents and enlarged peaks from (b) heating and (c) cooling states under 98 Pa; the gradual pyroelectric signals are cut by the followed next spike triboelectric signals.

Figure 3.18. Decoupled signals of multimodal sensor under simultaneously applied pressure and temperature. (a) Schematic illustration of multimodal sensing of inversely polarized P(VDF-TrFE) based sensor. (b-e) Multimodal output currents as a function of time and enlarged each peak to respond the simultaneous stimuli; the output currents depending on (b, c) the pressure under $-20\text{ }^{\circ}\text{C}$ (ΔT) and (d, e) the temperature under 490 Pa.

Figure 3.19. Pressure-dependence of the multimodal output signals under different temperature changes; (a-c) heating and (d-f) cooling.

Figure 3.20. Temperature-dependence of the multimodal output signals from (a-d) heating and (e-h) cooling process under different pressures.

Figure 3.21. Simultaneous monitoring of weak pulse pressure from carotid artery and different temperatures of finger touch. (a) Photographic images of real-time detection of pulse pressure with the inversely polarized P(VDF-TrFE) based sensor. (b) Real-time monitoring of the pulse pressure and (c) expanded pulse wave with three peaks (P_1 , P_2 , P_3). (d, e) Variation in the pulse pressure waves before and after physical exercise. (f, h) Schematic illustrations of finger touch monitoring from warm and cold hands with each infrared image of hand. Real-time monitoring of (g) the warm and (i) cold finger touches and enlarged responsive signal consisting of two peaks from finger pressure (I_1) and temperature (I_2).

Figure 3.22. Validation of the real-time detection of pulse pressure. (a) Comparison of the pulse-pressure responsive signals from inversely polarized, non-polarized sensors and electrode only; the enlarged responsive signals from (b) inversely polarized PVDF-TrFE sensor and (c) non polarized PVDF-TrFE sensor.

Figure 3.23. Comparison of augmentation index (AIr) before and after physical exercise.

Chapter 4.

Figure 4.1. Multilayered TESs with aligned BTO NPs. (a) Schematic of the multilayered PVDF-TrFE/BTO based TESs. (b) Cross-sectional SEM image of the 4-layered film. (c) Photo of the 4-layered PVDF-TrFE/BTO film. (d) Working mechanism of the TESs with multilayered ferroelectric materials. (e) Output current density and voltage of multilayered TESs (4-layered film).

Figure 4.2. (a) Schematic illustrating the fabrication process of the multilayered PVDF-TrFE/BTO film. (b) SEM image of the BTO NPs coated on the PVDF-TrFE layer.

Figure 4.3. (a) X-ray diffraction (XRD) result of the PVDF-TrFE film with strong β -phase (110/200); (b) XRD patterns of the tetragonal BTO NPs; and (c) FT-IR spectrum of PVDF-TrFE and PVDF-TrFE/BTO film.

Figure 4.4. (a) Schematic of the three different TESs: non-poled PVDF-TrFE, poled PVDF-TrFE, and poled PVDF-TrFE/BTO. Comparison of (b) the output current density and (c) voltage of the above three different types of 4-layered films under a vertical pressure of 98 kPa with 2 Hz. (d) Surface potential of different types of films measured by SKPM.

Figure 4.5. (a) SEM images of BTO interlayers coated on the PVDF-TrFE layer with a different surface density of BTO NPs; (b) output current density and (c) dielectric constant for the 4-layered PVDF-TrFE/BTO films with a different surface density. (d) Average size of BTO NPs at different surface densities of BTO NPs; ImageJ was used to approximate the surface densities.

Figure 4.6. (a) Output current density and (b) voltage of the multilayered PVDF-TrFE films with and without BTO interlayers by increasing the number of layers, which range from 1 to 7. (c, d) Dielectric constant of the poled PVDF-TrFE/BTO for a various number of layers.

Figure 4.7. Comparison of (a) the output current density and (b) voltage of the 1-layered (black) and 4-layered PVDF-TrFE/BTO film (red).

Figure 4.8. (a) Schematic of the three different types of samples with the same thickness: a PVDF-TrFE film, single PVDF-TrFE/BTO composite, and multilayered PVDF-TrFE/BTO film. Comparison of (b) the output current density and voltage under a vertical pressure of 98 kPa with 2 Hz. (c) FEM simulations of electric field distribution in the single and multilayered PVDF-TrFE/BTO composite films under Dirichlet boundary condition. (d) Comparison of the dielectric constant of the three different types of films.

Figure 4.9. Thermogravimetric analysis (TGA) of the PVDF-TrFE and the PVDF-TrFE/BTO film.

Figure 4.10. The contour plot of simulated electric field distribution in the single PVDF-TrFE/BTO composite and the multilayered PVDF-TrFE/BTO film having plate electrodes.

Figure 4.11. FEM Simulations of interfacial polarization in the single PVDF-TrFE/BTO composite and multilayered PVDF-TrFE/BTO film using Gauss's law under Dirichlet boundary condition.

Figure 4.12. Simulations of capacitance in the single PVDF-TrFE/BTO composite and multilayered PVDF-TrFE/BTO film at frequency ranging from 10^2 – 10^5 Hz.

Figure 4.13. Dielectric loss of poled films for pure PVDF-TrFE, single PVDF-TrFE/BTO composite, and multilayered PVDF-TrFE/BTO composite films.

Figure 4.14. (a) Schematics of the three different types of samples: single PVDF-TrFE, single PVDF-TrFE/BTO composite, multilayered PVDF-TrFE/BTO. (b) Piezoelectric current density of the three different types of films. All the samples had the same thickness.

Figure 4.15. Schematic and output current density of the TESs (a) in the forward connection and (b) in the reverse connection.

Figure 4.16. (a) Output current and (b) voltage of the four-layered PVDF-TrFE/BTO film depending on the applied pushing force up to 98 kPa. (c) Output voltage and current density at loading resistances ranging from 1 k Ω to 750 M Ω . (d) Optimized maximum output power density at 100 M Ω .

Figure 4.17. Stability of poled PVDF-TrFE/BTO multilayer film for (a) low-pressure of 0.98 kPa (b) medium-pressure of 49 kPa, and (c) high-pressure of 117 kPa.

Figure 4.18. (a) Rectified voltage of the four-layered PVDF-TrFE/BTO film and (b) a photograph showing the ability of TESs to drive LEDs.

Figure 4.19. (a) Schematic of the multilayered PVDF-TrFE/BTO TES device. Current signals and photographs of the multilayered TESs in response to (b) radial artery pressure on the wrist and (c) carotid pulse pressure on the neck. (d) Current signals and photographs of the multilayered TESs in response to human breath on the area below the nose. (e) Measurement system for acoustic sound wave detection. (f) Voltage signals of three different types of TESs as a function of a sound frequency. (g) Time-dependent sound waveforms and short-time Fourier transform (STFT) signals of the sound source ("Triboelectric sensor") and three types of TES: non-poled and poled PVDF-TrFE TES, and poled PVDF-TrFE/BTO TES.

Figure 4.20. Voltage signals of a poled multilayered PVDF-TrFE/BTO sensor as a function of sound pressure level.

List of Tables

Table 2.1. Comparison of mechanical characteristics of the results achieved in this work with previously reported as-spun PVDF fibers.

Table 2.2. Comparison of detection range of the results achieved in this work with previously reported textile-based sensors.

Table 2.3. Comparison of detection range and sensitivity of the results achieved in this work with previously reported triboelectric pressure sensors.

Table 2.4. Comparison of fabrication conditions and washability of the results achieved in this work with previously reported textile-based sensors.

Table 3.1. Comparison of triboelectric sensitivity and output performances of the results achieved in this work with previously reported self-powered sensors.

Table 3.2. Comparison of multimodal sensing performances of the results achieved in this work with previously reported multimodal sensors.

Table 4.1. Summary of thin-film based triboelectric sensors and their pressure sensitivities.

Nomenclature

1D	One dimensional
2D	Two dimensional
AFM	Atomic force microscope
Al	Aluminum
AI	Artificial intelligence
BPM	Beats per minute
CNT	Carbon nanotube
CPD	Contact potential difference
Cu	Copper
DAI	Diastolic augmentation index
DCEFM	Dynamic-contact electrostatic force microscopy
DMF	N,N-dimethylformamide
E-textile	Electronic textile
FBI	Federal Bureau of Investigation
FEM	Finite element method
FM	Frequency modulation
FE-SEM	Field emission scanning electron microscopy
FTIR	Fourier transform infrared
HOPG	Highly oriented pyrolytic graphite
IoT	Internet of Thing
KPFM	Kelvin probe force microscope
LED	Light-emitting device
NPs	Nanoparticles
OC	Open-circuit
PAI	Pressure augmentation index
PCB	Printed circuit boards
PDMS	Polydimethylsiloxane
PET	Poly(ethylene terephthalate)
PFM	Piezoresponse force microscopy
PI	Polyimide
PTFE	Poly(tetrafluoroethylene)
PU	Poly(urethane)

PVDF	Poly(vinylidene fluoride)
PVDF-CTFE	Poly(vinylidene fluoride-chlorotrifluoro ethylene)
PVDF-HFP	Poly(vinylidene fluoride-co-hexafluoropropylene)
PVDF-TrFE	Poly(vinylidene fluoride-co-trifluoroethylene)
PVDF-TrFE-CTFE	Poly(vinylidene fluoride- trifluoroethylene-chlorotrifluoroethylene)
PVP	Polyvinylpyrrolidone
RT	Room temperature
SC	Short-circuit
SEM	Scanning electron microscopy
SKPM	Scanning kelvin probe microscopy
SPL	sound pressure levels
STFT	Short-time Fourier transform
TENG	Triboelectric nanogenerator
TES	Triboelectric sensor
TGA	Thermogravimetric analysis
XRD	X-ray diffraction

Chapter 1. Introduction

Wearable sensing technologies have evolved to become one of the biggest industries in the world along with the recent development of the “Internet of Things (IoT)”, which interconnects the user with surrounding smart devices and communicates for the quality of life. The rapid development of wearable technology can be used for tracking information on real time basis and bring a new paradigm in daily life healthcare,¹⁻³ daily activity monitoring,^{2, 4} intelligent control,⁵ and human-machine interface systems⁶ (**Figure 1.1**). The ideal wearable devices require characteristics providing light weight, flexible, unobtrusive, autonomously powered for the convenience of user and sustainable uses.^{3, 7-8} However, current wearable devices mostly in the forms of glasses, wristbands, or watches, which are composed of obtrusive, hard supports or additional flexible strips to be mounted on the human body, have restrictions in practical uses and problems caused by mechanical and thermal loading under long-time uses.⁹ Moreover, conventional power supplying components are limited in ubiquitous sensing due to its several challenges such as inflexibility, large volume, and periodic replacement or recharging.¹⁰

To overcome these limitations, academic and industrial researchers have been seeking for the development of wearable devices with highly flexible, multifunctional, sustainable forms and high performances. For wearable and flexible form factors, textile and extremely thin films which are mountable and attachable on human body are used instead of the conventional obtrusive devices.^{3-4, 11-13} For sustainable sensors, the working mechanism is based on energy harvesting system such as triboelectric,¹⁴⁻¹⁷ piezoelectric,¹⁸⁻¹⁹ pyroelectric,²⁰⁻²¹ thermoelectric,²²⁻²³ photovoltaic effects which use green energy sources such as solar, wind, wave, heat, and vibrations.²⁴ In practical applications of wearable sensors, multifunctional sensing performances are required under multiple stimuli such as pressure, temperature, chemical, and light. For high performances of wearable sensors, high sensitivity to target stimulus and high durability in harsh conditions are required (**Figure 1.2**). The main strategy for highly flexible wearable sensors is to fabricate the textile-based and ultra-thin film-based structure using ferroelectric polymer and functional nanoparticles. Moreover, to realize the multifunctional sensing capability under pressure and temperature, working mechanism is based on triboelectric, piezoelectric and pyroelectric effects, which could also realize self-powered sensing system (**Figure 1.3**).

The diagram illustrates the key features of Wearable Tactile Sensors, categorized into two main groups: Fundamental and Sensing Capability.

Wearable Tactile Sensors (Central Core)

Fundamental Features:

- Highly flexible:** Represented by an illustration of a green, stretchable textile-based sensor.
- Skin-attachable:** Represented by an illustration of a hand with a sensor attached to the skin, showing a brain scan.
- Self-powered:** Represented by an illustration of a battery icon with a lightning bolt.
- Eco-friendly:** Represented by an illustration of a green globe.

Sensing Capability Features:

- Multifunctional:** Represented by an illustration of a hand holding a device that measures Pressure, Temperature, and Chemical.
- High Performances:** Represented by an illustration of a hand holding a device that measures Chemical.
- Highly-sensitive:** Represented by an illustration of a hand holding a device that measures Chemical.
- Highly-durable:** Represented by an illustration of a hand holding a device that measures Chemical.

18

Research Strategy for Advanced Wearable sensor

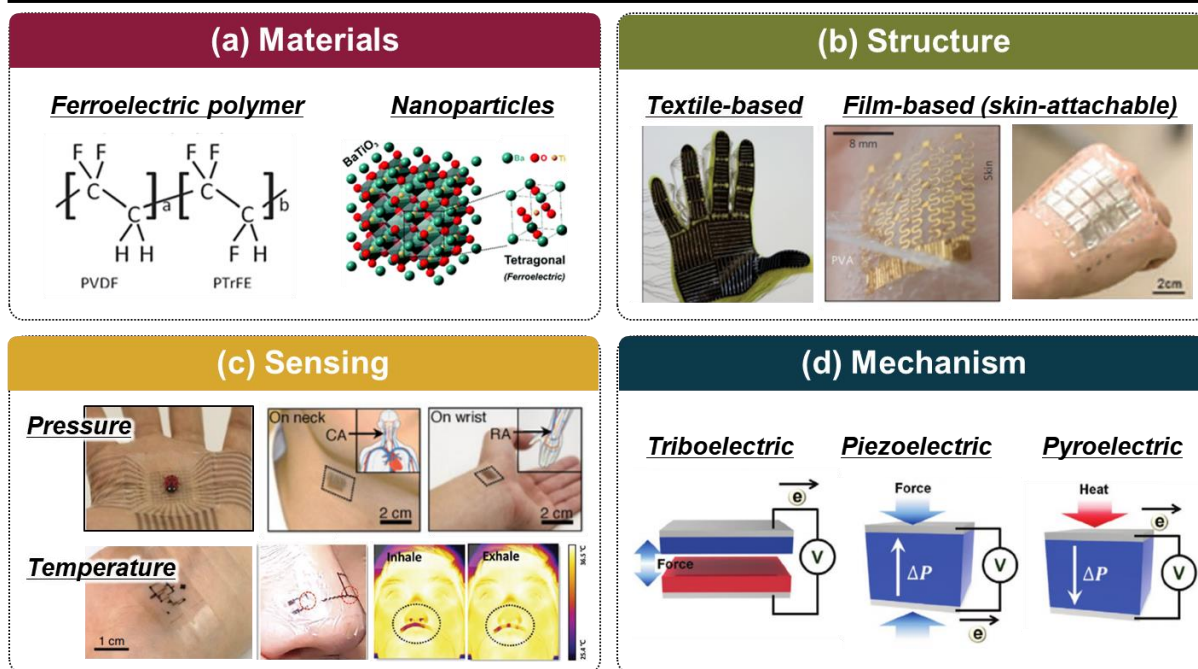


Figure 1.3. Research strategies to achieve the required technologies for advanced wearable sensors in terms of (a) materials (*J. Mater. Chem. A* **2017**, 5, 3091.; *Chem. Soc. Rev.* **2019**, 48, 1194.),³⁶⁻³⁷ (b) structures (*Nature* **2019**, 569, 698.; *Nat. Mater.* **2013**, 12, 938.; *Adv. Mater.* **2018**, 30, 1803388.),³⁸⁻⁴⁰ sensing target stimuli (*Nature* **2018**, 555, 83.; *Nat. Biomed. Eng.* **2018**, 2, 687.; *Nat. Electron.* **2018**, 1, 183.; *Adv. Mater.* **2019**, 1905527.),⁴¹⁻⁴⁴ and working mechanism (*Adv. Mater.* **2019**, 31, 1802898.).²⁴

1.1 Wearable sensors

Wearable electronics are defined as electronic devices which are tightly attached to the human body surface to provide a user-oriented monitoring system without distracting the users.⁹ This superior performance can be attributed to those mechanically soft, flexible, and stretchable forms. Wearable flexible sensors can be categorized according to their forms by fiber/textile-based sensors which are worn onto the human body and thin film-based sensors which are attachable on the skin.

Fiber/textile-based sensors: Textile based wearable sensors can be classified into three types according to the fabrication approaches; (1) integration of sensors in the commercial textiles, (2) weaving and (3) knitting based on one dimensional (1D) fibers contained functionality. The integrated sensors in commercially available fabrics or threads are the most-used approaches for textile-based wearable sensors. By carbonization or simple coating of commercial fabrics or threads with functional materials, active layers can be formed on these commercial substrates.⁴⁵⁻⁴⁷ For examples, these facile methods fabricate the smart textile based on the functional materials such as Ni/carbon nanotube (CNT),⁴⁵ Ag/fluoroelastomer composite,⁴⁶ and Ag/polydimethylsiloxane (PDMS)/CNT,⁴⁷ enabling detection of diverse body motions (Figure 1.4a). Another type is the woven textile-based electronics, which have mechanically stable structure but less-stretchable.⁴⁸⁻⁴⁹ Nonetheless, several researches demonstrated the stretchable sensors by weaving the elastomer-based fibers (Figure 1.4b).⁵⁰⁻⁵¹ Meanwhile, a variety of knitted sensors have been developed for stretchable textile sensors due to their structural characteristics (Figure 1.4 c).⁵²⁻⁵³ Moreover, these fabrications from 1D functional fibers by weaving or knitting have advantages in terms of relatively diverse structures.

Thin film-based skin-attachable sensors: Skin-attachable wearable sensors which can be directly mounted on the skin essentially require flexibility, stretchability, and chemical stability to pick up vital signals without limiting motions such as bending, stretching, and swelling. In this regard, conventional stiff substrate-based electronics have restrictions to be utilized as the wearable sensors.⁵⁴ ‘Epidermal electronic’ which is defined by the flexible stick-on patches with diverse sensing capability have been advanced by a number of researchers.^{6, 55-57} Rogers’s group developed the temporary tattoos-like attachable sensor which is based on the transfer methods using a rubber stamp starting from the conventional silicon-based fabrication (Figure 1.4d).⁶ Contrary to the relatively small sensor developed by Rogers’s group, Someya’s group suggested a much larger electronic device which exhibits ultra-thin (1 micron), light, but also robust enough characteristics. This device can endure stretching and crumpling on human body such as an elbow or knee, which is attributed to the fabrication based on the soft organic materials (Figure 1.4e).⁵⁵ To enhance the sensitivity of attachable sensors, Bao’s group developed the micro-patterned pressure sensors, which can be used to monitor heart motions through real-time sensing of artery pulse pressure (Figure 1.4f).⁵⁶ Furthermore, for

sustainable use of wearable sensors, Wang's group suggested the self-powered systems through electricity transduction from mechanical body movements such as walking, jumping, and running and organ motions such as heartbeat and respiration (Figure 1.4g).⁵⁷ In spite of recent great achievement of wearable sensors, there are still many aspects which should be further developed to meet a great demand for next-generation technology such as the IoT, artificial intelligence (AI), and human-machine interfaces.

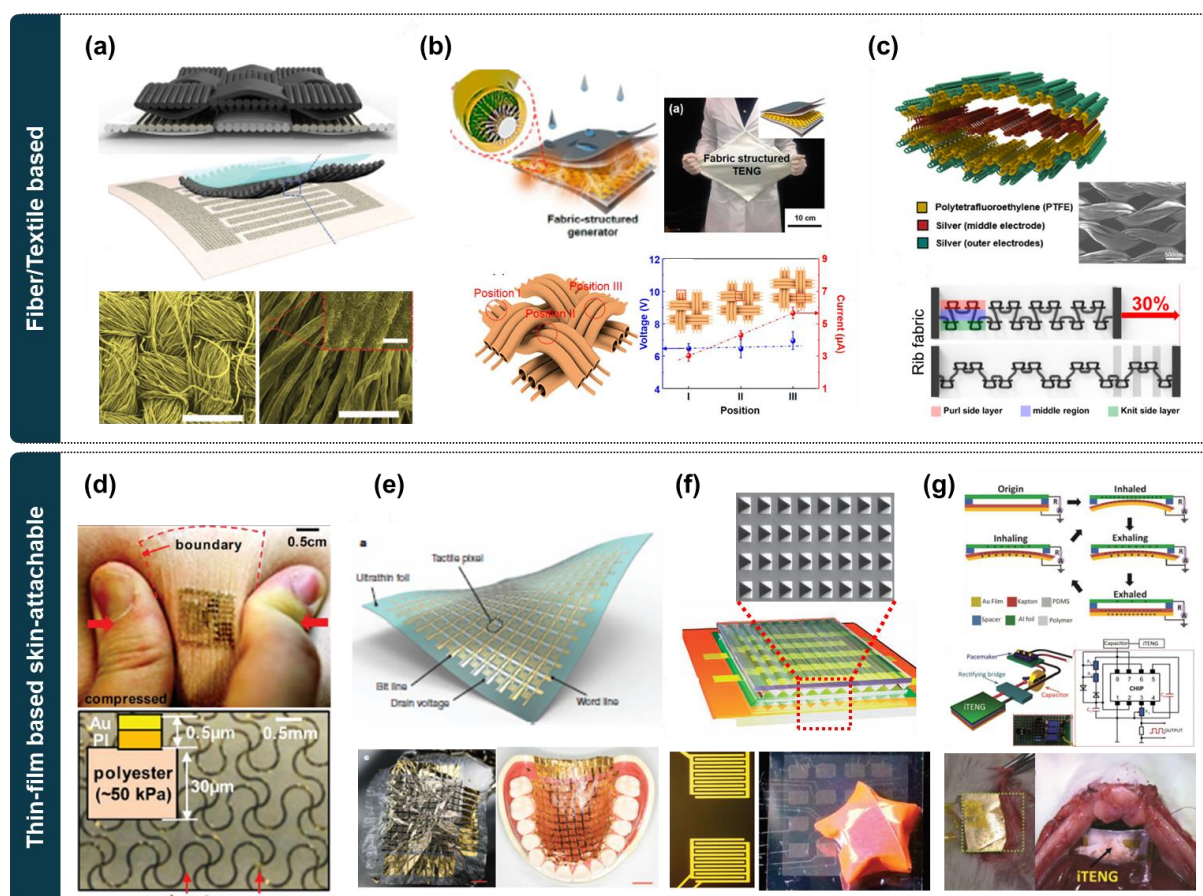


Figure 1.4. Wearable flexible sensors. (a-c) fiber/textile based sensor; (a) integration of sensor in the commercial textiles (*Adv. Mater.* **2017**, 29, 1703700.),⁴⁵ (b) woven sensor based on functional fibers (*ACS Nano* **2015**, 9, 6394.),⁵⁰ (c) knitted sensor based on functional fibers (*ACS Nano* **2017**, 11, 9490.).⁵² (d-g) thin-film based skin-attachable sensors; (d) tattoos-like attachable sensor by transfer method (*Science* **2011**, 333, 838.),⁶ (e) highly stretchable body-attachable sensor based on organic materials (*Nature* **2013**, 499, 458.),⁵⁵ (f) highly sensitive attachable sensors with microstructures (*Nat. Commun.* **2013**, 4, 1.),⁵⁶ (g) sustainable wearable sensor based on triboelectric effect (*Adv. Mater.*, **2014**, 26, 5851.).⁵⁷

1.2. Working mechanism of self-powered wearable sensors

For a sustainable sensing performance, it is crucial to realize the self-powered system which converts ambient environmental stimuli into valuable electric signals without external energy sources.²⁴ These self-powered systems have been receiving considerable attention due to the realization of a wireless system, eco-friendly technology without any pollutant, as well as operation without energy source.^{3, 14} The detailed self-powered sensing systems are categorized by target stimuli such as mechanical stimuli and temperature as described below.

1.2.1. Working principle for mechanical stimuli

Self-powered mechanical sensors monitoring mechanical stimuli such as strain, stress, and vibration can be driven by piezoelectric and/or triboelectric effects which convert mechanical energy into electricity.

Triboelectric effect: Triboelectric effect is caused from friction between two different materials, which are easily experienced in our daily life.⁵⁸ Specifically, triboelectricity is driven by coupling the contact electrification and electrostatic induction during the repeated contact and separation cycles (Figure 1.5a),⁵⁹⁻⁶⁰ and triboelectric device was firstly invented by Wang's group in 2012. The output voltage at open-circuit (OC) condition, V_{OC} is given by

$$V_{OC} = \frac{\sigma x(t)}{\epsilon_0}$$

where σ , $x(t)$, ϵ_0 are surface charge density, gap distance between two triboelectric materials, and vacuum permittivity, respectively.⁶⁰ At short-circuit (SC) condition, the transferred charges, Q_{SC} are given by

$$Q_{SC} = \frac{A\sigma x(t)}{d_0 + x(t)}$$

where A is area and d_0 is effective thickness.⁶⁰ Therefore, for high performance triboelectric devices, surface charge density and contact area have to be improved to achieve the enhanced contact electricity.⁵⁸ Moreover, effective electrostatic induction can be related to the dielectric constant of the materials.⁶¹⁻⁶² Therefore, the selection of triboelectric contact pair materials is crucial to develop the high performance triboelectric devices since surface charge density is relied on the large differences of two materials in charge polarities in triboelectric series. In addition, dielectric constant which is one of the intrinsic material characteristic is determined by the selection of materials. To this end, the

strategy can be classified into two types to improve the triboelectric performances.⁶³ One involves chemical modification to modulate the surface charge by doping,⁶⁴⁻⁶⁵ copolymerization,⁶⁶⁻⁶⁷ and surface functionalization.⁶⁸⁻⁷¹ And the other involves surface patterning to increase in contact area between triboelectric contact pairs by increasing surface roughness, generating a larger amount of charge.⁷²⁻⁷⁶

Piezoelectric effect: Piezoelectric effect converts mechanical energy into electricity, which is driven by the generation of electrical polarization due to deformation of the oriented non-centrosymmetric crystal structures in certain materials under mechanical force (Figure 1.5b).⁷⁷ Wang's group pioneered the self-powered systems based on piezoelectric effect by vertically pressing a ZnO nanowire using an atomic force microscope (AFM) tip.¹⁸ Piezoelectric performance is determined by the piezoelectric polarization charge density (ρ_p) which is expressed as

$$\rho_p = d_p X$$

where d_p is the piezoelectric coefficient, and X is the applied stress.²⁴ Therefore, it is crucial to enhance the piezoelectric coefficient and transfer the applied force more effectively for the high performance piezoelectric devices.

1.2.2. Working principle for temperature

Pyroelectric effect: Pyroelectric effect converts temporal temperature change into electricity, which is driven by the generation of spontaneous polarization in certain materials depending on the applied temperature (Figure 1.5c).⁷⁷⁻⁷⁹ The electric dipoles randomly oscillate within a degree from their aligned axes under ambient temperature due to thermal fluctuations. Nonetheless, no output current is generated since the total average of spontaneous polarization is a constant at a fixed temperature ($\Delta T = 0$). The change of spontaneous polarization causes the pyroelectricity under temporal temperature change ($\Delta T \neq 0$). When pyroelectric devices are in heating state ($\Delta T > 0$), spontaneous polarization can decrease, which is attributed to a larger degree of oscillation of electric dipoles from their aligned axes. Meanwhile, spontaneous polarization can increase under cooling state ($\Delta T < 0$), which is induced by a smaller degree of oscillation of electric dipoles from their aligned axes.^{20, 79} The generated pyroelectric current (i_p) is expressed as

$$i_p = \frac{dQ}{dt} = pA \frac{dT}{dt}$$

where Q , p , A , dT/dt are pyroelectric charge, pyroelectric coefficient, surface area of the material, and the temperature change rate, respectively.⁷⁸ Therefore, it is crucial to enhance the pyroelectric coefficient, surface area, and temperature change rate for the high performances of pyroelectric devices. Pyroelectric devices can be categorized by polymer based and ceramic based materials. Polymer-based pyroelectric devices are more suitable for wearable technology due to flexible, biocompatible, and those easy of processing, but there are limitations with relatively low pyroelectric coefficient. On the other hand, ceramic-based pyroelectric devices have much higher pyroelectric performances due to those higher pyroelectric coefficients, but they are less suitable for wearable devices. To this end, organic/inorganic composite-based devices have been developed to make up for each weakness and amplify the synergy effect.^{20-21, 79}

Thermoelectric effect: Thermoelectric effect also converts thermal energy into electricity, and it is driven by the diffusion of charge carriers due to temperature difference between the two ends of device, which is based on the ‘Seebeck effect’ (Figure 1.5d).⁸⁰ The efficiency of thermoelectric devices relies on the thermoelectric material’s figure of merit (ZT), which is expressed as

$$ZT = \frac{\sigma S^2 T}{\kappa}$$

where σ , S , T , κ are electrical conductivity, Seebeck coefficient, mean operating temperature, and thermal conductivity, respectively. For high performances of thermoelectric devices, it is important to improve the ZT of thermoelectric materials.⁸¹

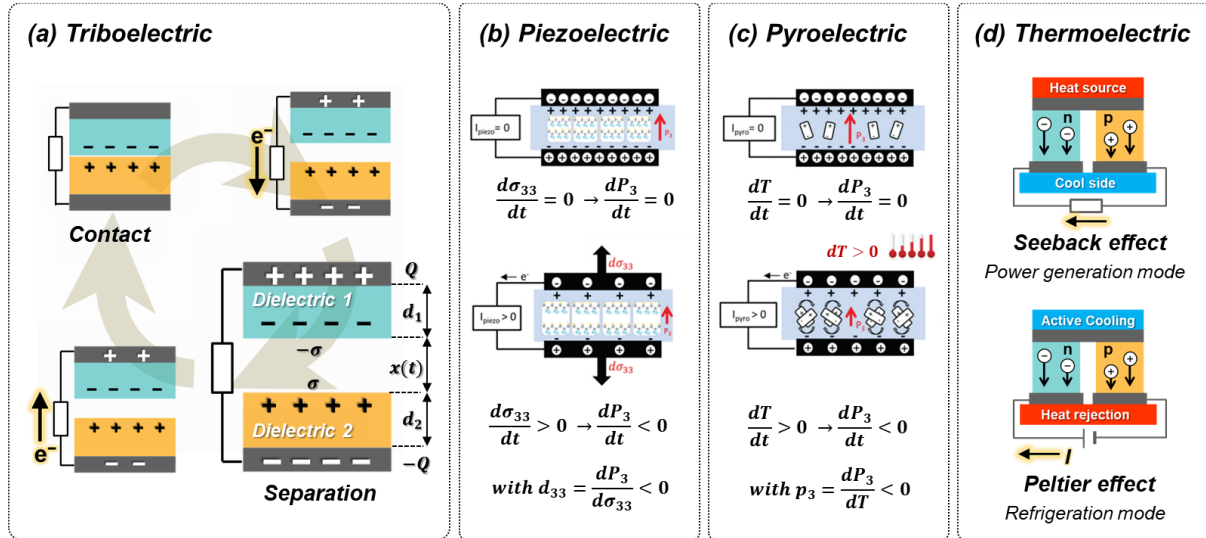


Figure 1.5. Working mechanism of self-powered wearable sensors; (a) Triboelectric, (b) Piezoelectric (*Chem. Soc. Rev.* **2019**, 48, 1787.),⁷⁷ (c) Pyroelectric (*Chem. Soc. Rev.* **2019**, 48, 1787.),⁷⁷ (d) Thermoelectric effect.

1.3. Ferroelectric polymer-based self-powered sensors

Ferroelectric polymers are regarded as an ideal candidate for self-powered wearable sensors, which is attributed to its multimodality based on piezoelectric and pyroelectric transduction, mechanical flexibility, self-powering capability, and those easy of processing.⁷⁷ Ferroelectricity is defined by a spontaneous electric polarization and reversible polarization through the applied electric field, which is manifested in certain materials.⁸² Generally, among 21 non-centrosymmetric crystal classes, 20 classes show piezoelectric effect, within which 10 classes are pyroelectric. Some of the pyroelectric materials exhibit ferroelectrics.⁷⁷ Poly(vinylidene fluoride) (PVDF) are the most representative ferroelectric material, which is composed of vinylidene (VDF) monomer with two fluorine and two hydrogen atoms bonded to its carbon backbone.⁸³ This semi-crystalline polymer shows five distinct crystalline phases, among which β crystalline phase has the highest spontaneous polarization per unit cell and the highest dielectric constant while α crystalline phase which is thermodynamically more stable than β phase, is nonpolar and paraelectric phase (Figures 1.6a, b). This ferroelectric polymer can lose its ferroelectric phase when the material is heated above the Curie temperature (T_c).⁸⁴⁻⁸⁶ When a ferroelectric material is cooled below T_c , domains which have unit cells with equal polarisation directions are randomly distributed, which results in no net polarization even with β crystalline phase. In this regard, the randomly orientated electrical dipoles should be aligned in a common direction by electric field to achieve a net polarization, which is called ‘electric poling’ process. The electrical dipole alignment by poling process is crucial to convert an inactive ferroelectric material to electromechanically active material (Figure 1.6c).³⁶ For high performance of ferroelectric polymer-based devices, it is important to enhance the β crystalline phase and induce the electromechanically active state. To this end, to improve the PVDF characteristic, PVDF based copolymer has been developed. Poly(vinylidene fluoride-co-trifluoroethylene) (PVDF-TrFE) is the most studied copolymer, which presents ferroelectric β crystalline phase owing to the third fluoride in the TrFE monomer unit with a large steric hindrance.⁸⁷⁻⁸⁸ Due to its promising characteristics, ferroelectric polymers, especially PVDF and its copolymers, have been exploited extensively for piezoelectric, pyroelectric, even triboelectric sensors.^{36, 87}

1.3.1. Piezoelectric devices based on ferroelectric polymer

Piezoelectric effect based on PVDF and its copolymer has been studied for the detection of mechanical stimuli such as compressive and tensile strain, tactile sensation, acoustic waves and vibration.⁷⁷ Contrary to piezoresistive and capacitive effect, piezoelectric effect is suitable for self-powered devices due to energy transduction properties without any external power source.

A variety of approaches have been suggested to achieve the high performances of piezoelectric sensors through the composite with fillers,⁸⁹⁻⁹² the micro/nano structured films,⁹²⁻⁹³ and the form of fibers⁹⁴⁻⁹⁵ or fabrics.⁹⁶⁻⁹⁷ For enhanced piezoelectric properties, ceramic materials such as barium titanate (BaTiO_3),⁸⁹ titanium dioxide (TiO_2)⁹¹ and carbon-based materials such as rGO,⁹² CNT⁹⁸⁻⁹⁹ have been used for filler materials in PVDF-based ferroelectric polymer matrix (Figure 1.7a). Micro/nano patterned structures have been proposed for high sensitivity due to effectively transferred force and localized strain (Figure 1.7b).⁹²⁻⁹³ Moreover, Fibrous sensor and textile sensor based on as-spun fiber have shown high performance piezoelectric performances, which is attributed to *in situ* alignment by the applied strain or electric-field during fabrication process such as wet-spinning, melt-spinning,^{95, 97} and electrospinning (Figure 1.7c).^{94, 96, 100}

1.3.2. Pyroelectric devices based on ferroelectric polymer

To date, pyroelectric effect from PVDF-based polymer was utilized for diverse sensors such as IR-sensor arrays for human proximity detection, heat-sensing, fire alarms, and pollution monitoring.^{78-79, 101-103} For the high performance of pyroelectric sensors, a number of approaches have been proposed, which is categorized by structure modification for effective thermal energy absorption¹⁰⁴⁻¹⁰⁸ and material modification for enhanced pyroelectric coefficient.¹⁰⁹⁻¹¹¹ Zabek et al. introduced a partially covered micropatterned top electrode for effective heat transfer and larger temperature fluctuation. The pyroelectric performances depended on the electrode coverage rate due to different temperature change rate (Figure 1.7d).¹⁰⁴ Moreover, Zabek et al. demonstrated asymmetric electrodes in the pyroelectric devices for effective radiation absorption. Graphene ink was used for asymmetric top electrodes for the improved pyroelectric performance which is induced by faster and larger temperature changes.¹⁰⁵ Zhao et al. reported noncontact nIR-driven pyroelectric devices depending on the electrodes such as Al, ITO, graphene, and CNT. Due to the high infrared absorption, CNT electrode on both sides of PVDF film showed the highest pyroelectric performances.¹⁰⁶ Lee et al. utilized graphene electrode with high thermal conductivity for fast thermal gradient which results in high performance pyroelectric devices (Figure 1.7e).¹⁰⁸ In order to enhance the pyroelectric coefficient, several approaches have been introduced such as material modification and crystallinity modulation. Gan et al. reported approach to enhance the pyroelectric property based on PVDF and TiO_2 composite materials through an interfacial relaxation phenomenon (Maxwell-Wagner effect). The heterogenetic structure of composite material induced an efficient poling process by this phenomenon, which results in the enhancement of pyroelectric coefficient at a much lower poling electric field.¹⁰⁹ Mokhtari et al. reported the electrospun PVDF fiber-based pyroelectric devices which showed high β crystalline phase without additional poling process due to *in situ* alignment during

electrospinning procedure.¹¹⁰ Kim et al. induced the high crystallinity and dipole alignment of P(VDF-TrFE) by using high dipole moment solvent, which results in highly enhanced pyroelectric performances (Figure 1.7f).¹¹¹

1.3.3. Triboelectric devices based on ferroelectric polymer

PVDF-based ferroelectric polymers have been used for triboelectric devices due to its strong electro-negativity in the triboelectric series and its ease of processing as well as flexibility. Moreover, the applied external electric field decides the polarization states that rely on aligned dipoles in ferroelectric polymers.^{36, 87} For the high performance of triboelectric sensors based on PVDF-based polymer, a variety of reports have been introduced, which is categorized by structure modification for the improved surface contact area, the internal polarization modulation based on ferroelectric characteristics, and material modification for higher surface charge density.

One of the strategies for the enhanced triboelectric performance is to increase the surface contact area which is directly proportional to triboelectric output. To this end, a number of researchers have made a lot of effort to increase the surface area using micro/nano patterned structures. Ha et al. demonstrated highly sensitive triboelectric sensors based on the hierarchical nanoporous and interlocked microstructures by mimicking the gradient stiffness of human skin. This innovative structure induces efficient stress concentration and transfer, and the effective contact-separation between opposing surfaces without additional bulky spacers, leading to highly sensitive triboelectric performances (Figure 1.7g).⁷⁵ Qin et al. fabricated PVDF-HFP nanofibers-based wearable sensors by electrospinning. Due to the ultrahigh specific surface area from electrospun nanofiber, the triboelectric device possesses noticeable triboelectric output performances. Moreover, this structural innovation provides the solution to overcome the delamination problem with electrode layer during long-term uses.¹¹²

Several researchers have suggested approach to boost output power using PVDF-based composites with inorganic nanoparticles and electrical poling process that enhance triboelectric charge density.^{62,} ¹¹³ Seung et al. reported high triboelectric output performances from P(VDF-TrFE)/BTO nanoparticles, which is attributed to the increased capacitance due to a large charge-trapping capability by high dielectric ceramic nanoparticles. They optimized fraction of nanoparticles into polymer matrix through contact potential difference (CPD) measurements (Figure 1.7h).⁶² Kim et al. presented a method for the maximized frictional surface charge density by doping of P(VDF-TrFE) and Nylon-11 with MoS₂ flakes. Both ferroelectric composite materials can be negative and positive triboelectric contact pairs, which results in high triboelectric output performances.¹¹³

Many research groups have demonstrated triboelectric phenomena based on polarization states-tuned ferroelectric polymers.^{111, 114-117} Kim et al. demonstrated that the higher dipole moment solvent considerably enhances the triboelectric output power since higher crystallinity and better dipole alignment of the polymer can be induced.¹¹¹ Bai et al. effectively modulated the triboelectric properties of PVDF by using the dipole moment in polarized ferroelectric polymer, which results in considerably enhanced triboelectric outputs.¹¹⁴ Lee et al. reported the higher positive triboelectric properties compared to skin which is regarded as the highest position in the triboelectric series. This research demonstrated the controllable triboelectric properties of ferroelectric materials depending on their polarization direction and intensity, which was explored by triboelectric output measurement as well as Kelvin probe force microscope (KPFM).¹¹⁵ Moreover, same group also monitored both the amount and direction of charge transfer in P(VDF-TrFE), which was investigated using atomic force microscopy (AFM). According to this research, ferroelectric polarization state can modulate the amount and direction of the charge transfer in triboelectricity (Figure 1.7i).¹¹⁶

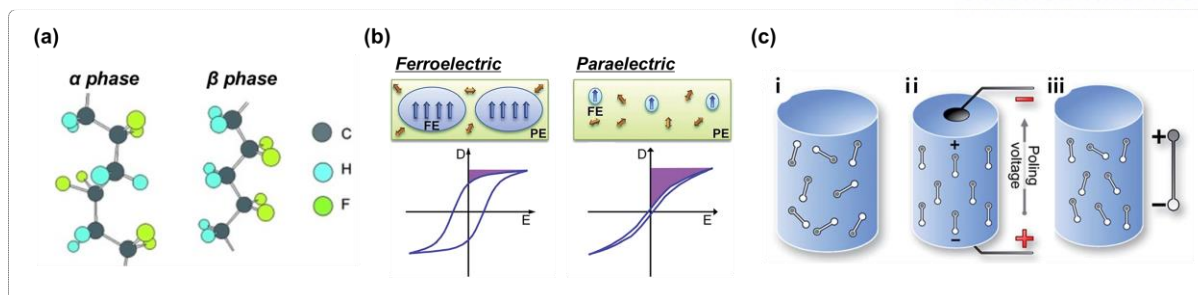


Figure 1.6. Schematics of representative ferroelectric polymer, PVDF. (a) Chin conformation for the α and β phases of PVDF (OMNEXUS home page, <https://omnexus.specialchem.com/selection-guide/polyvinylidene-fluoride-pvdf-plastic>, accessed: May 2020.).¹¹⁸ (b) D-E loops and domain structures of ferroelectric and paraelectric states (*Polymer* **2012**, 53, 728).⁸⁶ (c) Electrical poling procedure of ferroelectrics; i. Initially random arrangement of domains, ii. Aligned domains under the applied electric field, iii. A remnant polarisation under removing the electric field (*J. Mater. Chem. A* **2017**, 5, 3091.).³⁶

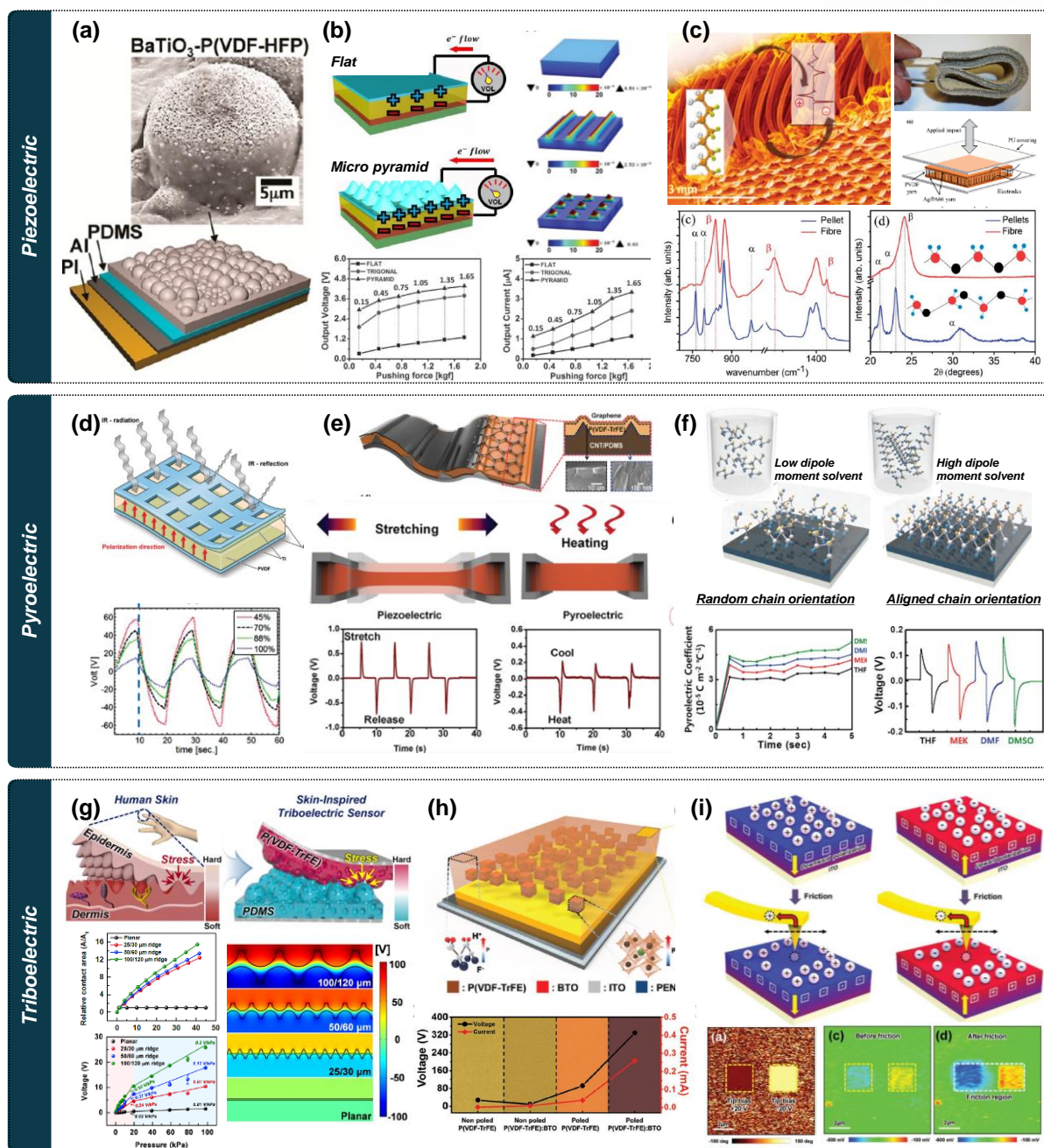


Figure 1.7. PVDF and its copolymer-based self-powered sensors. (a-c) High performance of piezoelectric sensors with (a) composite materials (*ACS Nano* **2014**, 8, 2766.),⁸⁹ (b) micropatterned structure (*Adv. Funct. Mater.* **2015**, 25, 3203.),⁹³ and (c) textile form (*Energy Environ. Sci.* **2014**, 7, 1670.).⁹⁷ (d-f) Enhanced pyroelectric sensing performances with (d, e) effective thermal energy absorption (*Adv. Energy Mater.* **2015**, 5, 1401891.; *Adv. Mater.* **2014**, 26, 765.),^{104, 108} and (f) material modification (*Adv. Funct. Mater.* **2017**, 27, 1700702.).¹¹¹ (g-i) Performance-modulated triboelectric sensors with (g) microstructures (*ACS Nano* **2018**, 12, 3964),⁷⁵ (h) composite materials (*Adv. Energy Mater.* **2017**, 7, 1600988.),⁶² and (i) ferroelectric polarisation (*Adv. Funct. Mater.* **2016**, 26, 3067.).¹¹⁶

1.4 Applications of self-powered wearable sensors

Self-powered wearable sensors have been intensively researched and achieved rapid advancement to keep up with the recent surge in demand. Benefiting from their superior performances, these self-powered wearable sensors are regarded as promising candidates for the future applications such as daily healthcare,¹¹⁹⁻¹²⁰ biometric security systems,¹²¹⁻¹²² soft robotics,¹²³ and smart tactile sensors.¹²⁴⁻¹²⁵

Healthcare: High sensitivity of wearable sensors has an advantage in monitoring the biomechanical signals of the human body, enabling diagnosis and prevention of several diseases in advance.⁸ To realize the ubiquitous health care, wireless system is essentially required, which could be possible by the self-powered sensors.⁹ The real-time monitoring of arterial pulse pressure can diagnose early cardiovascular diseases like arteriosclerosis, diabetes, and hypertension using information such as blood pressure as well as heart rate (Figure 1.8a).^{42, 126} Moreover, the real-time monitoring of gait patterns can be used for early diagnosis and prevention of several diseases, for examples, abnormal gait pattern is one of the symptom of Parkinson's disease, and diabetic foot ulcers can be caused by abnormal plantar pressure distribution (Figure 1.8b).^{125, 127} Furthermore, the monitoring of body motion can be used for long term rehabilitation after stroke, which is an important factor to ensure motor function recovery. The real-time monitoring of upper and lower extremities such as wrist, arm, and leg provides clinically relevant information which can be used for home-based rehabilitation technology.¹²⁸⁻¹²⁹

Biometric security systems: Due to the low risk of loss, copying, and sharing, biometric systems have been regarded as one of the ideal security system. Everyone has unique fingerprint as well as voice pattern, which can be utilized for personal passwords.^{121, 130} High performance acoustic sensor can be used for this voice-based security system, and several researches suggested eardrum-inspired acoustic sensors which show high sensitivity, fast response, and detection capability in wide range of frequency (Figure 1.8c).^{122, 131-132} In addition, wearable tactile sensors have been intensively studied, which suggests biometric security systems based on fingerprint recognition. The fingerprint sensors within a display require the advanced properties such as high resolution, transparency, as well as flexibility. Recently, higher performance sensor enabling multifunctional detection of finger pressure and skin temperature is developed based on transparent electrodes. Their resolution of sensor array sufficiently meets the criteria set by the Federal Bureau of Investigation (FBI) for extracting fingerprint patterns (Figure 1.8d).¹³³⁻¹³⁵

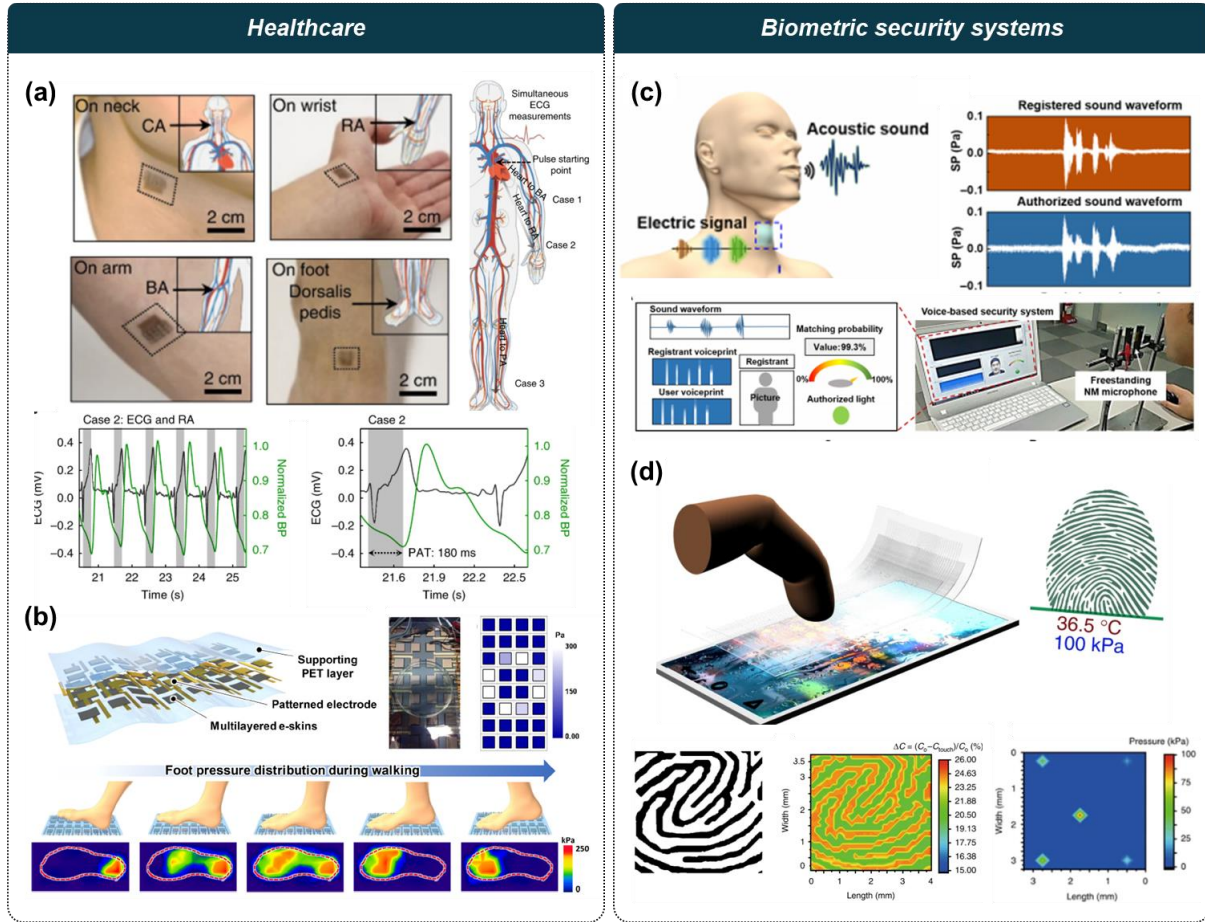


Figure 1.8. Applications based on self-powered wearable sensors; daily healthcare for (a) pulse pressure detection (*Nat. Biomed. Eng.* **2018**, 2, 687.)⁴² and (b) real-time gait patterns monitoring (*ACS Nano* **2018**, 12, 4045.)¹²⁵ biometric security systems with (c) voice patterns (*Sci. Adv.* **2018**, 4, eaas8772.)¹²² and (d) fingerprint (*Nat. Commun.* **2018**, 9, 1.)¹³³

1.5 Challenges of current self-powered wearable sensors

In the introduction, we summarized recent progress in wearable sensors, including fundamental working principles, advanced research strategies, and potential applications. In spite of recent great achievement of wearable sensors, there are still challenges to meet a great demand for practical applications. Wearable sensors should be further advanced by miniaturization, simplification, as well as self-powered operation, which will realize the ideal wearable sensors enabling unobtrusive, personalized, pre-diagnosable, and sustainable.

First, a wearable sensation is one of the crucial factors for the ultimate goal of future electronics, which could be achieved by highly flexible and high performance sensor design.^{9, 124} Textiles have been considered for promising platform due to its ubiquitous nature in our daily life. Although textile-based sensors have been developed through various traditional textile fabrication techniques, most approaches have insufficient mechanical properties, which restrict their practical uses.^{48-53, 136-139}

Second, multimodality in sensing multiple stimuli can accelerate to downsize and simplify wearable sensing devices. Multimodal sensing capability from most conventional self-powered sensors has been demonstrated by integrating the single elements for each stimulus,^{111, 140-143} which can restrict practical uses. Although there have been efforts to develop the simultaneous multimodal sensors, most sensors have problems with external power sources^{11, 92, 141, 143-144} and signal interference between multiple stimuli.^{140, 142, 144-145}

Third, the self-powered wearable sensors have been enhanced considerably in recent years through various approaches using diverse materials and structures, among which dissimilar hybrid materials have been widely used to boost triboelectric output performances. Especially, soft/hard hybrid materials have been utilized to make up for each weakness and amplify the synergy effect.^{62, 146-147} Nonetheless, there are still challenges in precise control of dissimilar material distribution¹⁴⁸⁻¹⁵⁰ to maximize the synergy effect, leading to high performance of triboelectric wearable sensors.

To address these issues, the ultimate goal of this work is to develop advanced sustainable wearable sensors with multimodality and high performances *via* structure design and modification of the material characteristics (**Figure 1.9**). In Chapter 2, we demonstrate the textile-based self-powered wearable sensors with high sensitivity, mechanical stability, and washing durability, enabling the practical uses. Chapter 3 describes triboelectric/pyroelectric effect-based multimodal sensors without signal interference, which is attributed to switchable triboelectric polarity *via* ferroelectric polarization. In Chapter 4, a novel approach is suggested for high performance of triboelectric sensors using layer-by-layer structure with soft/hard ferroelectric materials. Lastly, we summarize this thesis with future prospects and challenges of this research field in Chapter 5.

Chapter 2. Self-powered textile sensors with programmable stitch patterns based on PVDF fibers for realization of practical uses

2.1 Introduction

Smart textiles have great potential as next-generation wearable electronics in diverse fields such as those related to sensors,^{45, 153-154} energy generators,^{50, 53} transistors,¹⁵⁵⁻¹⁵⁶ and capacitors¹⁵⁷⁻¹⁵⁸ owing to their inherent characteristics of flexibility, deformability, comfort, breathability, and washability.^{136, 159-161} Moreover, textiles are essential in our daily life, and this ubiquitous nature makes them a promising platform for sensors that can be in direct contact with human beings. In particular, textile-based sensors have been widely explored for intelligent control, daily activity monitoring and medical diagnostics with diverse operation types such as capacitive,¹⁵⁴ piezoelectric,¹⁶² piezo resistive,^{45-46, 153, 163} and triboelectric.^{47-53, 137-139, 164-167} In particular, self-powered triboelectric sensors that do not rely on an external power source have been considered for electronic textile (e-textile) sensors because these systems have advantages of high efficiency, low cost, versatility in material choices and stability without the problems related to safety and weight of batteries.¹⁶⁸⁻¹⁷²

Various approaches have been suggested for textile-based sensors, which can be classified into three types; (1) integration of sensors with the existing two dimensional (2D) fabrics or threads, (2) woven textile sensors based on one dimensional (1D) electronic fibers, and (3) knitted sensors based on 1D functional fibers. The most-used approach is to functionalize the existing 2D fabrics or 1D threads by carbonization¹ and simple coating such as Ni/carbon nanotube (CNT) coating,⁴⁵ Ag-fluoroelastomer composite coating,⁴⁶ polydimethylsiloxane (PDMS)-Ag nanowire composites/polytetrafluoroethylene (PTFE)/polyurethane (PU)-Ag nanowire layered coating,¹⁶⁶ and PDMS/CNT/Ag layered coating.⁴⁷ However, these approaches have a limitation in fabricating more delicate structures on a large scale because of the mechanically weak conductor and polymer coatings on existing fabrics and threads. In addition, such fabrics are less suitable for daily life situations because the coated materials can detach from fabrics or threads during washing and repeated usage. Weaving and knitting are commonly used techniques in the textile industry. Woven textiles are typically produced by the interlacing of wefts (transverse threads) and warps (longitudinal threads) threads. Meanwhile, knitted textiles are typically composed of looped interconnections of courses (horizontal rows) and wales (vertical rows) with a series of yarns. Hence, woven textiles usually maintain stable structures but are not suitable for stretchable e-textile, while knitted textiles have better stretchability but are less stable.¹³⁶ In comparison with the approach of sensor embedment in commercial textiles, weaving and knitting by 1D functional fiber have the advantage of fabrication of relatively diverse structures. There have been many studies on the fabrication of woven 2D textile based on 1D electronic fiber.^{48-51, 137-138} Diverse

knitted fabrics based on 1D functional fiber have been developed for stretchable textile sensors, considering their structural characteristics.^{52-53, 139} However, owing to the weak mechanical properties of fibers, most of the approaches are incompatible with the machine processes used in the traditional textile industry, preventing the widespread application of e-textiles. Particularly, the traditional weaving and knitting techniques have the limitation that the sophisticated textile structures cannot be fabricated for e-textiles. On the other hand, sewing machine stitching or embroidery techniques can be used to fabricate sophisticated textile structures because these approaches enable realizing computerized 1D or 2D structures on 2D substrates. The stitching technique has been used for realizing conductive stitches for chemical sensors,¹⁷³ circuits,¹⁷⁴ and antennas¹⁷⁵ and for insulating stitches for photonic sensors¹⁷⁶ and printed circuit boards (PCBs).¹⁷⁷ However, most of the stitched devices are not washable and need external light or electrical power sources for operation.¹⁷³⁻¹⁷⁷

Herein, for the first time, we report the sewing machine stitching of polyvinylidene fluoride (PVDF) fibers into programmable textile patterns for wearable self-powered triboelectric sensors. Mechanically strong fibers are necessary for sewing machine stitching, as the fibers have to withstand the mechanical stress and breakage during the stitching process. Although diverse polymers such as PTFE,¹⁷⁸ PDMS,¹⁷⁹ and parylene¹⁶⁵ have been used for developing triboelectric devices, only a few choice of polymers, including nylon,¹⁸⁰ polyethylene terephthalate (PET),¹⁸¹ and silk¹⁸² can be used in the fiber-spinning process and applications in textile-based triboelectric devices. The PVDF fiber has been widely used in triboelectric devices because of its strong electro-negativity in the triboelectric series and its ease of processing.¹⁸³⁻¹⁸⁵ However, conventional as-spun PVDF fibers that have been fabricated by melt-spinning^{97, 186} or electro-spinning^{183, 187} processes are not suitable for stitching by a sewing machine. The melt-spinning process cannot provide high-strength fibers owing to inadequate structural development.^{186, 188} In the electro-spinning process, electro-spun PVDF fibers are commonly in a 2D-web state that is not suitable for sewing machine stitching, which requires continuous 1D fibers.¹⁸⁹⁻¹⁹⁰ In this work, for the sewing machine stitching of e-textiles, we obtained mechanically strong PVDF fibers by a dry-jet wet spinning process. “Dry-jet wet spinning” is similar to “wet-spinning”, and there is a small difference in the position of spinneret; spinneret of dry-jet wet spinning is outside the coagulation bath while spinneret of wet-spinning is inside the coagulation bath. Therefore, the extruded dope passes through an air gap before entering a coagulation bath.¹⁹¹⁻¹⁹² This air gap could induce the drawing of the jet that is the stable stream of dope in air, which results in the strong PVDF fibers. To the best of our knowledge, while there are several literatures about wet-spun PVDF fibers,¹⁹³⁻¹⁹⁴ the dry-jet wet spun PVDF fiber has not been reported. Owing to the facile sewing machine process of various stitch patterns, the proposed stitching of PVDF fiber threads enables realizing triboelectric wearable devices with diverse patterns and form factors for human motion sensing and bio-signal detection when stitched on the desired apparel. Our e-textile sensors provide a

broad range (326 Pa–326 kPa) of pressure detection capability, while previous textile sensors have a narrow detectable pressure range of tens of kilopascal to hundreds of kilopascal,⁴⁷ or can detect only high pressure in the kilopascal range¹⁶² and several megapascals.¹⁵⁴ Owing to this broad pressure detection range, our e-textile sensors enable diverse applications from biomechanical applications to health monitoring pressure detection. We demonstrated PVDF stitch-based triboelectric sensors for detecting various hand gestures and for real-time pulse monitoring. In particular, the sensing performance can be maintained even after dozens of washings. The washability of textile-based devices is one of the crucial factors for the practical applications of e-textiles.

2.2 Experimental details

Preparation of dry-jet wet spun PVDF fiber

PVDF with an average molecular weight of 534,000 g/mol and 99.5% N,N-dimethylformamide (DMF) were purchased from Sigma Aldrich, Co. and Samchun, Co., respectively. The PVDF polymer solution was prepared by dissolving PVDF in DMF at a concentration of 31 wt%. Dry-jet wet spinning was conducted using a custom-designed fiber spinning unit manufactured by Dissol, Co. (Republic of Korea) with an air-gap of 1 cm. The coagulation medium was deionized water maintained at 10 °C and the fiber was taken up at 10 m/min (spin-draw ratio: 2). The collected fibers were immersed in deionized water at room temperature for a day to remove the residual DMF in the fiber. Then, the fibers were further drawn in few steps using a heated godet roller at 50 and 90 °C. The maximum achievable draw ratio in the post-spin drawing process was 3.05, leading to a total draw ratio of 6.1 (including spin-draw ratio).

Fabrication of sewing machine stitching of the PVDF fiber

Multi-ply threads were prepared from the mono-ply as-spun PVDF fiber to use for sewing-machine operation and its diameter was similar to that of the commercial sewing thread. Various stitches were sewn on the conductive fabric (silver), which was sandwiched between supportive insulating fabrics by a commercial sewing machine (INNOVIS-950, Zhuhai Brother Industries Co. Ltd., China). For the textile sensor with two electrodes, we used nylon fabric with Al electrode as an opposite triboelectric part. And, for the textile sensor with single electrode, we used nylon fabric or skin without electrode as an opposite triboelectric part.

Characterization

The mechanical properties of the fibers were measured using a single filament tensile tester (FAVIMAT+, Texttechno, GmbH, Germany) at a gauge length of 25 mm and a strain rate of 1 %/s with a pre-tension of 0.5 cN. The SEM images of the stitches and coaxial thread were characterized by using a field emission scanning electron microscope (FE-SEM, S-4800, Hitachi, Japan). The open-circuit voltage and short-circuit current were measured by using an oscilloscope (DPO 2022B, Tektronix, US) and a source meter (2450-SCPI, Keithley, US), respectively. The output characteristics of the sensor were measured by applying a periodic force using a pushing tester (JIPT-100, JUNIL TECH, Korea).

2.3 Results and discussion

Structure of the sewing machine stitching sensor based on the PVDF fiber

Figure 2.1a shows schematic and photographic images of the sewing machine stitching of PVDF fibers. For the PVDF stitching process, multi-ply PVDF threads were fabricated from mono-ply PVDF fibers (8 filaments) that were spun by a dry-jet wet spinning process (Figure 2.2). PVDF was chosen as the main triboelectric material for fabricating triboelectric sensors because of its good biocompatibility, spinnability, and strong tendency to gain electrons.¹¹⁴ The mechanical properties of the PVDF fibers are shown in Figure 2.3a. The tensile strength and tensile modulus of the PVDF fibers are 0.24 ± 0.02 Gpa and 4.08 ± 0.29 Gpa, respectively, which are remarkably higher than those of the conventional PVDF fibers (Figure 2.3b, Table 2.1). Owing to the high mechanical strength of the prepared PVDF thread, it could be sewed by hand and even by a sewing machine. To the best of our knowledge, there is no existing report on fabricating a textile device with PVDF-based stitches by a sewing machine owing to the weak mechanical property of PVDF fibers. For sewing machine stitching, it is necessary to prepare two threads that compose the upper and lower stitches on both sides of the fabric. In our work, PVDF thread was used as the lower thread for stable sewing since the lower one is under relatively less tension than the upper one. A commercial PET thread was used as the upper thread to support PVDF stitching on the electrode fabrics. For the electrodes, knitted conductive fabrics composed of silver were utilized due to their softness, tactile comfort, and high conductivity. The conductive fabric was sandwiched between supportive cotton fabrics which were used as insulating layers for stable sensing. Then, the conductive fabric was connected with stainless steel conductive threads by knots, which play the role of wire electrodes similar to the conventional Cu wire electrodes.

Consequently, various PVDF stitch patterns could be easily fabricated by facile sewing machine stitching, resulting in e-textiles with all-stitched structures. Figures 2.1b-i show photographic and scanning electron microscopy (SEM) images of diverse stitch patterns such as the simple stripe (Figures 2.1b, c), embroidered pattern (Figures 2.1e, f), embroidered lines (Figure 2.1h), and even letters (Figure 2.1i), indicating that PVDF threads are mechanically strong enough to be sewed into arbitrary patterns. The stitch pattern is composed of twisted 5-ply PVDF threads (40 filaments), which comprise mono fibers of diameter ~ 50 μm (Figures 2.1d, g). When stitched on stretchable fabric, PVDF stitch patterns show a good mechanical stability for the folding, stretching, twisting and crumpling deformations (Figures 2.1j-m). This capability of sewing machine stitching of various patterns facilitates the fabrication of sophisticated textile structures for e-textile applications.

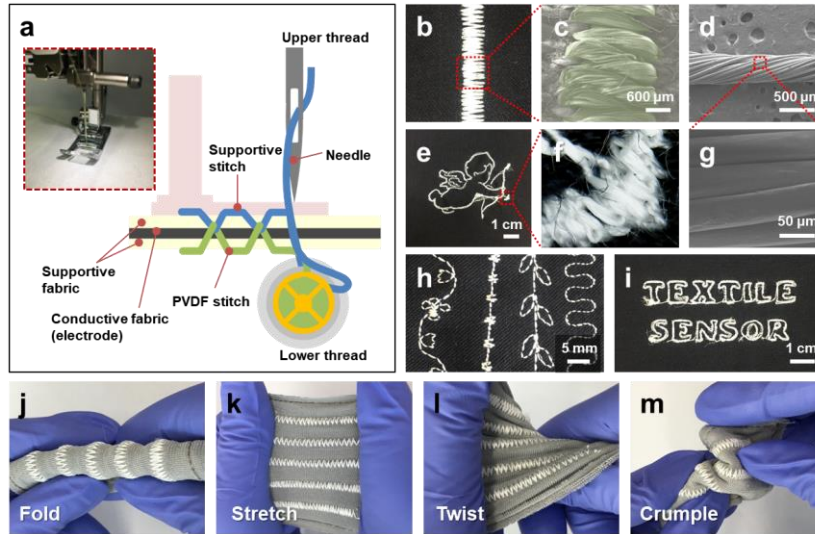


Figure 2.1. PVDF stitch-based triboelectric textile sensors. (a) Schematic illustration of the fabrication procedure of textile sensors by a sewing machine. (b–c) Photographic and SEM images of PVDF-based stripe stitch; (d, g) SEM images of the twisted 5-ply PVDF threads composed of mono fibers of diameter $\sim 50 \mu\text{m}$. Photographic images of (e–f) PVDF-based embroidery, (h) PVDF-based embroidered line stitches, and (i) PVDF-based letter stitches. (j–m) Photographic images of textile sensor demonstrating effects of different mechanical forces, including folding, stretching, twisting, and crumpling.

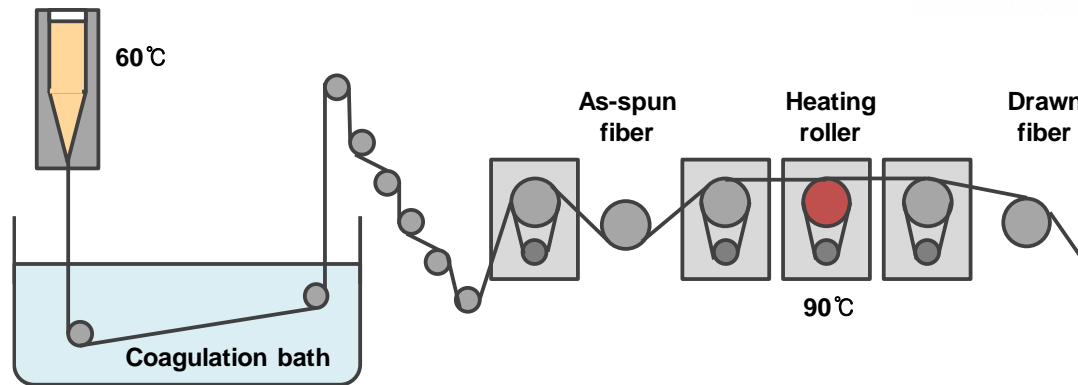


Figure 2.2. A schematic illustration of the lab scale dry-jet wet spinning procedure.

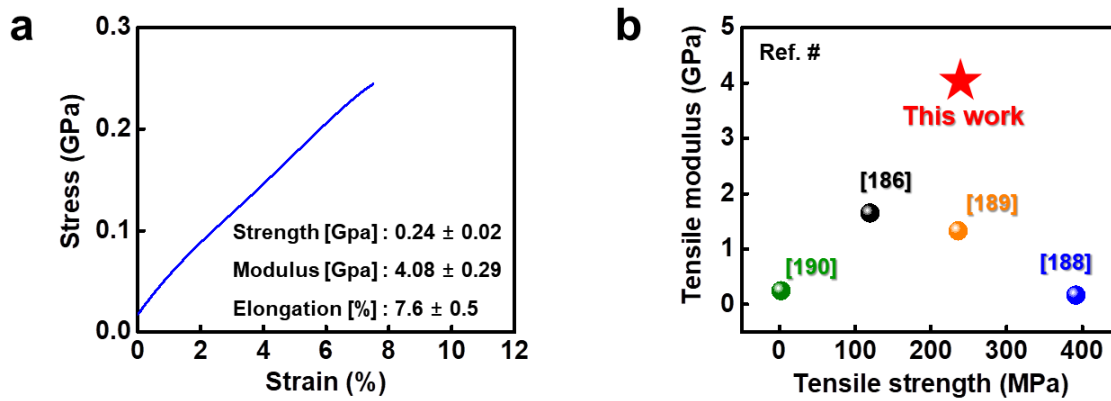


Figure 2.3. Mechanical characteristics of dry-jet wet-spun PVDF in this work; (a) Strain-stress curves, and (b) comparison of tensile modulus and strength based on this work and previous reports.^{186, 188-190}

Table 2.1. Comparison of mechanical characteristics of the results achieved in this work with previously reported as-spun PVDF fibers.

Fiber	Strength (GPa)	Young's modulus (GPa)
Melt-spun PVDF ¹⁸⁶	0.12	1.65
Melt-spun PVDF ¹⁸⁹	0.24	1.33
Electro-spun PVDF ¹⁸⁸	0.39	1.69
Electro-spun PVDF ¹⁹⁰	0.002	0.25
Dry-jet wet-spun PVDF (this work)	0.24	4

Working mechanism and device performance

Figures 2.4a and b show the photographic images of PVDF stitch sensors on layered fabrics, which are in contact with the nylon fabric on the Al electrode. Figures 2.4c and d show the SEM images of each surface of the nylon fabric and PVDF stitch. In our sensor structure, the effective contact area of PVDF stitches with opposite surfaces depends on the applied force since the stitch patterns can play the role of a spacer due to their own sub-millimeter height (Figure 2.4d). In addition, as an opposite triboelectric material, the knitted nylon fabric with entangled nylon microfiber structures can provide high surface area and large compressibility (Figure 2.4c). This unique combination of structures can increase the pressure sensitivity of triboelectric sensors. The working mechanism of PVDF-stitch-based triboelectric sensors is illustrated in Figure 2.4e, and it is based on the conjunction of contact electrification and electrostatic induction during the contact and separation with nylon. According to the triboelectric series, PVDF has a higher electron affinity than nylon.¹⁹⁵ Therefore, when the two materials make contact with each other under compressive force, the PVDF stitch is negatively charged by obtaining electrons while the nylon fabric is positively charged by losing electrons. Once the two materials are separated by releasing the pressure, an electric potential difference is created between the two electrodes. Therefore, electrons flow from the electrode of the PVDF stitch to the electrode of the nylon fabric until the equilibrium state is reached by the accumulated charges. When the two materials approach each other again, electrons flow inversely to realize charge balance. Then, charge neutralization occurs again when the PVDF stitch is fully in contact with the nylon fabric. Repeated contact–separation movements between two objects ($10 \times 10 \text{ mm}^2$) induce continuous alternating current and voltage outputs (Figures 2.4f and, g). Figure 2.5 shows triboelectric signals of PVDF-stitch-based triboelectric sensors induced by using various opposite materials with lower (silk, Al, cotton, and PI) or higher (PDMS and PTFE) electron affinity in the triboelectric series. Nylon has the highest triboelectric signal owing to the largest difference in electron affinity between nylon and PVDF. Compared to the signals induced by materials with lower electron affinity, the opposite shapes of signals can be observed for PDMS and PTFE materials owing to their higher electron affinity as compared to PVDF. Figure 2.6a shows photographic images of the front and backside of PVDF stripe patterns (3 and 10 mm in width and length, respectively) stitched by a sewing machine. Figure 3b shows the real-time pressure sensing of PVDF stitch/nylon fabric triboelectric sensors (device area: $3 \times 10 \text{ mm}^2$) under different applied pressures, where the triboelectric current increases with the increase in pressure. The triboelectric sensors can detect the applied pressure over a broad range, from 326 Pa to 326 kPa (Figure 2.6c), and exhibit two different sensitivities of 0.66 nA kPa^{-1} and 0.1 nA kPa^{-1} in the low-pressure region ($<16.3 \text{ kPa}$) and high-pressure region (from 16.3 kPa to 326 kPa). In terms of the triboelectric voltage unit, the sensitivities are 6.23 mV kPa^{-1} and 1.12 mV kPa^{-1} in the low- and high-pressure regions, respectively (Figure 2.7). In addition, Figure 2.8 shows the force

sensing capability in low pressure region from 326 Pa to 3.26 kPa with narrow range, and the minimum detection limit of our sensor is 326 Pa. This is significantly better than the conventional textile force sensors that can only detect a narrow range of high pressure from tens of kilopascals to hundreds of kilopascals,⁴⁷ or enable only large-area pressure detection for tens of kilopascals¹⁶² and several megapascals.¹⁵⁴ Many of the previous textile sensors did not provide a broad pressure detection range and any specific detectable pressure value (Figure 2.9, Table 2.2).^{48, 138-139, 167} In addition, the sensitivity of our textile sensor is comparable to the sensitivity reported in the literatures on conventional film-type triboelectric force sensors (Table 2.3).^{47, 196-197} The washability of textile-based devices is one of the important properties for the practical applications of e-textiles. For the washability test, the triboelectric sensors (area: $26 \times 27 \text{ mm}^2$) were prepared based on PVDF-based embroidery on conductive fabric sandwiched between cotton fabrics (Figure 3d). Then, the sensors were vigorously stirred in detergent-diluted solution (1 %) by magnetic stirring for 1 h, followed by drying at 60 °C (Figure 2.10). Figure 2.6e shows the variation in triboelectric currents after different cycles of washing. Although the triboelectric outputs of the stitch fabric decreased slightly after 10 times of washing, the output signals were well retained without a significant decrease in current, even after 50 times of washing (Figure 2.6e). The current retention ratio after repeated washing is 97% of the initial current after 50 times of washing (Figure 2.6f), indicating the mechanical stability of the stitch sensor against repeated washing. Moreover, Figure 2.11 shows the mechanical stability of the stitch sensor after different cycles of folding and twisting. The triboelectric outputs of stitch fabric were well retained without a significant decrease in current, even after 100 times of mechanical deformation by folding and twisting, respectively (Figure 2.11a, b). The current retention ratio after repeated folding and twisting is 95% and 91% of the initial current (Figure 2.11c, d), respectively. It indicates the mechanical stability of the stitch sensor against repeated mechanical deformations.

To investigate the force sensing capability, PVDF stiches (Figure 2.6a) underwent contact and separation cycles with nylon fabrics as the opposite triboelectric materials (Figure 2.12). For comparison, the PVDF film sensor was also fabricated on a conductive fabric. The output current of the PVDF stitch sensor is approximately four times that of the PVDF film (Figure 2.13a). This result is attributed to the better contact between the PVDF stitch and the electrode fabric due to tight stitching by a sewing machine, compared to the PVDF film (Figure 2.14). Interconnection of the fabric to the signal acquisition elements directly affects the performance of the textile sensor.¹⁵⁸ Moreover, the output current of the PVDF stitch is much higher than the output currents of commercial PET and nylon stitches (Figure 2.13b). PET and nylon have lower electron affinity than PVDF, leading to a much smaller triboelectric signal during the contact–separation process with a nylon fabric.¹⁴ To check the effect of supportive upper stitches and fabrics, PVDF stitches were fabricated with different commercial threads (PET and nylon) as the upper stitches on different

supportive fabrics (cotton and silk). The resulting triboelectric signals did not depend on the supportive upper stitches and fabrics (Figure 2.13c). This result can be attributed to two reasons. First, the supportive stitches are barely exposed on the PVDF stitched surface, as seen in the SEM image of the stitch (Figure 2.1c). Second, PVDF stitches with submillimeter height act as a spacer to generate triboelectric charges, preventing the supportive fabrics from making contact with the upper nylon fabric.

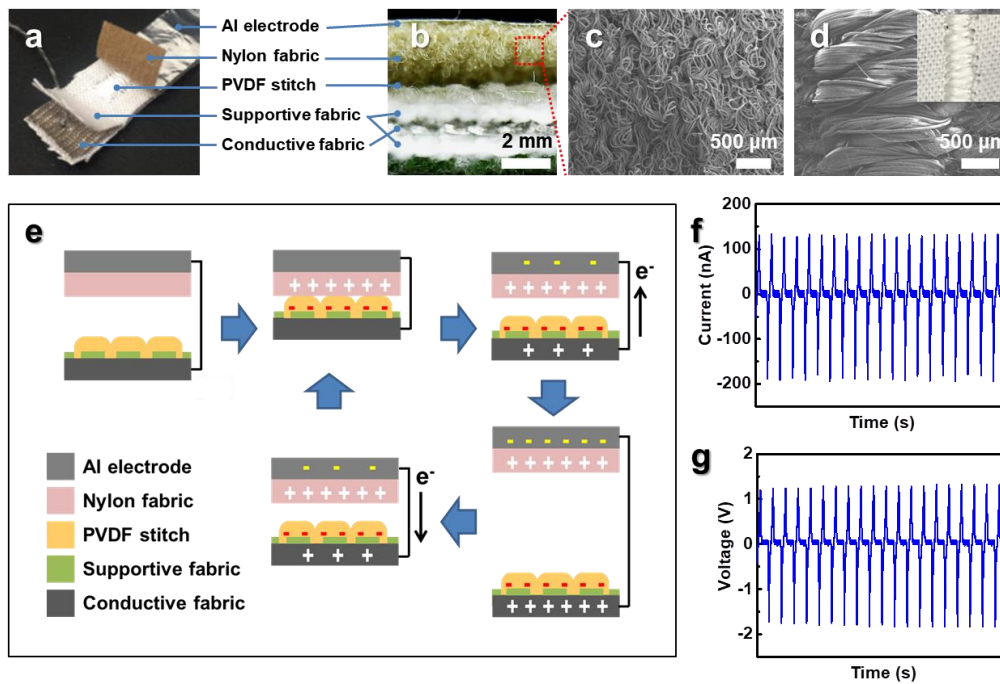


Figure 2.4. Working mechanism and triboelectric output performances of the PVDF stitch-based textile sensor. (a) Photographic and (b) optical cross-section images of the textile sensor. SEM images of (c) the nylon fabric for a positive triboelectric object and (d) PVDF stitch for a negative triboelectric object. (e) Schematic illustration of triboelectric charge generation and electron flow mechanism between the PVDF stitch and nylon fabric. Triboelectric output (f) current and (g) voltage under 9.8 N.

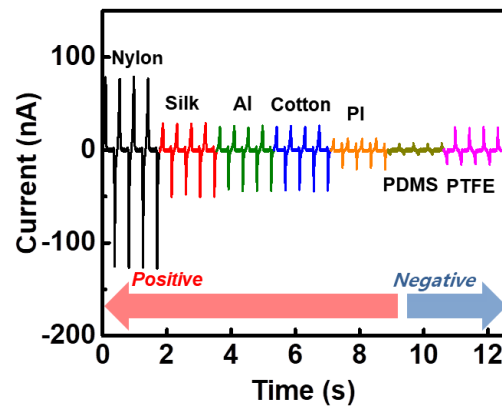


Figure 2.5. Triboelectric output current profiles of PVDF stitch textile sensor with relative contact-separation motion to different materials.

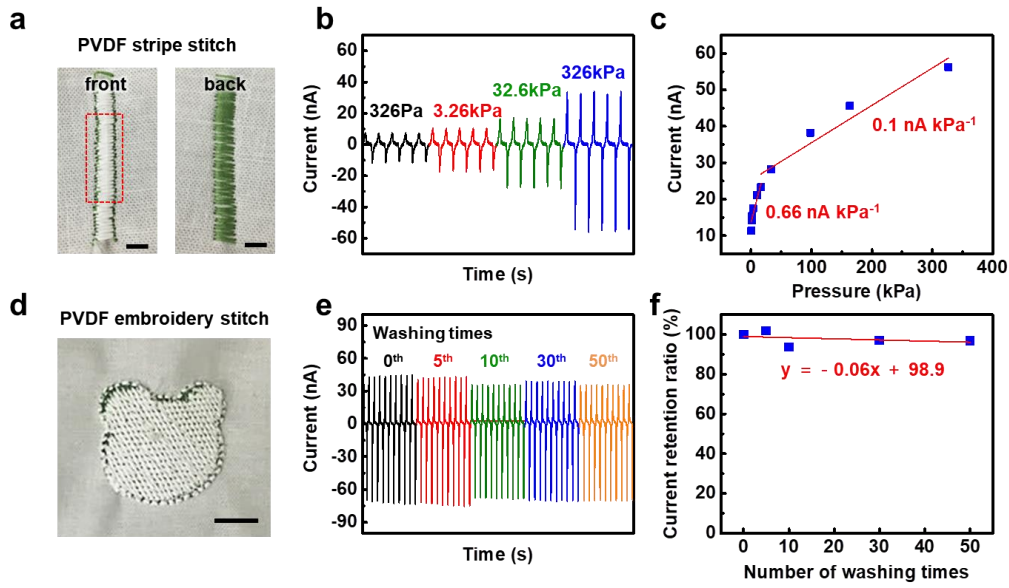


Figure 2.6. Evaluation of the PVDF stitch-based textile sensor for self-powered force sensing and washing durability. (a) A photographic image of the PVDF stitch for force sensing; the red rectangular region is under pressure (area $3 \times 10 \text{ mm}^2$) (scale bar: 10 mm). (b) Triboelectric output current as a function of time under different applied pressures. (c) Linear fitting between the triboelectric current variations and the applied pressure (326 Pa to 326 kPa). (d) A photographic image of the PVDF for the embroidery stitch washing durability test (scale bar: 10 mm). (e) Triboelectric output current of the device after 50 cycles of washing. (f) Linear fitting between the triboelectric current retention ratio and the number of washing times.

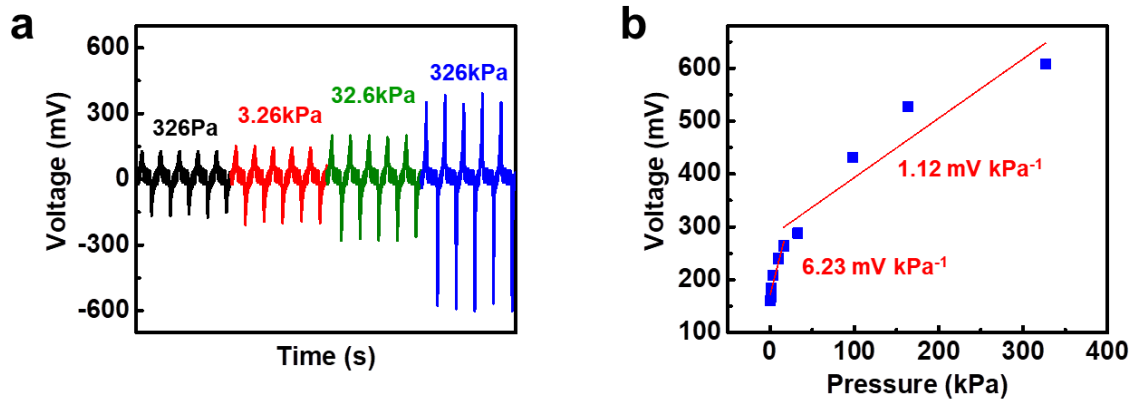


Figure 2.7. Evaluation of the PVDF stitch-based textile sensor for self-powered force sensing; (a) Triboelectric output voltage as a function of time at different pressures applied on the device. (b) Linear fitting between the triboelectric voltage variations and the applied pressure (326 Pa ~ 326 kPa).

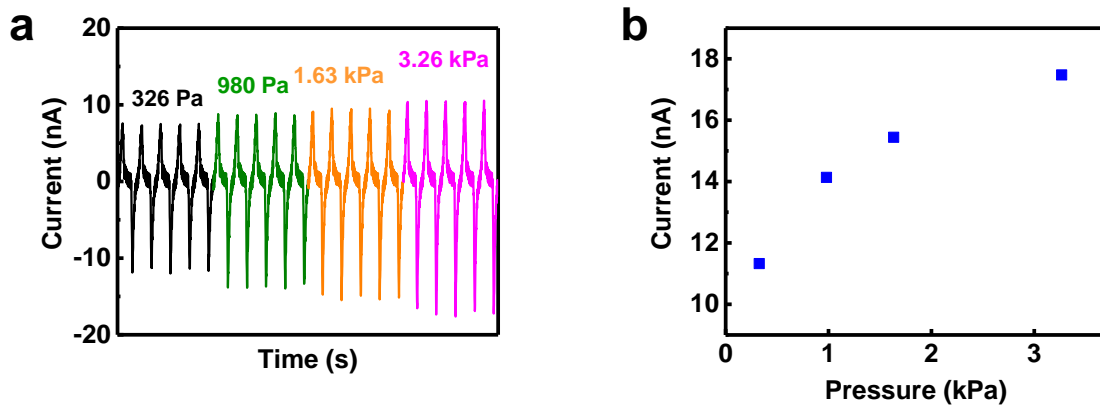


Figure 2.8. Triboelectric output signals in the low-pressure region (a) Triboelectric output current as a function of time and (b) the applied pressures from 326 Pa to 3.26 kPa in the low-pressure region.

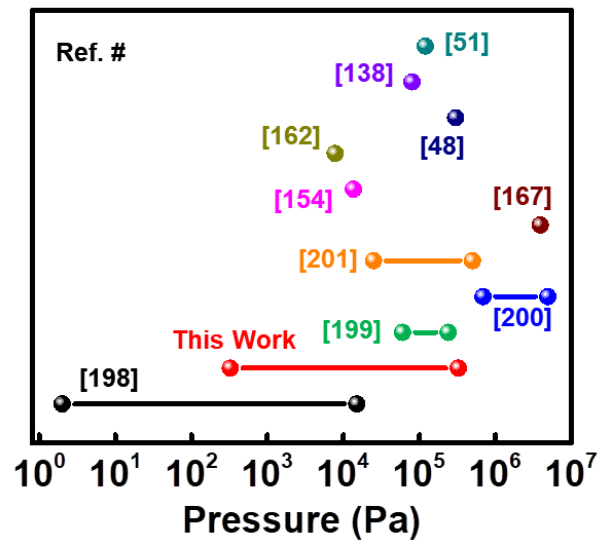


Figure 2.9. Comparison of the detectable pressure range of the results achieved in this work with previously reported triboelectric pressure sensor.^{48, 51, 138, 154, 162, 167, 198-201}

Table 2.2. Comparison of detection range of the results achieved in this work with previously reported textile-based sensors.

Textile fabrication	Basic materials	Detection range	Sensor type
Embedment	Cotton fabric coated CNT & Ni	2 Pa ~ 15 kPa	Resistive ⁴⁵
	Electrically Cu, Ni plating fabric, PE fabric	0.69 MPa ~ 4.9 MPa	Resistive ¹⁹⁸
	PET fabric with PDMS, CNT, Ag	40 kPa ~ 240 kPa	Triboelectric ⁴⁷
	Conductive thread stripes, synthetic elastic foam	~13.6 kPa	Capacitive ¹⁹⁹
	Conductive fabric, 3D textile	~ 7.8 kPa	Capacitive ²⁰²
	Ag-coated textile, Proprietary Closed Cell Resin	~ 300 kPa	Capacitive ²⁰⁰
Hand weaving	Kevlar coaxial thread coated with SBS/AgNP	~ 3.9MPa	Capacitive ¹⁵⁴
	PVDF strap with electrode Hollow PDMS tube	~ 80kPa	Piezoelectric, Capacitive ¹⁶²
	Commercial stainless steel/PET fiber coated with PDMS	-	Triboelectric ⁴⁸
	PET fabric coated with Ni & Parylene	-	Triboelectric ¹⁶⁷
Machine-weaving	PET thread coated with Cu & PI	-	Triboelectric ¹³⁸
	Metallic stripes, semi conductive fabric	25 kPa ~ 500 kPa	Resistive ²⁰³
Machine-knitting	Nylon fiber coated with graphene & nylon	-	Triboelectric ¹³⁹
Sewing machine stitching	Ag-coated conductive thread, 3D textile	~ 120 kPa	Capacitive ²⁰⁴
	As-spun PVDF on conductive fabric	326 Pa ~ 326 kPa	Triboelectric (This work)

Table 2.3. Comparison of detection range and sensitivity of the results achieved in this work with previously reported triboelectric pressure sensors.

Type	Basic materials	Detection range	Sensitivity
Film ²⁰⁵	PDMS, Al	0.6 ~ 30 MPa	6 MPa ⁻¹ (0.6 ~ 200kPa), 0.037 MPa ⁻¹ (350 kPa ~ 30 MPa)
Film ²⁰⁶	PDMS, Liquid	0.4 ~ 40 N	0.036 nA N ⁻¹
Film ¹⁹⁷	PDMS, Al	1 ~ 150 kPa	0.06 kPa ⁻¹ (1~80 kPa)
Film ²⁰¹	PVDF-TrFE, PDMS	0.05 ~ 600 kPa	104 mV kPa ⁻¹ (0.05~5 kPa), 55 mV kPa ⁻¹ (5~60 kPa), 49 mV kPa ⁻¹ (60~600 kPa)
Film ¹⁹⁶	Cu/PDMS, PTFE	~50N	0.019 μ A N ⁻¹ (0 ~ 40 N)
Film ²⁰⁷	PDMS	40 ~ 140 N	28 mV N ⁻¹
Textile ⁴⁷ (embedment)	PET fabric with PDMS, CNT, Ag	40 kPa ~ 240 kPa	-
Textile (sewing machine stitching)	As-spun PVDF on conductive fabric	326 Pa ~ 326 kPa (9.8 mN ~ 9.8 N)	0.66 nA kPa⁻¹, 6.23mV kPa⁻¹ (0.326 ~ 16.33 kPa), 0.1 nA kPa⁻¹, 1.12 mV kPa⁻¹ (16.33 ~ 326 kPa)



Figure 2.10. Washing durability of PVDF stitch textile sensor; Demonstration of the washing environment with commercial detergent by magnetic stirring.

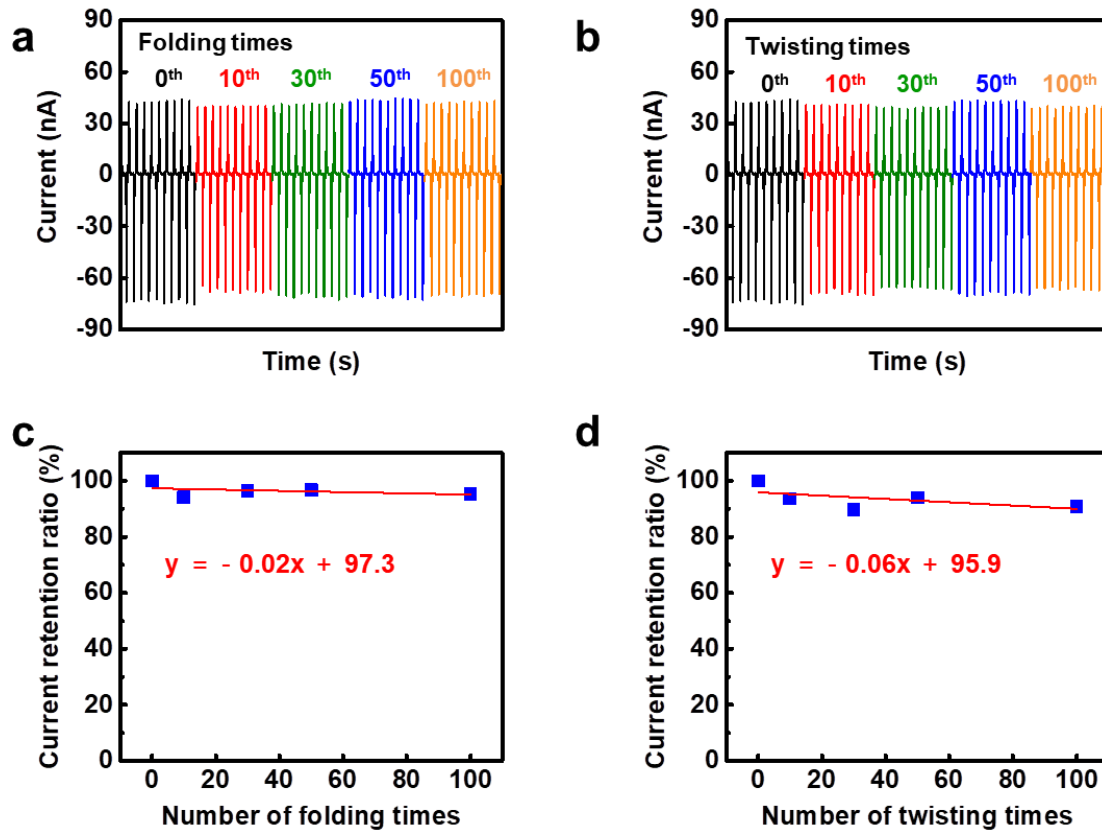


Figure 2.11. Evaluation of the PVDF stitch-based textile sensor for mechanical stability. (a, b) Triboelectric output current of the device after 100 cycles of mechanical deformation by folding and twisting. (c, d) Linear fitting between the triboelectric current retention ratio and the number of mechanical deformation times.

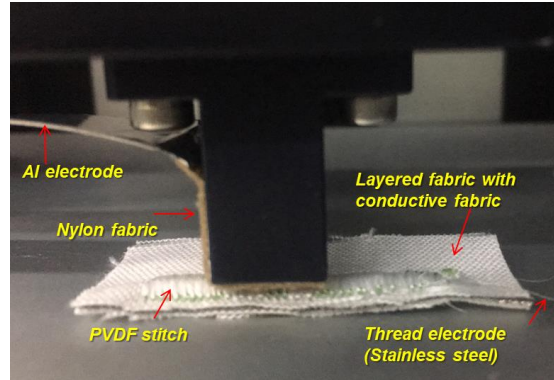


Figure 2.12. Experimental image of contact-separation motion between PVDF stitch and nylon fabric.

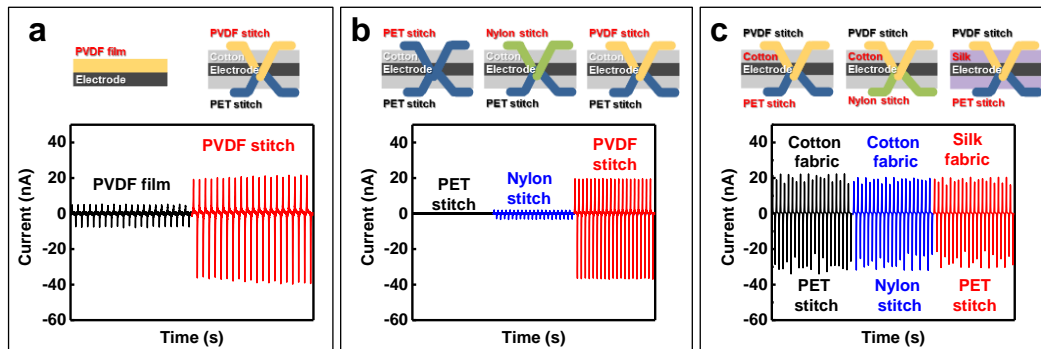


Figure 2.13. Outstanding triboelectric output performance of the PVDF stitch-based textile sensor. Comparison of the output currents from the PVDF stitch-based device with (a) PVDF film and (b) other commercial thread stitch. (c) The output current independent of the supportive stitch and substrate fabric.

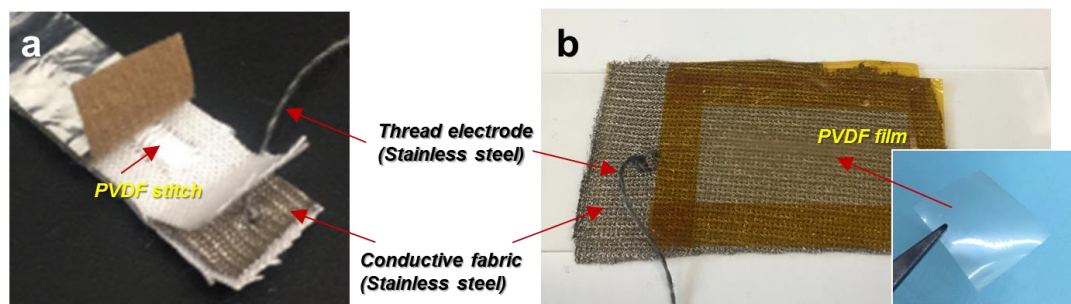


Figure 2.14. Comparison of both types of PVDF sensor. (a, b) Photographic images of (a) the stitch-based sensor and (b) the film-based sensor.

Applications for self-powered diverse sensing

The facile fabrication of programmable PVDF stitch patterns by a sewing-machine enables realizing textile-based triboelectric devices with application-specific stitch patterns, which are advantageous for diverse applications in self-powered sensors. In this work, we demonstrated a smart textile pad for body motion and hand gesture recognition using PVDF-stitch triboelectric sensors. Figure 2.15a shows the PVDF stitch sensor that can be sewn on the elbow part of a cloth for monitoring elbow movements. The PVDF stitch and the nylon cloth on the skin can function as negative and positive triboelectric materials, respectively. The PVDF thread was stitched on a multi-layered fabric pad composed of supportive cotton fabric, conductive fabric, and nylon joint pad 1. Then, the multi-layered fabric pad with PVDF stitches can be worn over joint pad 2 for forming opposite triboelectric contact surfaces. For the stitch sensor, we used a single electrode-based triboelectric system that is widely used for wearable electronics owing to its facile fabrication process and high efficiency for moving objects.²⁰⁸⁻²⁰⁹ The working mechanism of the PVDF-stitch-based single electrode sensors is illustrated in Figure 2.16. Owing to the difference in electron affinity between PVDF and nylon, electrons were injected from the nylon fabric to the PVDF stitch when the two materials came in contact with each other owing to the contact electrification. When the PVDF stitches are separated from the nylon fabric, the negative charges of the PVDF stitches can induce positive charges on the electrode, driving free electrons to flow from the electrode to the ground. When the two objects approach each other again, electrons flow inversely to attain a charge balance. Then, charge neutralization occurs again when the PVDF stitch is fully in contact with the nylon fabric. Repeated contact-separation movements between the two materials by hand gestures and body motions induce intrinsic current outputs. As a result, various motions of the wrist, elbow, ankle, and knee can be detected (Figure 2.15b). For the recognition of different motions in each joint, our sensor can be used for the recognition of motion strength by analyzing different intensity signals depending on the motion strength (Figure 2.17).

In another application, when the PVDF threads are stitched into the knuckle regions of a textile glove, a smart glove can be fabricated for the hand gesture-recognition. Figures 2.15c and d show that the smart glove can detect and distinguish various hand gesture signals for different numbers as well as gestures indicating rock, paper, scissors, etc. When repeating the hand gestures from i to vi, the smart glove generated an intrinsic triboelectric output current that can discriminate the hand gesture signals for different numbers. This result demonstrates that the smart glove with PVDF-stitch-based triboelectric sensors can distinguish specific hand gestures in real time. In addition, the PVDF stitches can be used for identifying Morse code by detecting the triboelectric output current when a user touches the PVDF stitches on the smart glove. Temporal or static touches on the PVDF stitches can

induce short or long triboelectric signals that can signify the sequences of dot and dash signals in Morse code. Therefore, the simple touch of the smart glove with PVDF stitches can transmit specific information of a user as electronic signals. Figure 2.15e shows the generated signals that represent the phase of “UNIST” in Morse code. For example, the Morse code of “U” is composed using two successive dots and one dash. When applying two successive temporal touches and following a static touch on the smart glove, we can obtain two short and one long triboelectric signal that can transmit the letter “U” as electronic signals. To dissociate the last signal of the specific letter from the first signal of the following letter, we used an obvious time interval between each letter.

Monitoring of foot pressure distribution is important in gait and posture analysis for the foot wear design, sports biomechanics, and wearable healthcare systems.¹²⁷ In particular, it can be used in diagnosing several diseases such as diabetic foot ulcers and Parkinson’s disease from abnormal gait patterns.²¹⁰⁻²¹¹ Wearable pressure sensors enable the monitoring of the walker’s gait patterns and posture.^{125, 212} Our stitch sensor can be also used for the monitoring of foot pressure distribution. In particular, compared to previous wearable pressure sensors, our stitch sensor is more appropriate for wearable foot pressure monitoring system because of its inherent characteristics of deformability, comfort, and breathability. Moreover, it is suitable to fabricate stitch sensors with programmable patterns for both aesthetic and functional form factors. Figure 2.18a shows a schematic illustration of the PVDF stitch sensor array for the monitoring of foot pressure. The PVDF stitch sensor array (3×4 pixel) with programmed textile patterns can be readily fabricated by a sewing machine (Figure 2.18b). Figure 2.18c shows the schematic of walking motions on the PVDF stitch sensor array and their corresponding contour mapping images of foot pressure distribution. Our PVDF stitch sensor array was capable of monitoring of foot pressure distribution during walking, where red and blue areas indicate high and low pressure, respectively. This foot pressure monitoring capability of our stitch sensor can be used for the posture correction and rehabilitation in wearable medical devices and sports industry.

The PVDF stitch sensor can also monitor artery pulse pressure when attached to the neck. The artery pulse signal is used as one of the vital signs to monitor the physical and mental state of a person.² Our stitch sensor enables the simultaneous monitoring of artery pulse pressure when attached to the neck skin above the carotid artery (Figure 2.19a). One advantage of sewing machine stitching is that arbitrary stitch patterns can be generated for the desired fashionable patterns on the triboelectric sensors, as seen in Figure 2.19a. Figures 2.19b, c show the resulting triboelectric output of pulse pressure with three distinguishable peaks (P_1 , P_2 , and P_3). Herein, P_1 is the main pulse pressure which is the difference between the systolic (P_{Sys}) and diastolic (P_{Dia}) pressures and is generated from the blood flow ejected by heart contraction. P_2 and P_3 are the reflected wave pressures caused by the

waves reflected from the peripheral sites (P_2 from the hand and P_3 from the lower body).²¹³ These parameters can be used to extract the radial artery augmentation index ($AI_r = P_2/P_1$) and round-trip time of a reflected wave from the hand periphery (T_r); these quantities are related to arterial stiffness depending on the age of people.²¹³ Figures 2.19d and e exhibit the artery pulse signals of a healthy female in her early thirties before and after physical exercise. After physical exercise, the pulse rate increased from ~69 beats per minute (BPM) to ~137 BPM and the signal intensity also increased owing to the increased cardiac output to rapidly supply blood to the activated muscles. Moreover, the average values of the augmentation index ($AI_r = 0.55$) are consistent with the literature data of healthy females in their early thirties; the value decreased to 0.27 after physical exercise (Figure 2.20). This decrease in the augmentation index indicates the decreased arterial stiffness owing to the vasodilation of the muscular arteries.²¹³⁻²¹⁴ This result demonstrates that our stitch sensors have potential as a self-powered wearable diagnostic sensor to monitor human health in real time. Table 2.4 (Supporting Information) compares the specifications of our sensor with the other textile-based sensors fabricated by embedding sensors in commercial textiles^{1, 45-47, 166, 215} and conventional textile fabrication techniques such as weaving,^{48, 50-51, 138, 154, 162, 164, 167} knitting,^{52-53, 139, 216} and sewing.^{163, 173, 176} Most of the conventional textile sensors are not washable owing to the lack of mechanical strength and coating-detachment issues. Moreover, sophisticated textile sensors cannot be fabricated by most approaches except for metal patterning with electroless deposition,⁴⁵ stencil printing,⁴⁶ industrial machine-knitting⁴ and computerized sewing techniques.^{173, 176} However, these approaches involve expensive and complicated processes to fabricate sophisticated e-textile sensors. Although existing stitch sensors can be fabricated by relatively low-cost and simple processes, they need external power sources for operation. On the other hand, our self-powered PVDF stitch sensors do not need an external power source. In addition, our all-textile structure with washability and arbitrary textile patterns is advantageous in diverse wearable sensor applications.

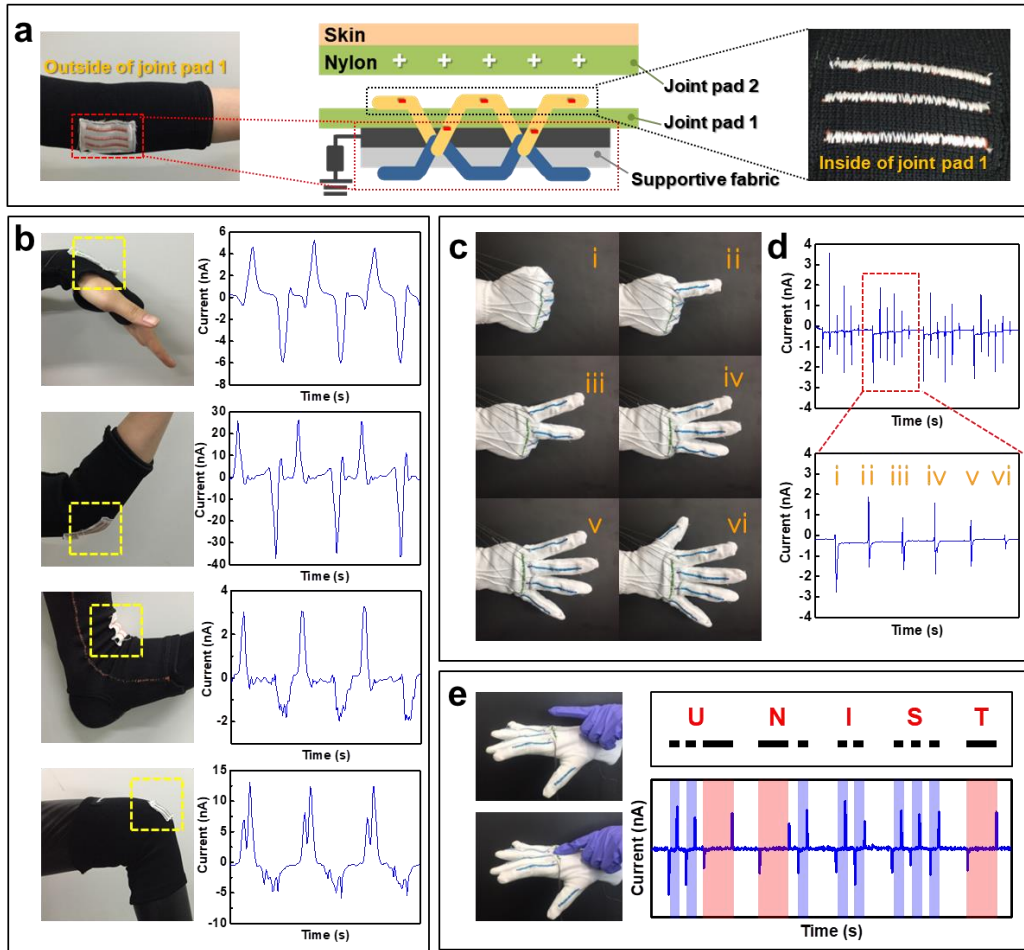


Figure 2.15. Real-time detection of different body motions and hand gestures using the self-powered PVDF-textile sensor. (a) A schematic illustration of the working mechanism of the PVDF stitch-based textile sensor attached to the joint pad. (b) Photographic images and intrinsic output current signals obtained by detecting various motions of the wrist, elbow, ankle, and knee; the body motion monitoring patch ($40 \times 60 \text{ mm}^2$) was composed of 3-lines of stitch with $3 \times 45 \text{ mm}^2$. (c, d) Photographic images and intrinsic output current signals by detecting (c) various body motions (the wrist, elbow, ankle, and knee) and (d) various hand gestures for different numbers; the smart glove was composed of 6-lines of stitch with $3 \times 50 \text{ mm}^2$. (e) Demonstration of the self-powered human-system interaction interface with Morse codes by touching the triboelectric stitch with finger, representing a word “UNIST.”

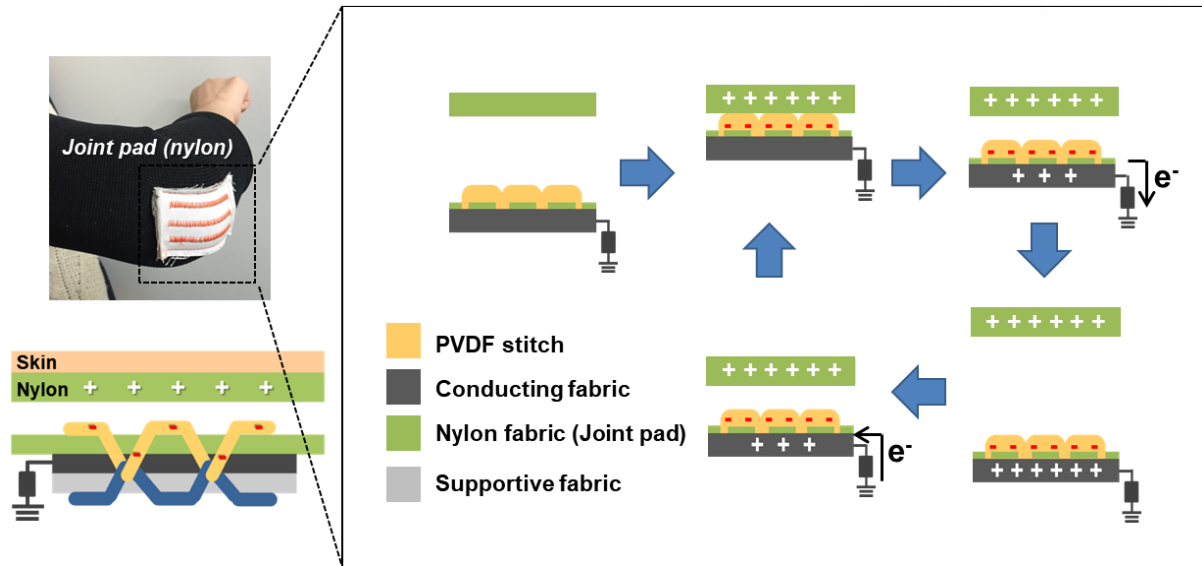


Figure 2.16. Working mechanism of PVDF stitch-based textile sensor as a body-motion sensor; Schematic illustration of triboelectric charge generation and electrons flow mechanism with single electrode system.

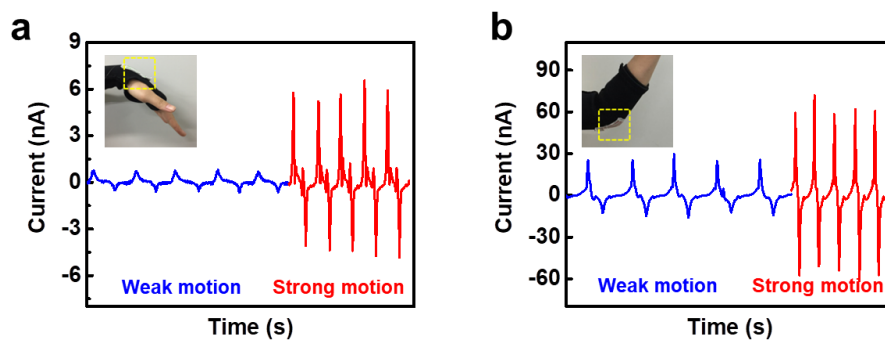


Figure 2.17. Real-time detection of body motion with different strength; (a) Output current signals from wrist movements with weak and strong motion. (b) Output current signals from elbow movements with weak and strong motion.

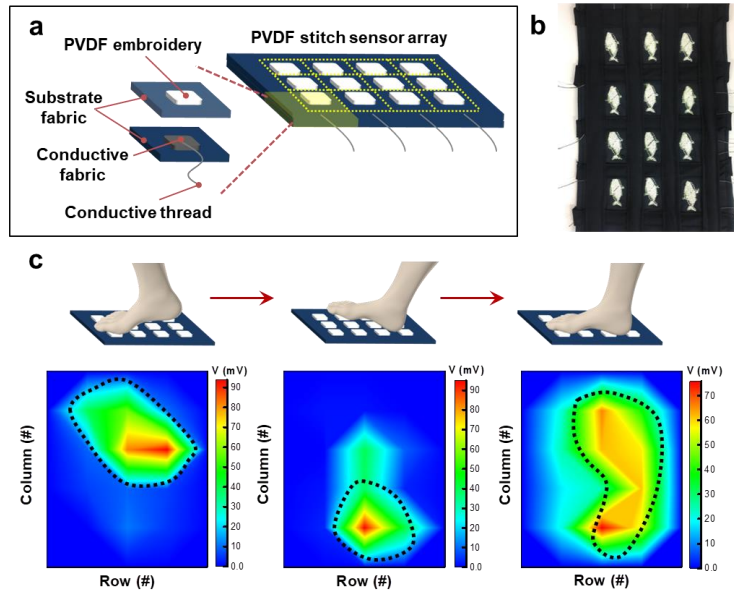


Figure 2.18. Self-powered foot pressure mapping based on the PVDF stitch sensor array. (a) A schematic illustration of the PVDF stitch sensor array device. (b) Photograph of 3×4 pixel arrays of PVDF stitch sensor with fish-shaped embroidery; the foot pressure sensor ($150 \times 230 \text{ mm}^2$) was composed of 12 pixels with $10 \times 30 \text{ mm}^2$. (c) Schematics of walking motions on PVDF stitch sensor array and their corresponding contour mapping images.

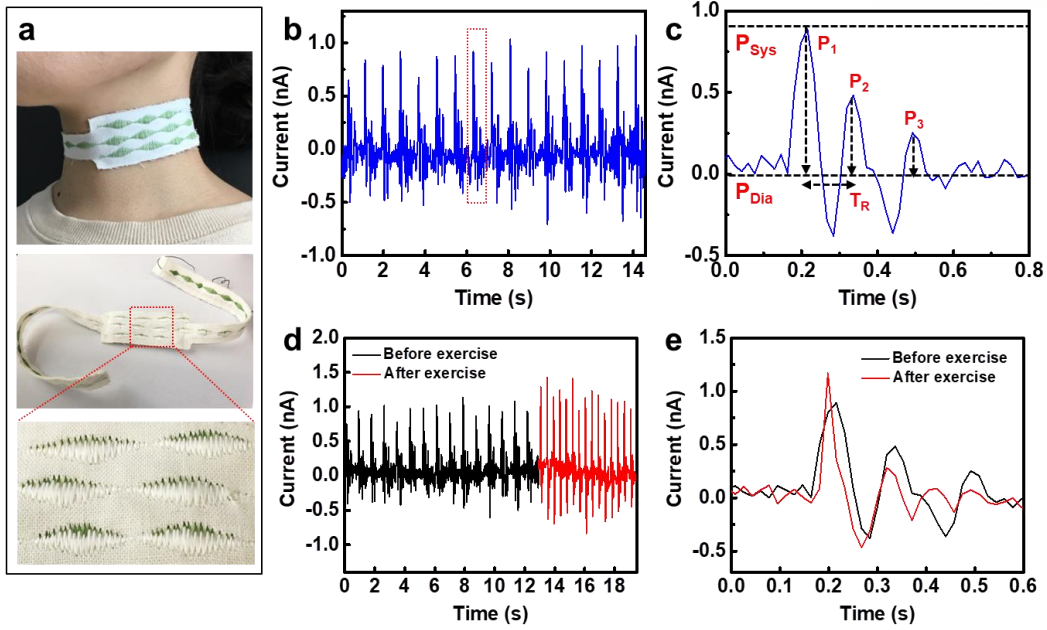


Figure 2.19. Real-time detection of pulse pressure using the self-powered PVDF-textile sensor. (a) Photographic images of the fashionable garment-type triboelectric sensor with arbitrary stitch patterns for pulse pressure detection; the pulse pressure sensor ($70 \times 30 \text{ mm}^2$) was composed of 11 diamond patterned stitches ($20 \times 5 \text{ mm}^2$). (b) Real-time monitoring of the pulse pressure and (c) expanded pulse wave consisting of three peaks corresponding to the pulse pressure (P_1) and reflected waves from the hand (P_2) and lower body (P_3). (d–e) Variation in the pulse pressure wave before and after physical exercise.

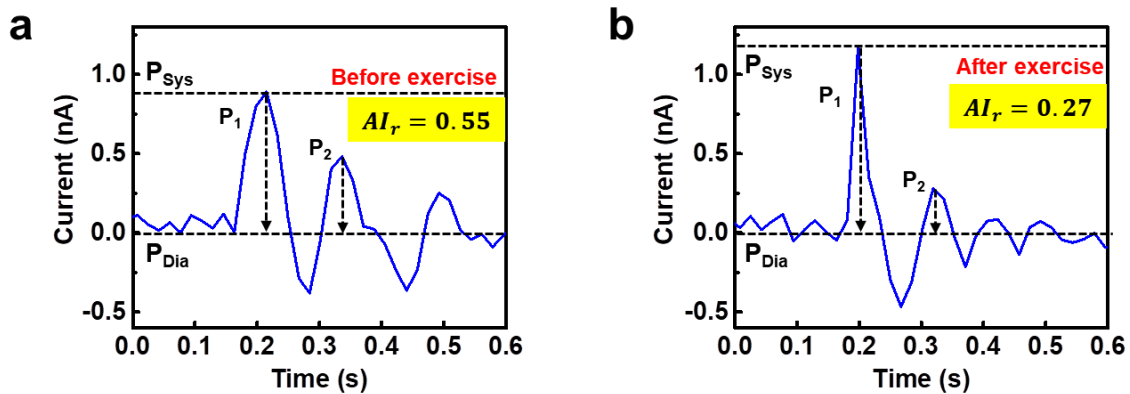


Figure 2.20. Comparison of augmentation index (AI_r) before and after physical exercise.

Table 2.4. Comparison of fabrication conditions and washability of the results achieved in this work with previously reported textile-based sensors.

Method	Key materials	Electrode	Substrate	Delicate pattern	Washable	Sensor type
Embedment in commercial thread or fabric						
Coating	Carbonized silk	-	Silk fabric	-	-	Resistive ¹⁵³
CNT coating & Ni plating	CNT coated fabric & Ni	-	Cotton fabric	△	-	Resistive ⁴⁵
Stencil printing	Ag-fluoroelastomer	-	Knitted fabric (Nylon/PU)	△	○	Resistive ⁴⁶
Coating	PDMS, PET,	Aligned CNT, Ag paste	PET fabric	-	-	Triboelectric ⁴⁷
Coating	PDMS-AgNW, PTFE, PU-AgNW	AgNW	PU fiber	-	-	Triboelectric ¹⁶ ₆
Layering	Cu, Ni- electroplating fabric, PE	Cu, Ni	PE fabric	-	-	Capacitive ¹⁹⁸
Layering	Conductive thread stripes, synthetic elastic foam	Conductive thread	Synthetic elastic foam	-	-	Capacitive ¹⁹⁹
Layering	Conductive fabric, 3D textile	Conductive fabric	Conductive fabric, 3D textile	-	-	Capacitive ²⁰²
Layering	Ag-coated textile, Proprietary Closed Cell Resin	Ag	-	-	○	Capacitive ²⁰⁰
Conventional textile fabrication technique						
Weaving (by hand)	PDMS	SBS/AgNP	Kevlar fiber	-	-	Capacitive ¹⁵⁴
	PVDF, PET	Metal	Elastic hollow tube	-	-	Piezoelectric, Capacitive ¹⁶²
	CNT & PTFE	CNT	Cotton thread	-	-	Triboelectric ¹⁶⁴
	PDMS, Au-coated Al	Au-coated ZnO NWs/Al wire	Al wire, Al foil	-	-	Triboelectric ⁵⁰
	PVDF-TrFE, Ag	CNT, Ag-coated nylon yarn	PU fiber	-	-	Triboelectric ⁵¹
	PDMS, stainless-steel/PET thread	Stainless-steel/PET thread	Stainless-steel/PET thread	-	○	Triboelectric ⁴⁸
	Ni & parylene	Ni	PET fabric	-	-	Triboelectric ¹⁶⁷
Weaving (by Industrial weaving loom)	Cu, PI	Cu	PET thread	-	○	Triboelectric ¹³⁸
	Metallic stripes, semi-conductive fabric	Metallic stripes	Normal fabric	-	-	Resistive ²⁰³

Conventional textile fabrication technique						
Knitting (by hand)	PDMS, stainless- steel/PET thread	Stainless steel/PET thread	Stainless steel/PET thread	-	○	Triboelectric ⁵²
Knitting (by Harry Lucas circular knitting machine)	CNT-wrapped spandex fiber	-	Spandex fiber	-	-	Resistive ²¹⁶
Knitting (by Industrial knitting machine)	PTFE thread, Ag thread	Ag thread	-	Plain-, double-, rib patterns	-	Triboelectric ⁵³
Knitting (by STOLL computerized flat knitting machine)	PTFE, Nylon	Graphene	Nylon fiber	-	-	Triboelectric ¹³⁹
Sewing (by hand)	Graphene nano platelets	-	Commercial yarn	-	-	Resistive ¹⁶³
Stitching (by sewing machine)	Ag/AgCl or carbon coated PET thread	Ag/AgCl or carbon coated PET thread	PET thread	△	-	Electro- chemical ¹⁷³
	Melt-spun coaxial polymer optical fiber	-	Polymer optical fiber	△	○	Photonic ¹⁷⁶
	Ag-coated conductive thread, 3D textile	Ag-coated conductive thread	Non- conductive textile	-	○	Capacitive ²⁰⁴
	As-spun PVDF fiber	Ag conductive fabric	Various fabric (Cotton, Silk)	Various patterns, Letters, Embroidery	○	Triboelectric (This work)

2.4 Conclusions

In summary, PVDF-stitch-based triboelectric sensors have been demonstrated by using a sewing machine for the first time. We showed that the operation of a sewing machine with the dry-jet wet spun PVDF fibers was feasible owing to the strong mechanical properties. The resulting PVDF stitches on commercial fabric can generate the triboelectric output signals through contact and separation with another commercial fabric (nylon) owing to different electron affinity. Because of the all-stitched structures, PVDF stitch sensors are not only flexible, lightweight, and wearable but also comfortable. In addition, the sensing performances of the stitch sensor were well retained without significant decrease even after repeated washing cycles, demonstrating that the suggested PVDF stitch sensor can be utilized for practical applications. For active sensing applications, a smart glove and joint pads with PVDF stitches were fabricated based on commercial clothing products. These active sensors based on PVDF stitches can detect and distinguish various hand gestures and body motions. In addition, the self-powered stitch sensor can monitor the pulse signal in real time. We demonstrated that PVDF stitch sensors can be readily fabricated onto commercial fabrics using a sewing machine. Our proposed strategy can be easily extended for other functional applications when integrating with diverse stitch patterns, and functional materials, paving a new way for the facile, low-cost and large-scale fabrication of self-powered wearable sensors in commercial clothes and garments.

Chapter 3. Triboelectric/pyroelectric multimodal sensors with decoupled pressure and temperature multiple stimuli *via* ferroelectric polarization

3.1 Introduction

Internet of things (IoT) have attracted great interest and boosted the rapid development of wearable, wireless and self-powered sensors, which bring great benefits in the daily life healthcare,¹⁻³ intelligent control,⁵ daily activity monitoring,^{2, 4} and human-machine interface systems.⁶ Accordingly, multimodality in simultaneous sensing of pressure and temperature without energy loss and signal interference has been investigated to meet the requirements of smart wearable sensors.¹¹⁻¹² For these applications, piezoelectric,¹⁸⁻¹⁹ pyroelectric,²⁰⁻²¹ thermoelectric,²²⁻²³ and triboelectric^{14-17, 172, 217} effects have been extensively studied to develop self-powered multifunctional devices. However, most of conventional self-powered sensors realize multifunctional sensing by integrating individual sensors for each pressure and temperature, which can limit their applications.¹⁴⁰⁻¹⁴³ Although simultaneous multimodal sensors have been developed, most sensor needs external working bias.^{11-12, 92, 141, 143-144} Therefore, new approaches to develop self-powered multimodal sensors are necessary, which enables the discrimination of multiple pressure and temperature without signal interference.

P(VDF-TrFE), a ferroelectric polymer with a good piezoelectric and pyroelectric response, has been widely used for multimodal sensing devices due to its ease of processing as well as flexibility. However, conventional multimodal sensors based on ferroelectric polymer cannot clearly distinguish the simultaneously applied pressure and temperature due to the signal interference resulting from low piezoelectric output performances.^{140, 142} Meanwhile, P(VDF-TrFE) have frequently been used for triboelectric devices due to its strong electro-negativity in the triboelectric series. Because the applied external electric field greatly affects the polarization state which relies on the aligned dipoles in ferroelectric polymers,^{36, 87} triboelectric devices have been demonstrated based on polarization-tuned ferroelectric polymers.^{62, 111, 113-117} Several researchers have suggested approaches to boost the output power of PVDF-based composites by the electrical poling process, enhancing the triboelectric charge density.^{62, 113} Another approach is the use of high dipole moment solvent to induce the high crystallinity and dipole alignment of the polymer, which considerably enhances the triboelectric output power.¹¹¹ In addition, several researches have suggested approaches to modulate the direction as well as the amount of charge transfer in triboelectricity by ferroelectric polarization.^{114, 116-117, 218} However, contact electrification has not been demonstrated between identical materials with identical triboelectric polarity. Generally, output performance of triboelectric devices relies on the selection of triboelectric contact pair materials with large differences in polarity in triboelectric series.²¹⁸⁻²²⁰ Although triboelectric devices based on identical materials in contact pairs enable the facile

fabrication of triboelectric devices without complicated additional processes on the selected pair materials, identical materials have not been considered for triboelectric contact pairs because the contact electrification is usually not observed between identical materials. Therefore, further research is necessary for the high performance self-powered devices through the facile fabrication approach based on identical materials in triboelectric contact pairs, which are capable of sensing and discriminating temperature as well as mechanical force variations via pyroelectric and triboelectric effects.

Herein, we report the fabrication of self-powered multimodal pressure and temperature sensors based on polarity-modulated ferroelectric P(VDF-TrFE). Although an identical material is used for triboelectric contact pairs, remarkable triboelectric output performance can be obtained because contact electrification can be controlled by switching the aligned direction of dipoles depending on the applied polarization bias. Moreover, noticeable pyroelectric output performance can be achieved by ferroelectric polarization even with the triboelectric device structure that is different from the conventional pyroelectric devices with the ferroelectric films sandwiched between two electrodes. To the best of our knowledge, multimodal triboelectric and pyroelectric devices using an identical material with easily switchable polarity by electrical polarization have not been reported yet. Our sensor provides a broad range of pressure detection capability (98 Pa to 98 kPa) and high sensitivity (40 nA kPa^{-1} and 1.4 V kPa^{-1}) in the subtle pressure range ($< 19.6 \text{ kPa}$) as well as temperature detection capability with high sensitivities of $0.38 \text{ nA } ^\circ\text{C}^{-1}$ and $0.27 \text{ nA } ^\circ\text{C}^{-1}$ in the cooling ($-20^\circ\text{C} < \Delta T < -2.5^\circ\text{C}$) and heating ($2.5^\circ\text{C} < \Delta T < 20^\circ\text{C}$) state, respectively. In addition, our sensor can provide two different approaches for simultaneous temperature and pressure sensing and discrimination. One is based on the opposite directional signals to respond the simultaneously applied pressure and temperature, especially under negative temperature change ($\Delta T < 0$), which is due to the opposite electron flow from triboelectric and pyroelectric effects. The other is the use of different response and saturation times of triboelectric and pyroelectric effects. Owing to the high sensing performances and unique structure, our sensor can be utilized for the monitoring of weak pulse pressure of carotid artery as well as multimodal finger touch. Our work provides a feasible approach to develop high-performance triboelectric and pyroelectric hybrid devices based on identical contact pair materials via ferroelectric polarization.

3.2 Experimental details

Synthesis of β phase of P(VDF-TrFE) film and fabrication of devices

P(VDF-TrFE) solution (20 wt%) was prepared by dissolving 70/30 P(VDF-TrFE) copolymer powder (PIEZOTECH, France) in 99.5% N,N-dimethylformamide (DMF). P(VDF-TrFE) solution was spin-coated on Cu substrate (1000 rpm, 60 s) ($\sim 22^\circ\text{C}$, $\sim 23\%$ RH), followed by drying at 70°C for 1 h to remove the DMF solvent. P(VDF-TrFE) film thickness ($\sim 15\ \mu\text{m}$) was optimized for the stable electrical polarization without leakage current, which enhanced the output performance of our multimodal sensor. For enhancement of crystallinity of β phase, the film was annealed at 140°C for 2 h and followed by gradual natural cooling to room temperature. The electrical poling was carried out under an external electric field ($50\ \text{MVm}^{-1}$) for 30 minutes to align the electric dipoles. For the fabrication of free-standing triboelectric devices ($\sim 2 \times 2\ \text{cm}^2$), as-prepared P(VDF-TrFE) films on electrodes were attached to each other using polyimide double-sided tape which was also used as spacer.

Characterization

The structural analysis of the β phase of P(VDF-TrFE) films were verified by X-ray diffractometer (D8 Advance, Bruker) with monochromatic Cu K α radiation ($\lambda = 0.15406\ \text{nm}$) and Fourier transform infrared (FT-IR) equipment (670-IR, Varian). All of the topography, piezoresponse force microscopy (PFM) and Kelvin probe force microscopy (KPFM) measurements were acquired using a commercial atomic force microscope (XE-70, Park Systems Corp.) at room temperature. PFM images were measured in dynamic-contact electrostatic force microscopy (DC-EFM) mode. The KPFM images were obtained in non-contact mode. The Au coated conducting tip was modulated by applying sinusoidal voltage of 1.5 V (rms) at a frequency of 15 kHz using a lock-in amplifier (SR-830, Stanford Research Systems). The contact potential difference (CPD) was obtained by applying DC feedback voltage to nullify the first harmonic signal, which is proportional to the electrostatic force component between the tip and the sample. We employed the frequency modulation (FM) mode for feedback. In each measurement, we compared the surface potential difference between the AFM tip and highly oriented pyrolytic graphite (HOPG) to normalize the tip effect. The open-circuit voltage and short-circuit current were measured by using an oscilloscope (DPO 2022B, Tektronix, US) and a source meter (2450-SCPI, Keithley, US), respectively. The output characteristics of the sensor were measured by applying a periodic force using a pushing tester (JIPT-100, JUNIL TECH, Korea).

3.3 Results and discussions

Modulation of identical P(VDF-TrFE) for inverse triboelectric series materials

P(VDF-TrFE) has distinct dipoles when it has the all trans (TTT) planar zigzag structure (β phase), inducing a net charge,^{87, 114, 221} which can be confirmed by Fourier transform infrared spectroscopy (FTIR) and X-ray diffraction. The absorption bands at 1288 cm^{-1} and 850 cm^{-1} are related to the ferroelectric β phase in the FTIR spectrum (Figure 3.1a), and the outstanding XRD peak at $2\theta = 19.9^\circ$ is associated with (110) and (200) reflection of the crystalline β -phase (Figure 3.1b).^{87, 116, 222} Further alignment of the polymer chains in β phase P(VDF-TrFE) films can be performed by the post electrical poling process. Figures 3.1c-e show piezo response force microscopy (PFM) topology, phase and amplitude analysis of in-situ β -phase polarized P(VDF-TrFE) films. Figures 3.1d and e show a clear contrast in the phase and amplitude between the positively and negatively polarized P(VDF-TrFE) films. PFM results indicate that P(VDF-TrFE) films could be negatively and positively polarized depending on the applied bias direction. Before the electrical polarization of P(VDF-TrFE), the net charge is zero when dipoles are randomly arranged in β phase. When a large bias is applied across the films, the dipoles are aligned in P(VDF-TrFE) films, inducing the net charge in the films.²²¹

Electrically polarized P(VDF-TrFE) films have aligned dipoles in a certain direction while non-polarized one has randomly oriented dipoles (Figure 3.2a). Negative polarized P(VDF-TrFE) film is negatively charged, while positive polarized one is positively charged when rubbed with Al surface. Figure 3.2b and 3.3 show the triboelectric output signals with different polarization. Polarized films induce noticeably enhanced triboelectric output signals due to the aligned dipoles compared to non-polarized one. In addition, different polarization directions cause different shapes of triboelectric output signals. An upside peak appears when negatively polarized film is pressed with Al, while a downside peak appears when released. On the other hand, opposite behaviors were observed with positively polarized films. This result indicates that the triboelectric polarity of identical P(VDF-TrFE) film could be switched to the opposite directions through electrical polarization. Figure 3.4 shows the duration of the tuned triboelectric polarity. The opposite shape of signals from both negatively (Figure 3.4a) and positively (Figure 3.4b) polarized films can be maintained even after 24 hours. In addition, Figure 3.5 shows negligible piezoelectric output signals compared to triboelectric ones from the polarized PVDF-TrFE film under the same condition (98 kPa), indicating that the signals mainly come from the triboelectric outputs rather than piezoelectric ones.

The Kelvin probe force microscope (KPFM) surface potential measurements exhibited surface potentials of -1.5 V , $+0.8\text{ V}$, and -2.7 V for non-polarized, negatively and positively polarized ones, respectively (Figure 3.2c). This result supports that the triboelectric polarity of P(VDF-TrFE) could be tuned by the electrical polarization, which is shown in the schematic illustration of triboelectric series

(Figure 3.2d). In addition, for the aligned dipoles in a polarized P(VDF-TrFE) film, it is assumed that the surface charges are opposite to each other for the two sides of the film since dipoles are perpendicularly aligned to the film after the electrical poling,¹¹³⁻¹¹⁷ but there has been no direct experimental evidence. The triboelectric performances for the opposite-charged sides of polarized P(VDF-TrFE) films were investigated in Figure 3.6, indicating the surface charges are opposite to each other for the two sides of the polarized P(VDF-TrFE) film.

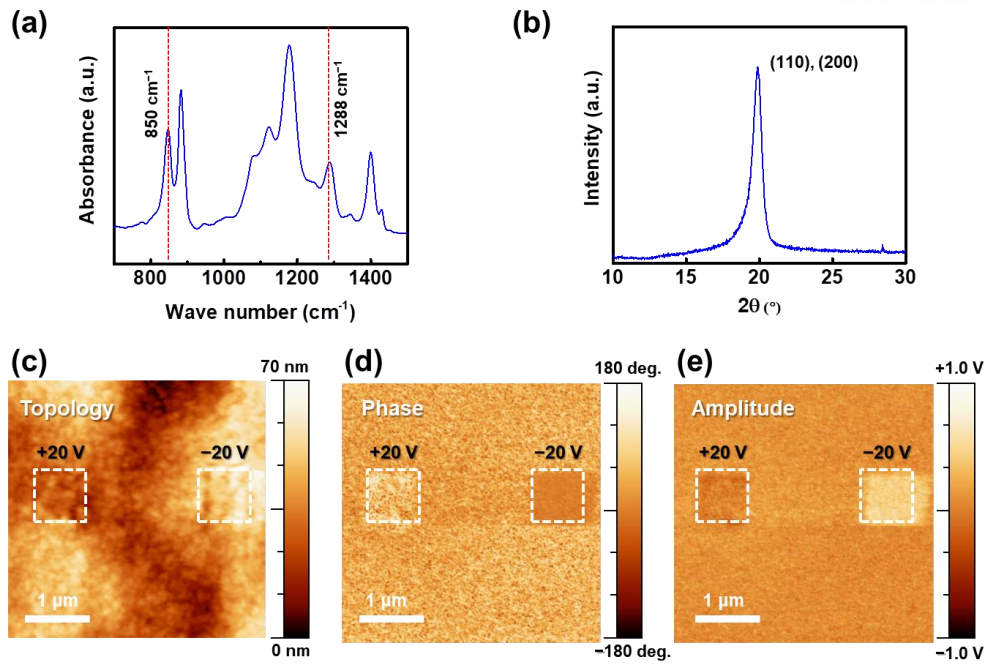


Figure 3.1. Structural and PFM analysis of P(VDF-TrFE) film. (a) FT-IR result for the β phase of P(VDF-TrFE) (b) XRD result for the β phase (110/200) of P(VDF-TrFE). (c-e) PFM images of P(VDF-TrFE) film with different direction of bias. (c) Topology, (d) phase, and (e) amplitude images of P(VDF-TrFE) films; the white dotted square indicates positively (negatively) poled area by applying +20 V (-20 V).

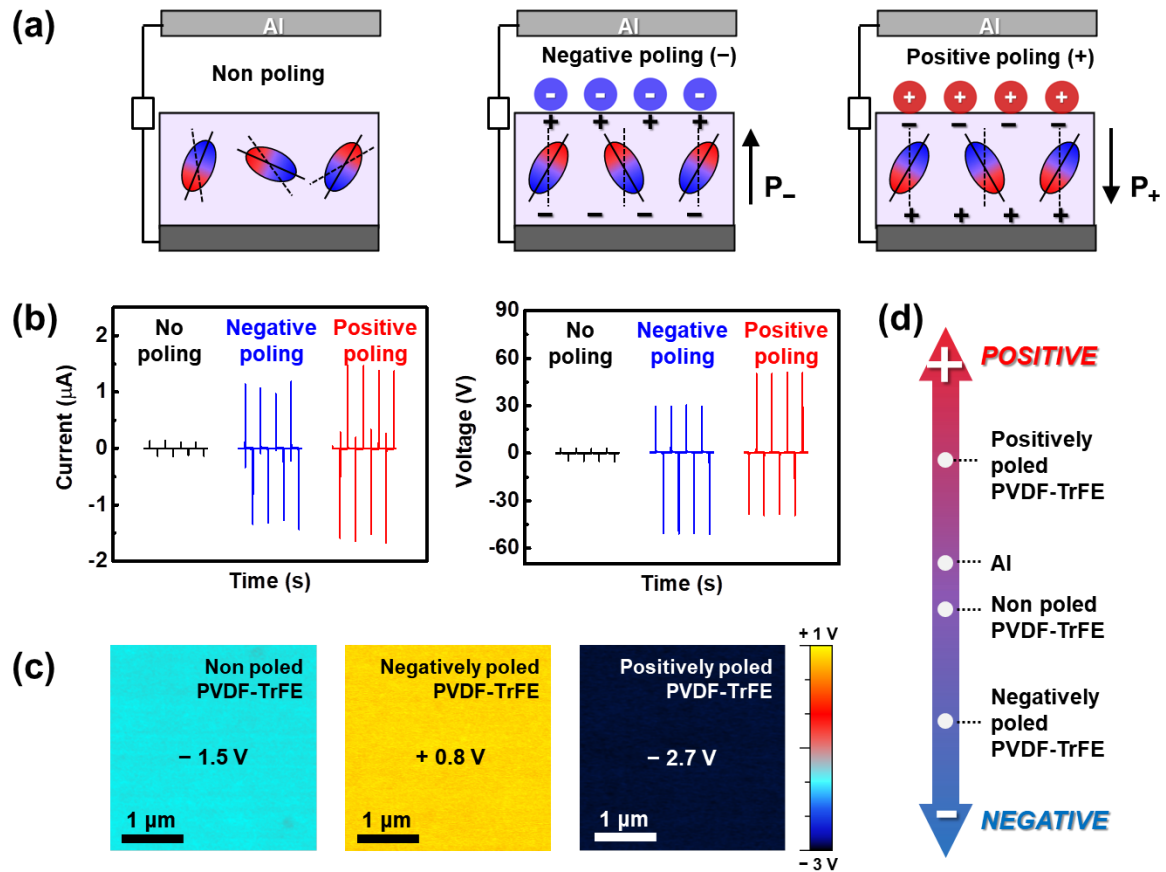


Figure 3.2. Switchable triboelectric polarity of identical P(VDF-TrFE) film by electrical polarization. (a) Schematic illustration of P(VDF-TrFE) films with different surface charge depending on the direction of dipoles. (b) Output current and voltage of surface charge-tuned P(VDF-TrFE) films. (c) KPFM images of the different surface charge potential distribution of non-, negatively and positively poled P(VDF-TrFE). (d) Modified triboelectric series with surface-charge-tuned P(VDF-TrFE) by ferroelectric polarization.

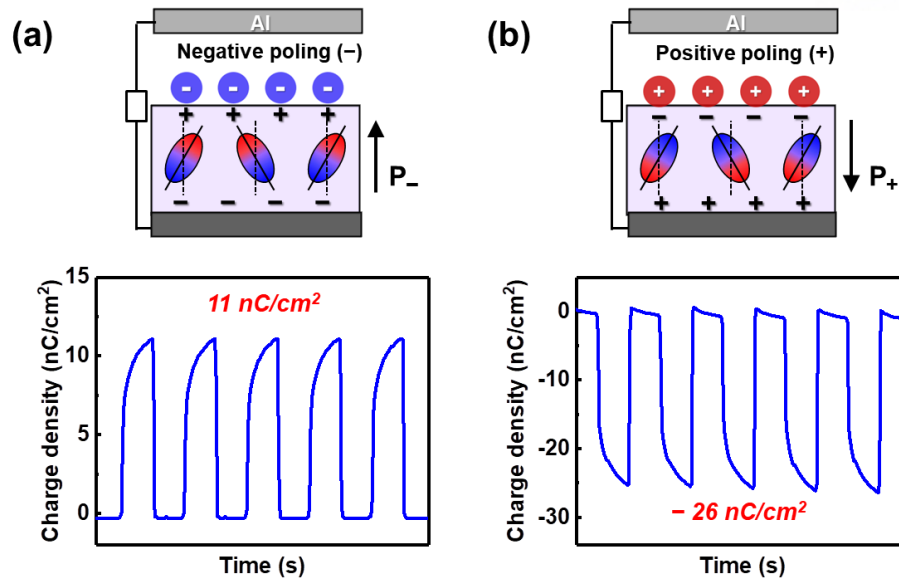


Figure 3.3. Triboelectric charge density of the polarization-tuned PVDF-TrFE films; (a) negatively, (b) positively polarized films.

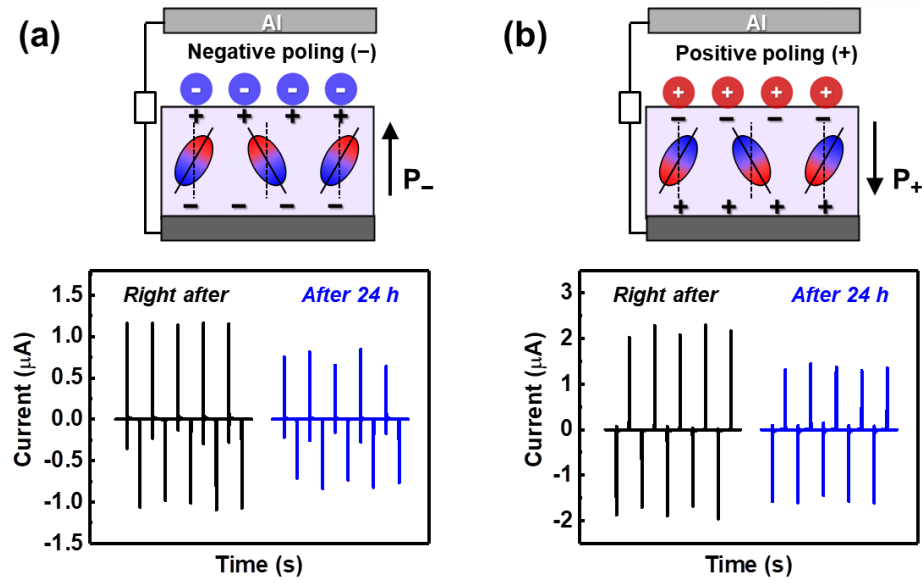


Figure 3.4. Evaluation for the duration of the tuned triboelectric performances. Triboelectric output current right after and 24 h after electrical poling from (a) negatively polarized and (b) positively polarized PVDF-TrFE films.

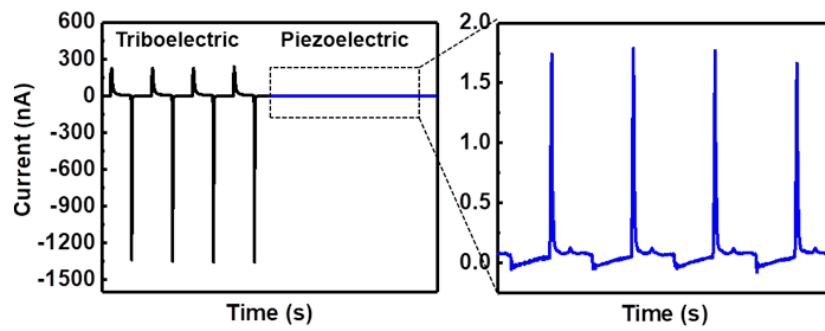


Figure 3.5. Comparison of triboelectric and piezoelectric output performances under the same pressure with 98 kPa.

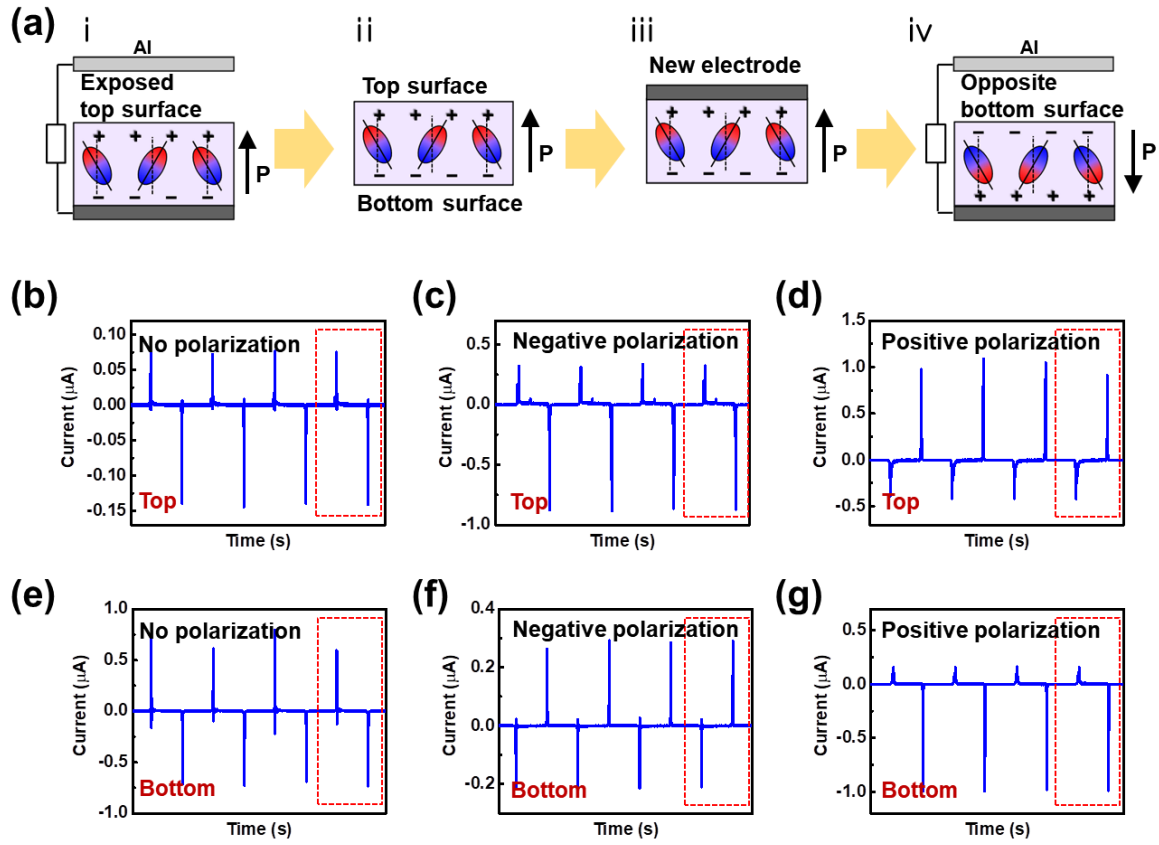


Figure 3.6. Identification of charges from both surfaces of P(VDF-TrFE) film with different polarization conditions. (a) Schematic procedure illustration of measurement of opposite bottom surface of P(VDF-TrFE) film. Output current of top surface of (b) non poled, (c) negatively poled, and (d) positively poled P(VDF-TrFE) films. Output current of bottom surface of (e) non poled, (f) negatively poled, and (g) positively poled P(VDF-TrFE) films.

Triboelectric and pyroelectric performances of polarization-tuned P(VDF-TrFE) film

Figures 3.7a-e show the working mechanism and performances of triboelectric devices based on polarization-manipulated P(VDF-TrFE) films. The triboelectric device is based on the conduction of contact electrification and electrostatic induction during the repeated contact and separation cycles (Figure 3.7a). Once the two films with opposite polarization directions come in contact with each other, triboelectric surface charges are generated at the interface of the two films, resulting in positive and negative charged surfaces at positively and negatively polarized films, respectively. During the separation of the two films, compensating charges are built up on each side of the electrodes, generating an electron flow through the external circuit until the equilibrium state is reached by the accumulated charges. When the two films approach each other again, electrons flow inversely for the charge balance. Therefore, continuous alternating triboelectric current and voltage signals appear in response to the repeated contact-separation movements between two films as shown in Figures. 3.7b and c. Figures 3.7d and 3.8a show the real-time pressure sensing of triboelectric sensors with inversely polarized P(VDF-TrFE) films under a broad range of pressures from 98 Pa to 98 kPa (sensor area of $10 \times 10 \text{ mm}^2$). Triboelectric output signals increase with the increase in pressure and are distinguishable with each other even under subtle pressure range (inset in Figure 3.7d). Triboelectric sensors exhibit three different sensitivities of 40, 11.5, and 3.7 nA kPa^{-1} in the low-pressure ($< 19.6 \text{ kPa}$), middle-pressure ($19.6\text{--}58.8 \text{ kPa}$), and high-pressure regions ($58.8\text{--}98 \text{ kPa}$), respectively (Figure 3.7e). In terms of the triboelectric voltage unit, the sensitivities are 1.4, 0.4, and 0.1 V kPa^{-1} in the low-, middle- and high-pressure regions, respectively (Figure 3.8b). In particular, the sensitivity (40 nA kPa^{-1} , 1.4 V kPa^{-1}) in the low pressure range ($< 19.6 \text{ kPa}$) is the highest compared to those sensitivities of previous PVDF-based triboelectric sensors with similar range of pressure detection and competitive with those sensitivities of other polymer-based triboelectric sensors (Table 3.1). Figure 3.8c shows the output current density and voltage as a function of load resistance. The current density decreases and the voltage increases as the load resistance increases, and the maximum power density ($147 \text{ }\mu\text{W}/\text{cm}^2$) was obtained for the $100 \text{ M}\Omega$ load resistance. This self-powered triboelectric device is sufficient to light up a green LED using a rectifying system (Figure 3.8d). The power density from our sensor is the highest compared to those of previous self-powered triboelectric pressure sensors (Table 3.1). In addition, the sensitivity and output performances of our sensors are competitive with those from identical materials with additional chemical functionalization.^{68, 70, 117}

The polarized P(VDF-TrFE) films also exhibit pyroelectricity due to the spontaneous polarization change by different dipole oscillation depending on the applied temperature (Figure 3.9a). When the device is in heating state ($\Delta T > 0$), the electric dipoles in P(VDF-TrFE) oscillate within a larger degree from their aligned axes compared to one in the ambient state ($\Delta T = 0$), resulting in a lower

level of spontaneous polarization. Consequently, the quantity of induced charges in the electrodes is reduced, leading to an electron flow from the bottom electrode to the top electrode. Meanwhile, when the device is in the cooling state ($\Delta T < 0$), the electric dipoles in P(VDF-TrFE) oscillate within a smaller degree from their aligned axes, resulting in a higher level of spontaneous polarization. Consequently, the quantity of induced charges in the electrodes is increased, leading to an inverse electron flow. Therefore, continuously alternating pyroelectric current signals appear in response to the repeated temperature change cycles. In addition, the output signal directions of pyroelectric signals in heating and cooling states are opposite with each other (Figures 3.9b, c). The response times of pyroelectric output signals for the applying and withdrawing thermal source are 0.16 and 0.09 s, respectively, which are noticeably fast compared to conventional pyroelectric devices.²²³⁻²²⁴ Figure 3.9d shows the real-time temperature sensing capability of pyroelectric sensors with inversely polarized P(VDF-TrFE) films for the ΔT from -20 to 20 °C (~ 177 mm²). Pyroelectric output current is highly responsive to the applied temperature change (ΔT) and increases with the increase in the absolute value of temperature change ($|\Delta T|$). Figure 3.10 shows the highly responsive pyroelectric performance of our sensor in real time when the object with gradually changing temperature was repeatedly contacted and separated from the sensor. The dotted graphs of gradually decreasing temperature of the hot object (Figure 3.10a) and increasing temperature of the cold object (Figure 3.10b) are highly coincident with the gradually changing graphs of corresponding pyroelectric signals, respectively. Moreover, pyroelectric output signals appear even in non-contact mode, which depends on the distance between the sensor and thermal source (Figure 3.11). Pyroelectric output signals highly decrease in non-contact (0.5 cm) than contact mode (0 cm), and further decrease with the increased distance up to 2 cm. In addition, our pyroelectric sensors exhibit high sensitivities of 0.38 and 0.27 nA °C⁻¹ in cooling and heating states, respectively (Figure 3.9e), which are competitive with those sensitivities of previous multimodal sensors (Table 3.2). We notice that the pyroelectric sensitivity and response time are different in heating and cooling states, which can be attributed to the temperature dependent atomic and molecular motions of polymer chains at different temperatures during heating and cooling processes.²²⁵⁻²²⁷ To verify the signals induced by pyroelectric effects of polarization-tuned P(VDF-TrFE) films, pyroelectric output signals were compared for different combinations of devices (Figure 3.12). Compared to the standard sensor composed of positively and negatively polarized P(VDF-TrFE) films as a bottom and top components, respectively (Figure 3.12a-c), the device with both non-polarized films shows negligible output signals (Figure 3.12d-f). When the connection of electrode polarity is switched (Figure 3.12g-i) or when the device has an opposite composition with negatively and positively polarized P(VDF-TrFE) films as a bottom and top components, respectively (Figure 3.12j-l), opposite directional output signals were observed

compared to ones from the standard devices. Therefore, the possible artifacts from the measurement system can be ruled out.

To further investigate the inversely polarized P(VDF-TrFE) films, the triboelectric and pyroelectric output performances were compared from the devices composed of different combination of non-polarized (0), positively (+) and negatively (−) polarized P(VDF-TrFE) films (Figure 3.13a). Figures 3.13b-c and 3.14a-b show triboelectric output current and voltage depending on the device combinations, respectively. Compared to the negligible outputs (~ 22 nA, ~ 0.9 V) for the device with both non-polarized films (0/0), the device with inversely polarized films (−/+) exhibits ~ 106 and ~ 126 times higher output current (~ 2.4 μ A) and voltage (~ 111 V), respectively. This result can also be confirmed by the analysis of surface potential change before and after the contact of different combinations of P(VDF-TrFE) films (Figure 3.15). There were negligible ($\Delta V = -0.07$ V) or small ($\Delta V = +0.92$ V) surface potential changes for the contact between non-polarized films (Figure 3.15a) and negatively polarized films (Figure 3.15b), respectively. On the other hand, the contact between oppositely polarized films induced noticeably large change of surface potential ($\Delta V = +9.4$ V) (Figure 3.15c). Pyroelectric output performances also show similar trends depending on the device combinations (Figures 3.13d, e and Figure 3.16). The device with inversely polarized films (−/+) exhibits noticeably enhanced output current and pyroelectric coefficient (4.7 nA, 66.9 pC/cm²K), which are ~ 12 and ~ 2230 times higher than those (0.4 nA, 0.03 pC/cm²K) for the device with both non-polarized films (0/0).

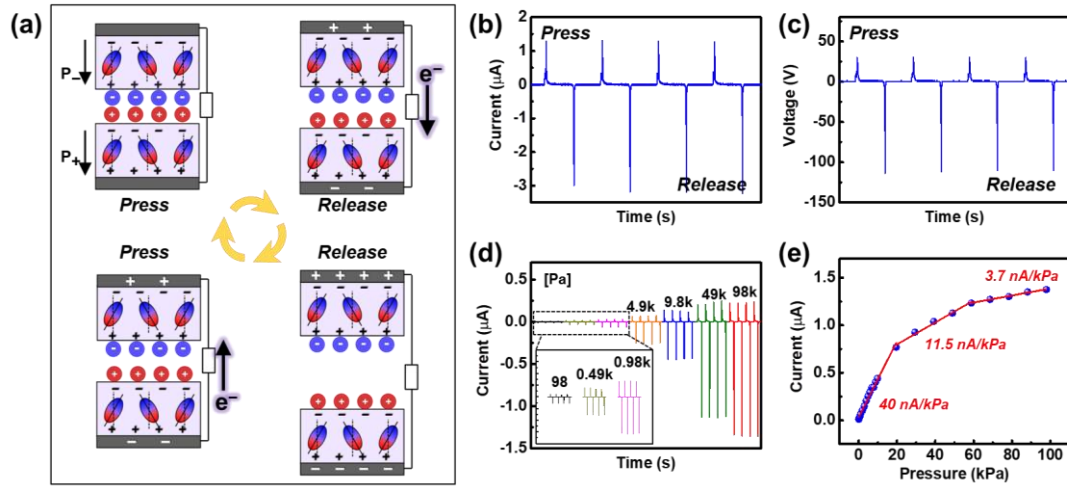


Figure 3.7. Triboelectric working mechanism and output performances of the inversely polarized P(VDF-TrFE) based sensor. (a) Schematic illustration of triboelectric charge generation and electron flow mechanism between the inversely polarized P(VDF-TrFE) films. Triboelectric output (b) current and (c) voltage under 98 kPa. (d) Triboelectric output current as a function of time under different applied pressures. (e) Linear fitting between the triboelectric current variations and the applied pressure (98 Pa to 98 kPa).

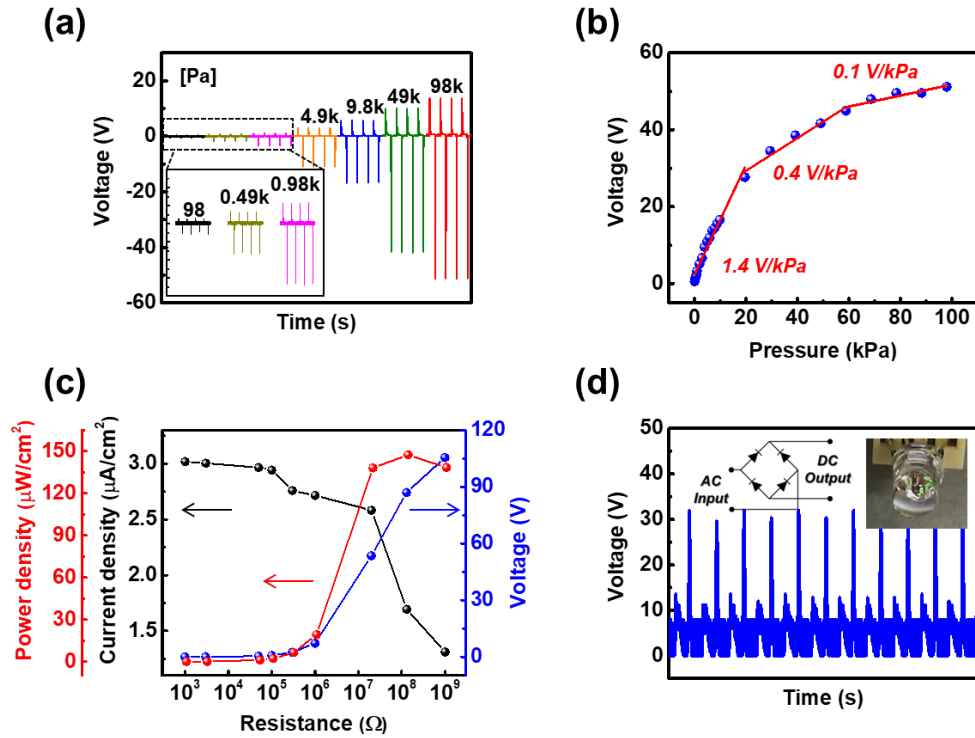


Figure 3.8. Evaluation of surface charge tuned P(VDF-TrFE) based triboelectric sensor for self-powered force sensing and output power performances. (a) Triboelectric output voltage as a function of time under different applied pressures. (b) Linear fitting between the triboelectric voltage variations and the applied pressure (98 Pa to 98 kPa). (c) Triboelectric output variations of current density, voltage, and power density with an external load resistance from 103Ω to 109Ω . (d) Rectified triboelectric voltage connected with rectifier and the inset image of capability for lighting LED driven by self-powered triboelectric sensor.

Table 3.1. Comparison of triboelectric sensitivity and output performances of the results achieved in this work with previously reported self-powered sensors.

Ref.	Major materials	Pressure range	Sensitivity	Output
<i>PVDF-based</i>				
This work	PVDF-TrFE with inverse polarization	98 Pa ~ 98 kPa	40 nA, 1.4 V/kPa (0.4 μ A/N, 14 V/N) ; 98 Pa ~ 19.6 kPa	105 V 3 μ A/cm ² 147 μ W/cm ²
201	PVDF-TrFE sponge & PDMS	50 Pa ~ 600 kPa	0.104 V/kPa ; 0.05 ~ 5 kPa	47.25 μ W/cm ²
228	Core-shell fiber ; PVDF-HFP (shell) ; PDMS-ion gel (core)	100 kPa~700 kPa	0.068 V/kPa ; 100 ~700 kPa	90 μ W/cm ²
229	PVP & PVDF fiber by electrospinning	200 Pa ~ 1.4 kPa	0.94 nA, 8.8 V/kPa ; 200 ~ 800 Pa	13.2 V 1.4 μ A ~1.15 μ W/cm ²
75	Porous PVDF/ porous PDMS	< 100 kPa	0.55 V/kPa ; Below 19.8 kPa	~46.7 μ W/cm ²
151	PVDF stitches & Nylon	326 Pa ~ 326 kPa	0.66 nA, 6.23 mV/kPa ; 326 Pa ~ 16.3 kPa	-
<i>Other polymer-based</i>				
206	Liquid & PDMS	< 40N	0.035 nA/N	3.15 V 2.5 nA 7.8 nW/cm ²
230	CNT & PDMS	-	1 V/N	60 V 180 nA 1.7 μ A/cm ²
231	ITO & PDMS	0.3 ~ 429 kPa	2.82 mV/kPa	1.6 V 47.3 μ A/cm ² 0.13 μ W/cm ²
196	Cu on PDMS & PTFE	< 40N	0.04 μ A/N, 0.5 V/N	25 V 1.3 μ A 2.45 μ W/cm ²
207	Al & PDMS	40 ~ 140 N	28 mV/N	90 V 9 μ A
205	PDMS (single mode)	0.6 Pa ~ 30 MPa	6 MPa ⁻¹ ; 0.6 Pa ~ 200 kPa	-
72	PET & PDMS	13 mPa <	-	18 V ~0.13 μ A/cm ² ~2.34 μ W/cm ²
232	FEP (single mode)	1 ~ 250 kPa	2.79 V/kPa ; < ~10 kPa	-

233	FEP & foreign object	< 10kPa	44 V/kPa ; Below 150 Pa	50 V (10 kPa)
197	PDMS & Al	1 kPa ~ 80 kPa	0.06 kPa ⁻¹	-
234	PDMS & glass	63 Pa < 25kPa	0.29 kPa ⁻¹ (9.54 V/kPa) ; 63 Pa ~ 5 kPa	~30 V (4.5 kPa)
131	PTFE & Nylon	2.5 Pa ~ 6 kPa	51 V/kPa ; 2.5 Pa ~ 1.2 kPa;	~37 V (0.8 kPa)
235	FEP & PDMS	< 180 Pa	150 V/kPa	~70V (1 kPa)

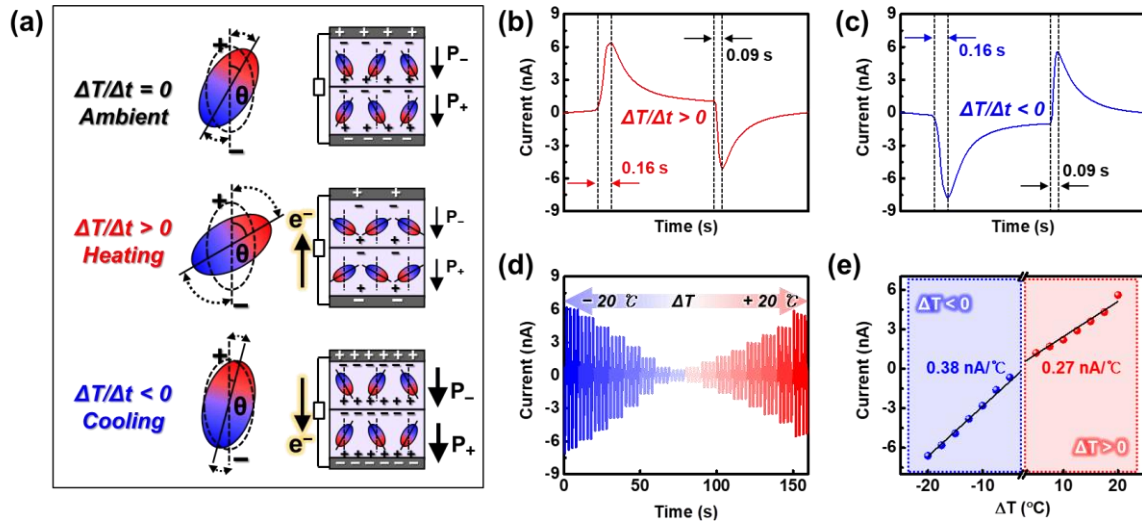


Figure 3.9. Pyroelectric working mechanism and performances of the inversely polarized P(VDF-TrFE) based sensor. (a) Schematic illustration of pyroelectric charge generation and electron flow mechanism between the inversely polarized P(VDF-TrFE) films. Pyroelectric output currents from (b) heating and (c) cooling states. (d) Pyroelectric output current as a function of time under different applied temperatures (ΔT) from -20 to 20 °C. (e) Linear fitting between the pyroelectric current variations and the applied temperatures.

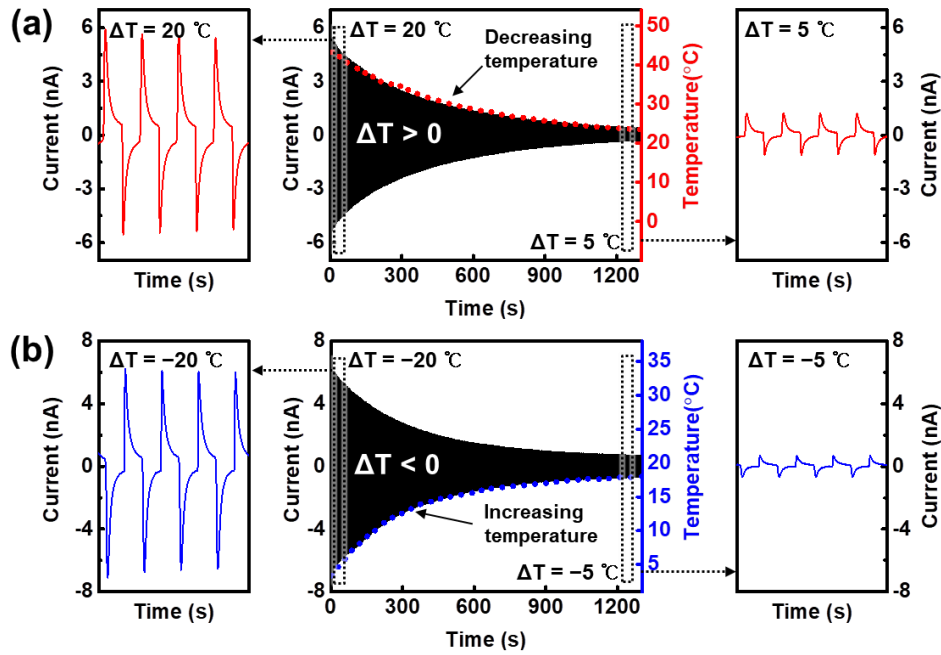


Figure 3.10. Highly responsive pyroelectric performance under real-time temperature gradient. (a, b) Pyroelectric output current as a function of time under gradually (a) decreased temperature ($5^\circ\text{C} < \Delta T < 20^\circ\text{C}$) and (b) increased temperature ($-20^\circ\text{C} < \Delta T < -5^\circ\text{C}$).

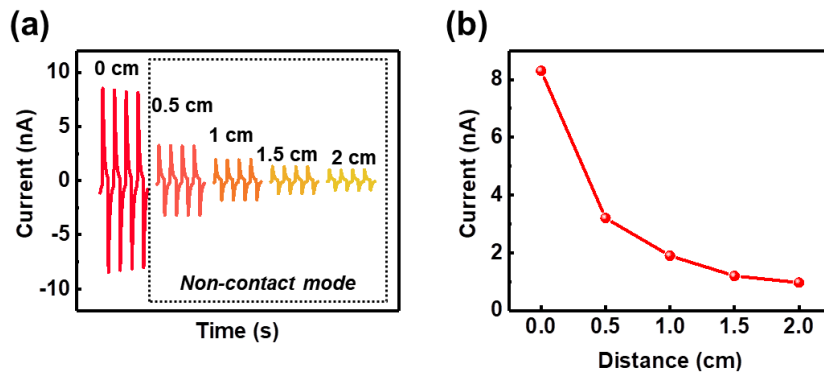


Figure 3.11. Evaluation of the pyroelectric performances of the inversely polarized P(VDF-TrFE)-based sensors with different distances between the sensor and thermal source. (a) Pyroelectric output current as a function of time under different distances. (b) Comparison of pyroelectric performances from different distances.

Table 3.2. Comparison of multimodal sensing performances of the results achieved in this work with previously reported multimodal sensors.

Ref.	Type	Major materials	Performances	Structure	Simultaneous detection	Zero-bias
This work	Pyroelectric /Trieoelectric	PVDF-TrFE	$\Delta T \pm 20\text{ }^{\circ}\text{C}$ (3 ~ 43 $^{\circ}\text{C}$) 0.27 nA/ $^{\circ}\text{C}$ @ $\Delta T > 0$ 0.38 nA/ $^{\circ}\text{C}$ @ $\Delta T < 0$ Response time 0.16s	Single device	○	○
224	Trieoelectric /Piezoelectric /Pyroelectric	PVDF, Ag NWs @ PTFE	0.11 V/ $^{\circ}\text{C}$ @ 0~58 $^{\circ}\text{C}$ Response time 0.53 s	Single device	○	○
92	Piezo resistive /Piezoelectric /Pyroelectric	PDMS/MWNT composite	-2 ~ 100 $^{\circ}\text{C}$ 2.93 E ⁻² / $^{\circ}\text{C}$	Single device	○	×
11	Piezoelectric /Capacitive	CNT micro yarn, Ecoflex, PDMS	-	Single device	○	×
141	Thermo-conductive	Different R of Pt & porous PDMS	20 ~ 80 $^{\circ}\text{C}$	Integrated device	○	×
144	Piezo-resistive / NTC of rGO	Graphene Nanoplatelet, PDMS	25 ~ 100 $^{\circ}\text{C}$ 4.8 E ⁻⁴ / $^{\circ}\text{C}$	Single device	$\Delta^{\text{a)}$	×
143	Resistive /Capacitive	CVD-Graphene, GO, rGO, PDMS	0 ~ 95 $^{\circ}\text{C}$	Integrated device	×	×
236	Thermoelectric	rGO porous foam	$\Delta T < 97\text{ }^{\circ}\text{C}$	Single device	×	○
111	Pyroelectric /Piezoelectric /Trieoelectric	PVDF-TrFE with different solvent	ΔT 13 $^{\circ}\text{C}$ (23 ~ 36 $^{\circ}\text{C}$) 315.8 mV & 36.29 nA	Not single device	×	○
223	Pyroelectric /Piezoelectric	Methylammonium lead iodide incorporated electro-spun PVDF nanofibers	ΔT 38 $^{\circ}\text{C}$ (298 ~ 336 K) 15.7 pA Response time ~ 1.14 s	Single device	×	○
140	Pyroelectric /Piezoelectric /Trieoelectric	Al/PTFE/Cu Cu/PVDF/Cu	ΔT 10 $^{\circ}\text{C}$ (25 ~ 35 $^{\circ}\text{C}$)	Integrated device	$\Delta^{\text{b)}$	○
142	Pyroelectric /Piezoelectric /Trieoelectric & Electromagnetic shielding	PVDF & Rubber-coated antimagnetic radiation fabric	ΔT 27 $^{\circ}\text{C}$ (23 ~ 50 $^{\circ}\text{C}$) ΔT of finger touch; ~2 $^{\circ}\text{C}$	Integrated device	$\Delta^{\text{b)}$	○
145	Pyroelectric /Piezoelectric	BTO/PDMS	ΔT 2.03 ~ 13.57 $^{\circ}\text{C}$ (27 ~ 40 $^{\circ}\text{C}$) 0.96 nA/ $^{\circ}\text{C}$ ΔT -1.8 ~ -7 $^{\circ}\text{C}$ (19~27 $^{\circ}\text{C}$) 1.33 nA/ $^{\circ}\text{C}$	Single device	$\Delta^{\text{c)}$	○

a) Simultaneous detection is possible, but output signals are overlapped because of same directional signal. So, peak deconvolution is necessary.

b) Output signal is simultaneously responsive to applied stimuli, but it's hard to distinguish each stimulus.

c) Simultaneous detection is possible, but each stimulus was applied with different frequency.

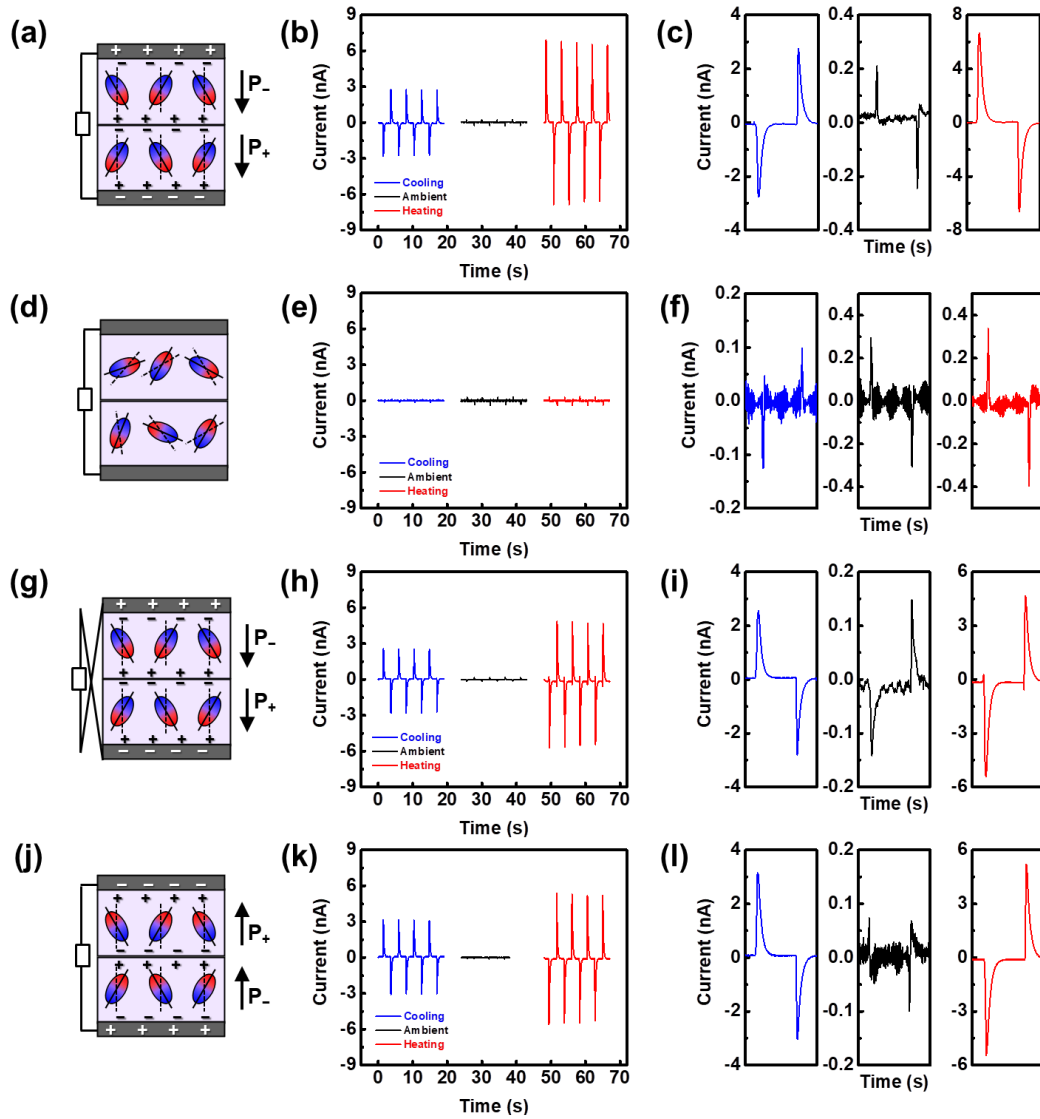


Figure 3.12. Pyroelectric output performances depending on the device compositions. Pyroelectric output signals under different temperature from (a-c) standard device composed of positively and negatively polarized P(VDF-TrFE) films as a bottom and top components, respectively, and (d-f) device with non-polarized films. Opposite directional pyroelectric signals from (g-i) reverse connection and (j-l) opposite composition of device compared to ones from standard device in forward connection.

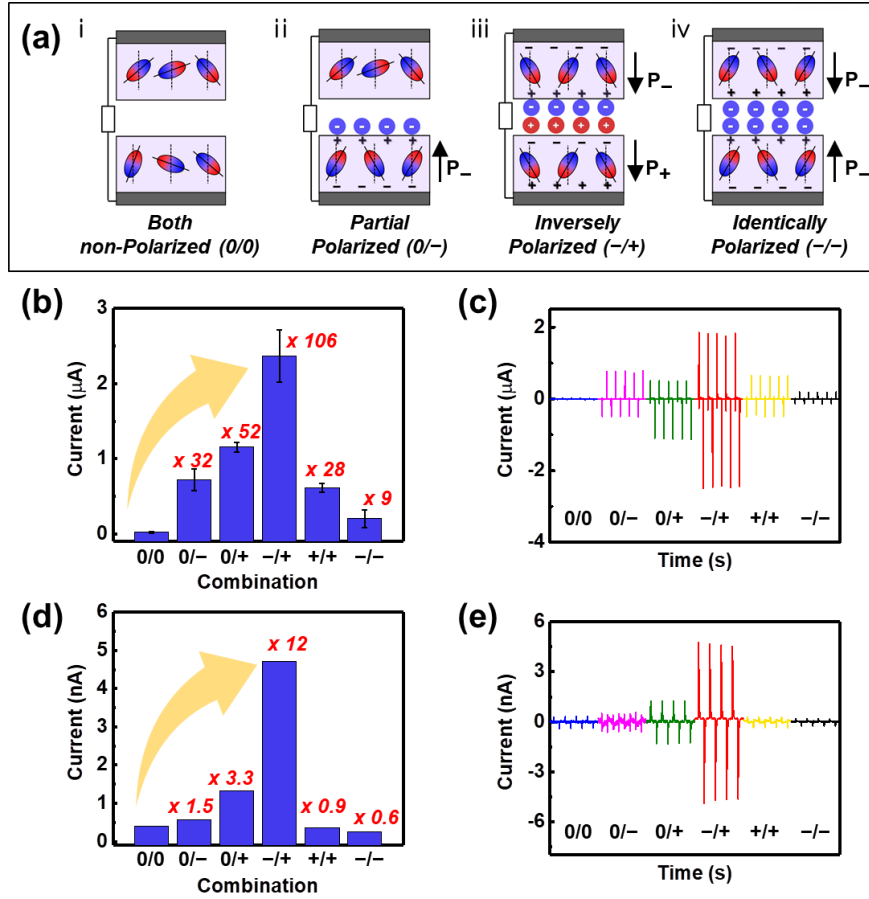


Figure 3.13. Comparison of triboelectric and pyroelectric performances from different compositions of P(VDF-TrFE) based sensors. (a) Schematic illustration of diverse devices composed with two P(VDF-TrFE) films; non poled, negatively poled, and positively poled P(VDF-TrFE) films. Output currents of different composition of (b) triboelectric and (d) pyroelectric devices based on surface charge-tuned P(VDF-TrFE) films. (c) Triboelectric and (e) pyroelectric output currents as a function of time with different composition of devices.

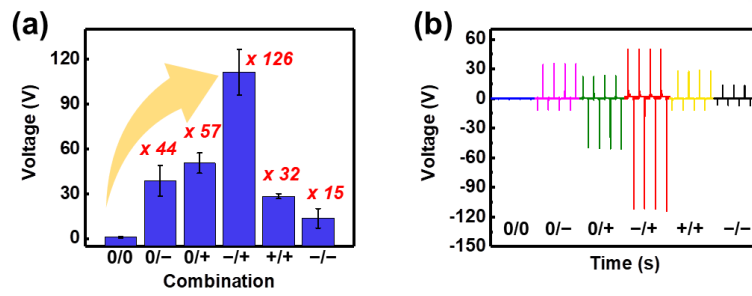


Figure 3.14. Comparison of triboelectric performances from different compositions of P(VDF-TrFE) based sensors. (a) Output voltages of different composition of triboelectric devices based on surface charge-tuned P(VDF-TrFE) films. (b) Triboelectric output voltages as a function of time with different composition of devices.

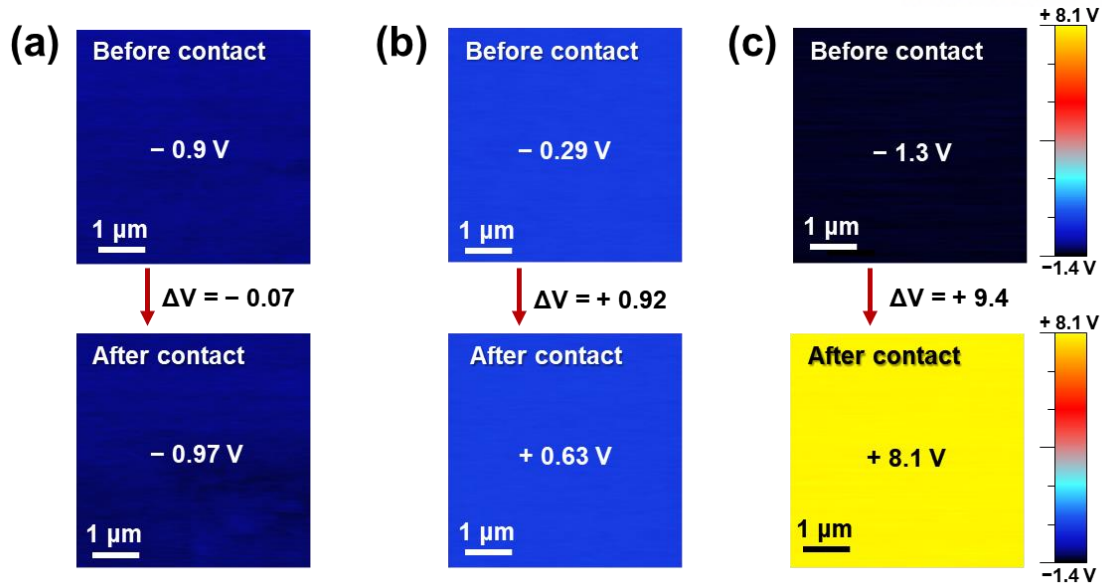


Figure 3.15. KPFM of various combinations before and after contact-separation with different compositions of P(VDF-TrFE) films; (a) both non polarized films, (b) both negatively polarized films and (c) oppositely polarized films (negatively and positively poled films).

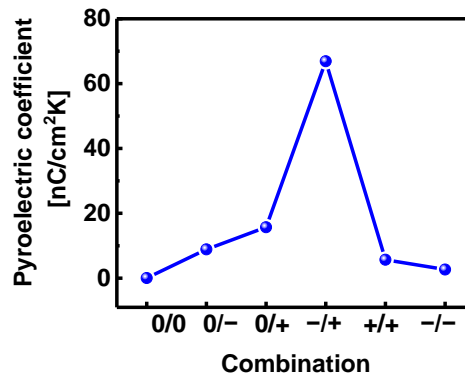


Figure 3.16. Pyroelectric coefficient with different combinations of sensors.

Multimodal sensing performances of polarization-tuned P(VDF-TrFE) based devices under simultaneously applied pressure and temperature

Our device with the simultaneous triboelectric and pyroelectric effects exhibits multimodal performances (Figure 3.17). The pressure detection is based on the conduction of contact electrification and electrostatic induction during the repeated contact and separation of inversely polarized two P(VDF-TrFE) films. Meanwhile, the temperature detection is based on the spontaneous polarization change by different dipole oscillation during the repeated contact and separation between the sensor and temperature-controlled external object. When the pressure is applied simultaneously with the higher temperature than the room temperature (RT), the same direction of electron flow arises from the bottom to the top electrodes (Figure 3.17a-i), followed by both sharp triboelectric and gradual pyroelectric signals in the same direction (Figure 3.17b). Meanwhile, when a lower temperature than RT is applied simultaneously with the pressure on the sensor, the opposite directions of electron flows arise from triboelectric and pyroelectric effects; triboelectric electron flow is induced from the bottom to the top electrodes while pyroelectric electron flow is induced from the top to the bottom electrodes (Figure 3.17a-ii). Consequently, decoupled bimodal signals are shown with sharp triboelectric and gradual pyroelectric signals (Figure 3.17c). Due to the different response time of triboelectric and pyroelectric effects, both signals show different saturation time. The gradual pyroelectric signals are cut by the followed next spike triboelectric signals because pyroelectric signals have a longer saturation time than the triboelectric signal under the repeated contact-separation cycle with 0.5 Hz. Herein, P_c (point in the contact) and P_s (point in the separation) in Figures 3.17b and c are cut points by the followed signals from applying and releasing the stimuli, respectively.

Our sensor can be utilized to differentiate the simultaneously applied pressure and temperature by the decoupled signals under the negative temperature change ($\Delta T < 0$) due to the opposite electron flow from triboelectric and pyroelectric effects (Figure 3.18a). Figures 3.18b and c show the pressure dependent output signal when ΔT is -20°C . The triboelectric spike signals increase with the increased pressure, while the opposite directional pyroelectric signal is constant under the same temperature. Figures 3.18d and e show the temperature dependent output signal under 490 Pa. The pyroelectric signals decrease with the decreased absolute value of temperature change ($|\Delta T|$). Here, the gap distance between P_c and P_s (Figures 3.17 b and c) can be used to distinguish the applied temperature from the simultaneously applied pressure regardless of the sign of ΔT . Figures 3.19 a-c and d-f show pressure-dependent output signals under heating and cooling conditions, respectively. The spike signals increase as the applied pressure is increased, while the gap distance between P_c and P_s is constant under the same temperature change even with a different pressure. Figures 3.20 a-d and e-h show heating and cooling temperature-dependent output signals under different pressure. The

spike signals change depending on the pressure while the gap distances between P_c and P_s depend on the temperature change. Therefore, the simultaneously applied temperature and pressure can also be discriminated by the gap distance between P_c and P_s , and the height of spike signals, respectively. The ability of our sensor to differentiate the simultaneously applied stimuli without external bias is advantageous for sustainable wearable devices compared to previous multimodal devices (Table 3.2).

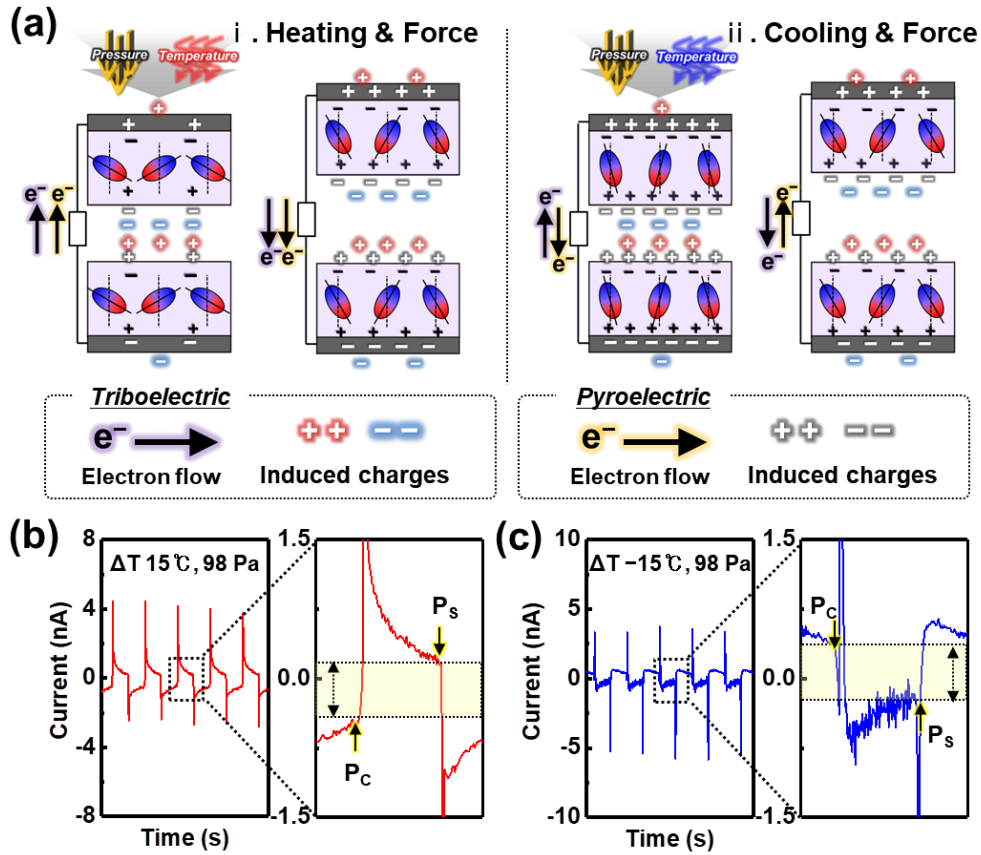


Figure 3.17. Working mechanism of multimodal sensing performance of inversely polarized P(VDF-TrFE) based sensors. (a) Schematic illustration of both triboelectric and pyroelectric charge generation and electron flow mechanism between the inversely polarized P(VDF-TrFE) films. Multimodal output currents and enlarged peaks from (b) heating and (c) cooling states under 98 Pa; the gradual pyroelectric signals are cut by the followed next spike triboelectric signals.

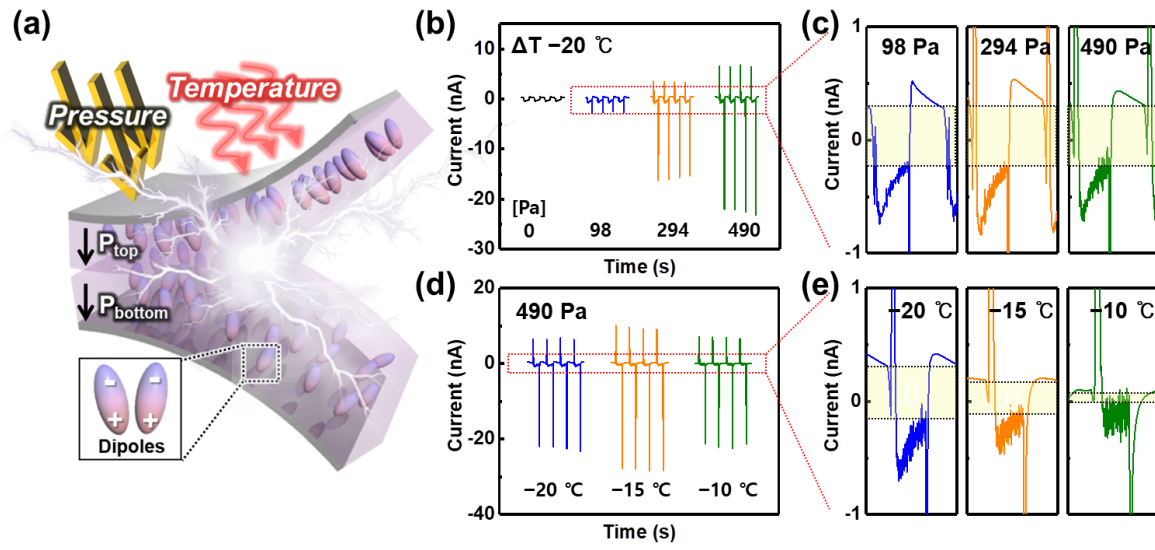


Figure 3.18. Decoupled signals of multimodal sensor under simultaneously applied pressure and temperature. (a) Schematic illustration of multimodal sensing of inversely polarized P(VDF-TrFE) based sensor. (b-e) Multimodal output currents as a function of time and enlarged each peak to respond the simultaneous stimuli; the output currents depending on (b, c) the pressure under -20°C (ΔT) and (d, e) the temperature under 490 Pa.

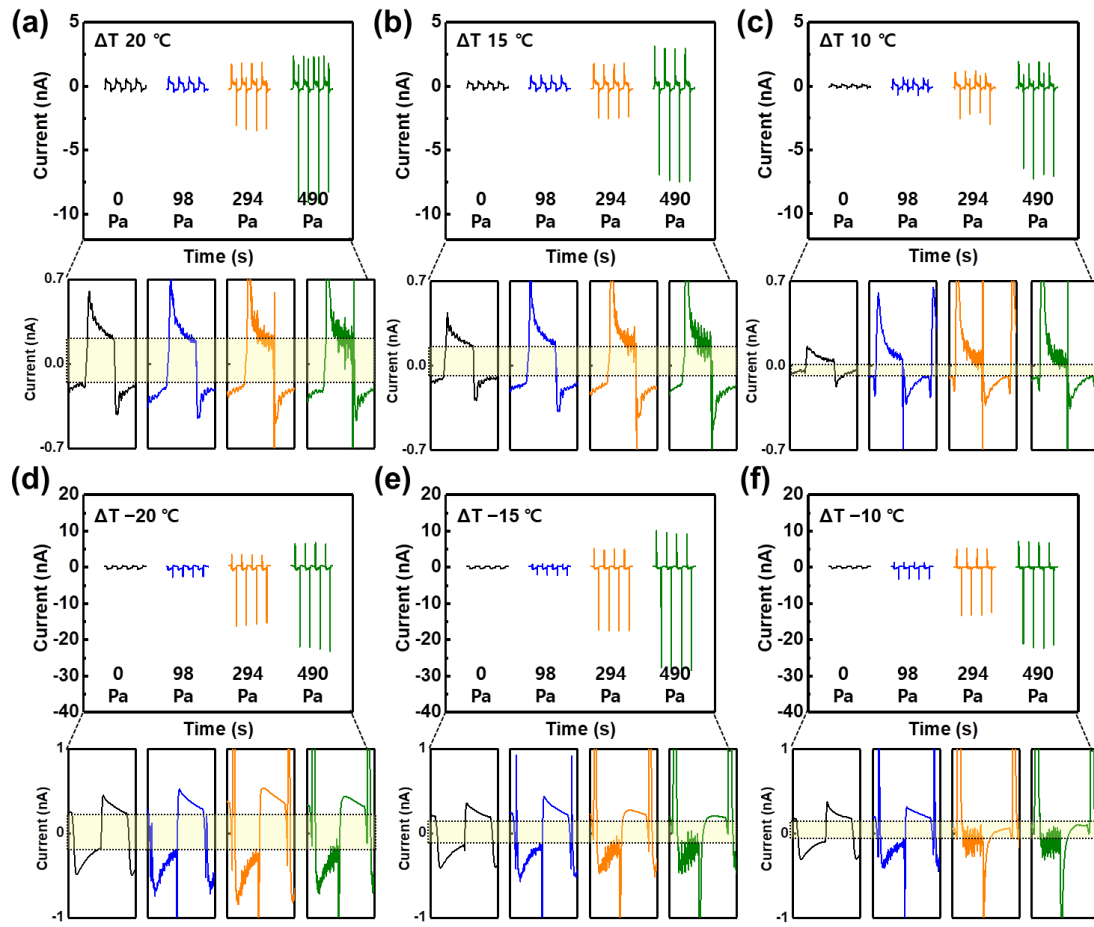


Figure 3.19. Pressure-dependence of the multimodal output signals under different temperature changes; (a-c) heating and (d-f) cooling.

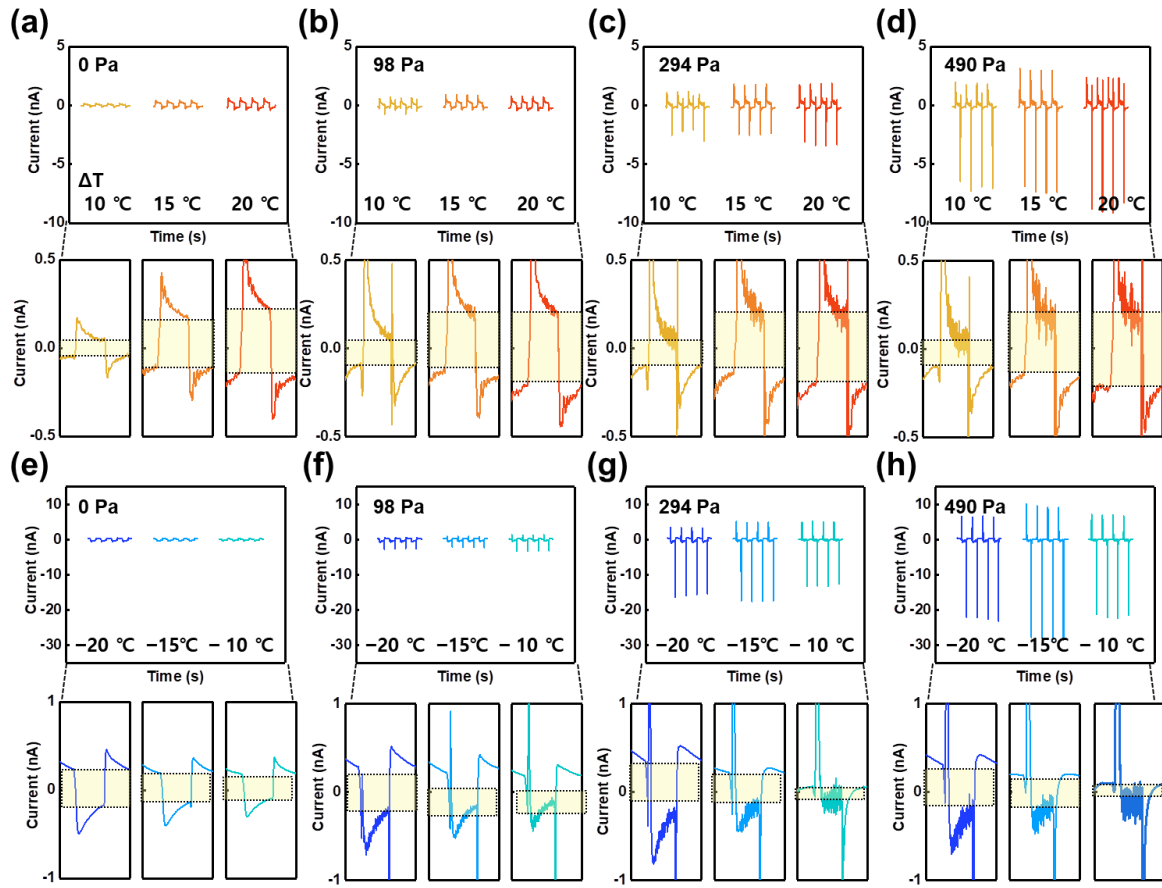


Figure 3.20. Temperature-dependence of the multimodal output signals from (a-d) heating and (e-h) cooling process under different pressures.

Healthcare and human-machine interface applications

Our triboelectric sensor is promising for applications in self-powered diagnostic sensors to monitor human health in real time. In particular, the high pressure sensitivity of our sensor in the low pressure region is advantageous in the monitoring of weak pulse pressure of carotid artery (Figure 3.21a). Figures 3.21b and c show the triboelectric output signals for the pulse pressure with three distinguishable peaks (P_1 , P_2 , and P_3). Herein, P_1 is the main pulse pressure by the blood flow ejected by the contraction of the heart, and P_2 and P_3 are the reflected wave pressures by the waves reflected from the peripheral sites.²¹³ These parameters can be used to extract the radial artery augmentation index ($AI_r = P_2/P_1$) and round-trip time of a reflected wave from the hand periphery (T_r), which are related to the arterial stiffness depending on the person's age.²⁰¹ When the devices with non-polarized PVDF-TrFE films and only electrode are used for pulse pressure detection instead of the device with inversely polarized films, the much smaller responsive output signals and negligible noise signals are observed, excluding the possible signal artifacts from the measurement system and the environmental interference (Figure 3.22). Figures 3.21d and e exhibit the artery pulse signals of a healthy female before and after physical exercise. After the physical exercise, the pulse rate increases from ~86 beats per minute (BPM) to ~97 BPM and the signal intensity also increases due to the increased cardiac output to rapidly supply blood to the activated muscles. The average value of the augmentation index ($AI_r = 0.48$) is consistent with the literature data of healthy females in their ages.²¹³⁻²¹⁴ AI_r value decreased to 0.16 after physical exercise (Figure 3.23), which indicates the decreased arterial stiffness owing to the vasodilation of the muscular arteries.²¹³⁻²¹⁴ In addition, our polarity-switchable P(VDF-TrFE) multimodal sensors can simultaneously monitor the pressure and temperature of the fingertip touch in real-time (Figures 3.21f-i). When our sensor was forced with different temperatures by warm (~29 °C) and cold (~16 °C) fingers (Figures 3.21f and h), the sensor shows temperature-dependent output signals (Figures 3.21g and i). The output signal for the cold finger is comprised of two opposite directions of peaks (I_1 , I_2), while the output signal for the warm finger is comprised of the same direction of two peaks (I_1 , I_2). Herein, the sharp current peak (I_1) is a triboelectric signal generated by the touching pressure and the gradual current peak (I_2) is the pyroelectric signal generated by the applied temperature. This result demonstrates that our triboelectric-pyroelectric hybrid sensor is promising for applications in wearable artificial intelligent systems and human-machine interfaces.

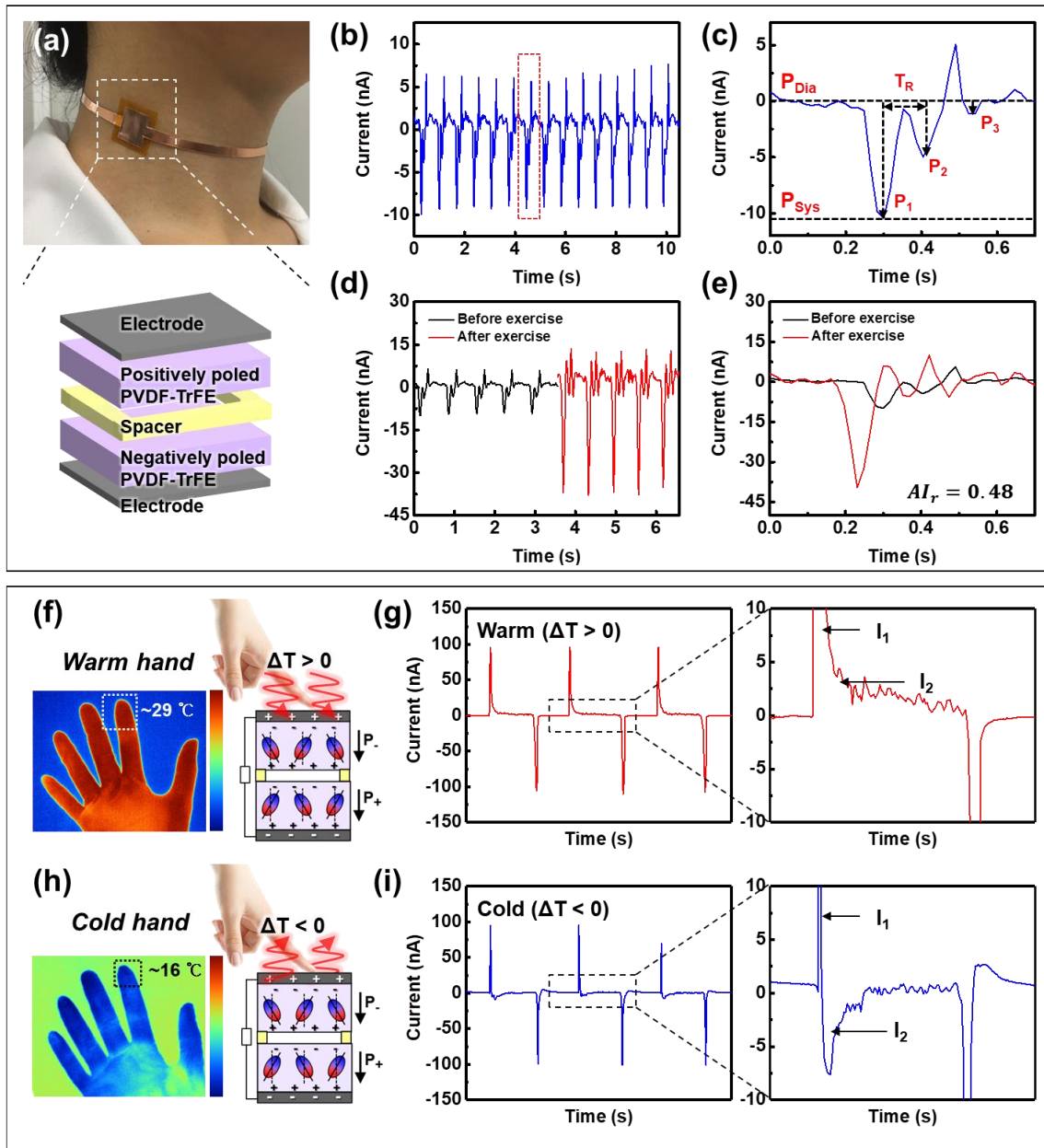


Figure 3.21. Simultaneous monitoring of weak pulse pressure from carotid artery and different temperatures of finger touch. (a) Photographic images of real-time detection of pulse pressure with the inversely polarized P(VDF-TrFE) based sensor. (b) Real-time monitoring of the pulse pressure and (c) expanded pulse wave with three peaks (P_1 , P_2 , P_3). (d, e) Variation in the pulse pressure waves before and after physical exercise. (f, h) Schematic illustrations of finger touch monitoring from warm and cold hands with each infrared image of hand. Real-time monitoring of (g) the warm and (i) cold finger touches and enlarged responsive signal consisting of two peaks from finger pressure (I_1) and temperature (I_2).

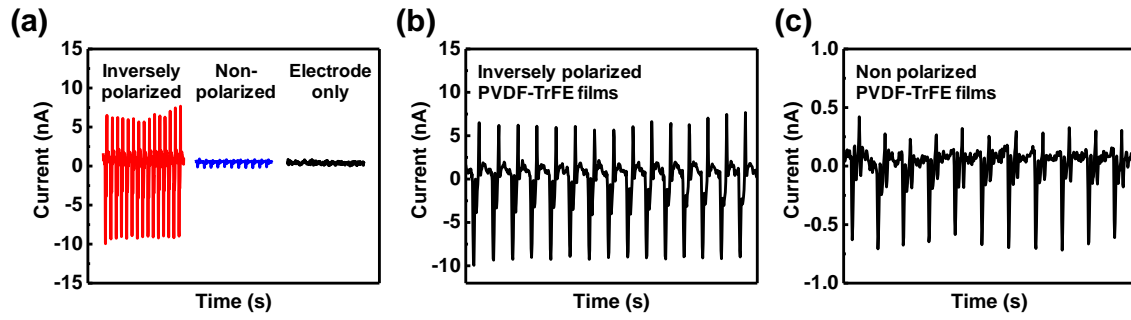


Figure 3.22. Validation of the real-time detection of pulse pressure. (a) Comparison of the pulse-pressure responsive signals from inversely polarized, non-polarized sensors and electrode only; the enlarged responsive signals from (b) inversely polarized PVDF-TrFE sensor and (c) non polarized PVDF-TrFE sensor.

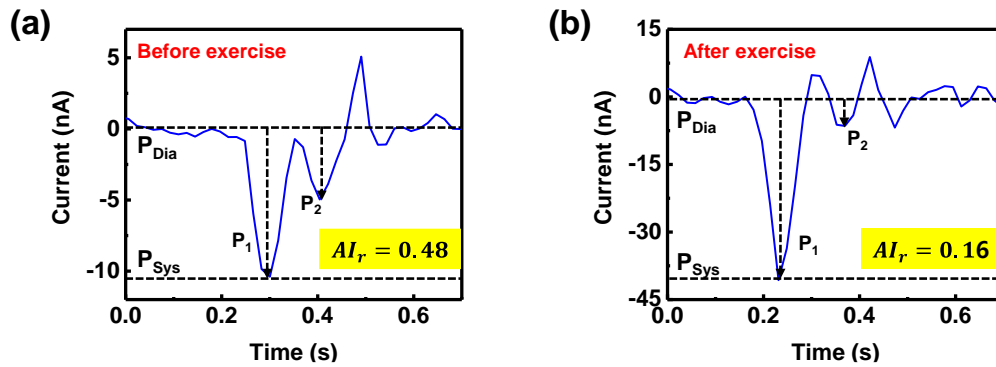


Figure 3.23. Comparison of augmentation index (AI_r) before and after physical exercise.

3.4 Conclusions

In summary, we demonstrated an efficient approach to fabricate high-performance triboelectric and pyroelectric-based multimodal sensors with the identical contact pair material via modulation of triboelectric polarity of the ferroelectric copolymer (P(VDF-TrFE)) by electrical polarization. We observed that the aligned direction of dipoles in P(VDF-TrFE) can be easily switchable depending on the applied polarization bias direction. Consequently, the device with inversely polarized films has noticeably enhanced triboelectric output performance with ~ 106 and ~ 126 times higher output current and voltage values compared to the device with non-polarized ones. Our triboelectric sensor exhibited the pressure sensitivity of 40 nA kPa^{-1} (1.4 V kPa^{-1}) and output power of $147 \text{ }\mu\text{W/cm}^2$, which are the highest values among the PVDF-based self-powered sensors. In addition, our sensor with inversely polarized films shows remarkable pyroelectric output performance with ~ 12 times higher output current value compared to the device with non-polarized ones. Our sensor displayed the high sensitivity of 0.38 and $0.27 \text{ nA } ^\circ\text{C}^{-1}$ in cooling and heating states, respectively, which are the competitive values among previous temperature sensors. The ultrahigh sensitivity of our sensor can be used for the simultaneous monitoring of weak pulse pressure of carotid artery. Moreover, our sensor can be utilized for the multimodal finger touch monitoring due to the multimodality in simultaneous sensing of pressure and temperature in real time. Our approach on the modulation of triboelectric polarity provides a feasible route to remarkably enhance the output performances of multimodal devices based on identical contact pair materials even without any additional chemical functionalization or mechanical modification on the opposite materials in a contact pair. We anticipate that our strategy can also be effective for other ferroelectric materials such as other PVDF-based copolymers such as poly(vinylidene fluoride-co-hexafluoropropylene) (PVDF-HFP), poly(vinylidene fluoride-chlorotrifluoro ethylene) (PVDF-CTFE), poly(vinylidene fluoride-trifluoroethylene-chlorotrifluoroethylene) (PVDF-TrFE-CTFE) and inorganic ferroelectric materials (BaTiO_3 , PZT, etc.). In addition, our self-powered sensor provides new approaches for the discrimination of multiple pressure and temperature without signal interference, which can find diverse applications in self-powered multimodal healthcare sensors, artificial intelligent systems and human-machine interfaces.

Chapter 4. Alternating PVDF-TrFE/BaTiO₃ multilayer nanocomposites for enhanced triboelectric performances

4.1 Introduction

Energy harvesting systems can scavenge abundant energy from solar power, thermal energy, and wind energy. Among various energy harvesting systems, triboelectric nanogenerators (TENGs) can produce electrical energy from mechanical energy via triboelectrification and electrostatic induction. In particular, the TENG generates electrical outputs that are proportional to the intensity of mechanical strength, which is beneficial for applications in triboelectric sensors (TESs).^{75, 171} TESs, possessing the merits of high power density, flexibility, low-cost, and an easy fabrication process, have been applied to self-powered pressure sensors,^{75, 168, 237-238} wearable and body-implantable electronics,^{237, 239} and healthcare monitoring devices.^{151, 240-241} As the triboelectric output performances are proportional to the surface charge density, various approaches that increase the surface area or triboelectric polarity difference between opposite triboelectric materials through surface physical or chemical modifications^{68, 242-244} have been proposed to increase the surface charge density of materials. The use of materials with high dielectric constant (k) could also increase the surface charge density owing to the enhanced capacitance of the dielectric layer.^{147, 245} To further enhance the surface charge density, various attempts have been made to use ferroelectric polarization.^{62, 113, 115-116} Ferroelectric materials can improve the triboelectric output performance by enhancing the quantity of triboelectric charges on the surface through the coupling of residual dielectric polarization and surface polarization during the triboelectrification.²⁴⁶

Triboelectric devices with ferroelectric organic materials such as PVDF and PVDF-TrFE have the advantage of high flexibility and controllable ferroelectric polarization, which leads to high surface charge density and thereby improved triboelectric output.¹¹⁴⁻¹¹⁶ However, triboelectric devices with organic dielectrics exhibit a limited output performance owing to their relatively low dielectric constants. On the contrary, triboelectric devices containing high- k inorganic materials such as ZnO,²⁴⁷ CsPbBr₃,²⁴⁸ and TiO₂²⁴⁹ exhibit high output performances, but the brittleness of inorganic materials prevents their applications in flexible devices. To address this issue, hybrid organic/inorganic materials with the properties of both high dielectric constants and flexibility have been utilized to develop high-performance and flexible triboelectric devices.^{62, 146-147} However, triboelectric devices based on composites containing randomly distributed inorganic particles require precise control of the quantity of nanoparticles and their dispersion owing to the issue of nonuniform nanoparticle agglomeration, which results in deteriorated performances.¹⁴⁹

The stress-induced polarization of ferroelectric materials can be enhanced by controlling effective transfer of applied mechanical stress to them. Previously, stress concentration structures have been reported in various micro/nanostructures, including porous structures,²⁵⁰⁻²⁵¹ surface microstructures,⁹² and composites with mechanically reinforcing fillers.^{90, 148} For example, Park et al. reported a high-performance piezoelectric sensor based on well-dispersed BTO NPs in the PDMS polymer matrix.¹⁴⁸ The concentrated stress between the high modulus ceramic nanoparticles and low modulus polymer induced a large deformation of the BTO/PDMS composite, thus leading to a high piezoelectric potential. In addition, Gao et al. demonstrated vertically-aligned ceramic particles in a polydimethylsiloxane (PDMS) matrix.¹⁵⁰ The aligned ceramic particles in the polymer matrix exhibited a higher stress transfer capability than the randomly dispersed particles, which increased the polarization of ferroelectric nanoparticles, generating a high piezoelectric potential.

Herein, we introduce high-performance TESs based on ferroelectric multilayer composites consisting of alternating organic PVDF-TrFE and inorganic BTO NP layers. Compared to random composite TESs, the organic/inorganic multilayer structure with alternating soft/hard layers can effectively transfer the applied vertical stress to the inorganic nanoparticles, leading to significantly improved triboelectric output. Moreover, the multilayered structure provides superior interfacial polarization compared to random composites, resulting from the reduced leakage current induced by the PVDF-TrFE barrier layers between inorganic BTO NP layers. In addition, the introduction of an electrical poling process induces alignment of dipoles in the multilayer ferroelectric films and a large surface potential, leading to an additional increase in triboelectric output.

4.2 Experimental details

Preparation of materials

BaTiO₃ nanoparticles (BTO NPs) coated with polyvinylpyrrolidone (PVP) (average size of 200 nm) were purchased from U.S. Research Nanomaterials, Inc. The PVP coated BTO NPs were used to achieve uniform dispersion of nanoparticles in EtOH.²⁵²⁻²⁵³ The Poly(vinylidene fluoride-co-trifluoroethylene) (70/30) powder was obtained from Piezotech, France. The PVDF-TrFE powder (2 g) was dissolved in N,N-dimethylformamide (DMF) solvent (8 g) to prepare a 20 wt% solution. The PVDF-TrFE solution was stirred for 2 h at 40 °C to ensure uniform distribution. The PVP-coated BTO NPs powder was dispersed in EtOH to prepare a 3 wt% solution using bath-sonication for 1 h.

Fabrication of PVDF-TrFE/BaTiO₃ multilayered film

The PVDF-TrFE/DMF (20 wt%) solution was coated onto the Cu electrode using a bar coater with a coating speed of 6 mm/s, where a standard Meyer rod (RSD 3, RD Specialties, Inc.) with a diameter of 76 µm was used. To control the thickness of the films, PI tapes were rolled onto the Meyer rod. The controlled thickness of the PVDF-TrFE film was measured as approximately 10 µm. After coating, the films were dried for 30 min at 35 °C to reduce the surface roughness and then for 30 min at 60 °C to remove the remaining DMF. The BTO-PVP/EtOH suspension was coated onto the PVDF-TrFE coated Cu electrode using a bar coater with the same coating speed. Here, the Meyer rod RSD 2 with a diameter of 51 µm was used. After that, the coating and drying processes of PVDF-TrFE were repeated one more time. Then the sandwich structured PVDF-TrFE/BTO films were fabricated. To fabricate a multilayered PVDF-TrFE/BTO film, this fabrication process was repeated. Then, the film was annealed at 140 °C for 2 h. To align the dipole of ferroelectric material, an electric field of 30 MV/m was applied to the sample at 80 °C.

Characterization of material and device

All the experiments were performed under ambient conditions. The crystallinity of the PVDF-TrFE film and BaTiO₃ NPs were characterized using X-ray diffraction (XRD D8 ADVANCE, Bruker AXS, US) and the morphologies of the PVDF-TrFE/BTO multilayered film were investigated by field emission scanning electron microscopy (FE-SEM S-4800, Hitachi). A Fourier transform infrared (FT-IR 670/620, Varian, US) measurement was used to analyze the crystal structure conversion of the β-phase PVDF-TrFE film. Thermogravimetric analysis (TGA Q500, TA instruments, US) was performed to measure the BTO concentration inside the PVDF-TrFE/BTO multilayered film. The

triboelectric output voltage and current were measured using an oscilloscope (DPO 2022B, Tektronix, US) and source meter (2450-SCPI, Keithley, US), respectively, under the vertical pressure that was applied by the pushing tester (JIPT, JUNIL TECH, Korea). The contact area between Al and multilayer was $1 \times 1 \text{ cm}^2$. The capacitance was measured by an impedance analyzer (4192A, Agilent, US) to obtain the dielectric constant. The surface potential was characterized by a scanning Kelvin probe microscopy (SKPM MFP-3D, Asylum Research, Santa Barbara, US). The theoretical simulation was performed by COMSOL 5.4 multiphysics software. In a measurement system for acoustic sound wave detection, we analyzed the characteristics of acoustic sensors using triboelectric signals generated from the vibration of films depending on the applied acoustic energy. The sound source was applied by a speaker with a different frequency range (0.1–8 kHz) and sound pressure level (50–100 dB). The distance between the device and the speaker was fixed at 2 cm.

4.3 Results and discussions

The schematic in Figure 4.1a shows the multilayered hybrid TESs consisting of alternating PVDF-TrFE and BTO NP layers. To construct the TES devices, aluminum (Al) and copper (Cu) are used as the top and bottom electrodes, respectively. Here, the Al acts as both a top electrode and a positive triboelectric material, as it easily donates electrons when it makes contact with the multilayered films. The multilayered film is used as a negative triboelectric material, which is fabricated by repetitive bar-coating of the PVDF-TrFE solution and BTO NP solution alternatively on the Cu electrode and the annealing process (Figure 4.2a). BTO NPs (200 nm) were coated onto the PVDF-TrFE film with a surface density of 4.3 % (Figure 4.2b). Figure 4.1b exhibits the cross-sectional SEM image of a 4-layered PVDF-TrFE film (thickness of $\sim 50 \mu\text{m}$) with BTO interlayers. Each PVDF-TrFE layer has a regular thickness of approximately $10 \mu\text{m}$. The resulting multilayered PVDF-TrFE/BTO film shows a high flexibility (Figure 4.1c). The crystalline structures and phases of the ferroelectric PVDF-TrFE polymer and BTO NPs were analyzed via XRD and FT-IR measurements. Figure 4.3a shows the XRD pattern of the PVDF-TrFE with a single peak at 19.8° , corresponding to the ferroelectric β -phase of PVDF-TrFE. The XRD result of PVP-coated BTO NPs indicates a good crystalline structure with a ferroelectric tetragonal phase (Figure 4.3b).^{252, 254} Figure S2c exhibits the FT-IR analysis results of the PVDF-TrFE and PVDF-TrFE/BTO films, where three strong peaks at 850 cm^{-1} (CF_2 symmetric stretching), and 1400 cm^{-1} (CH_2 wagging vibration) indicate that both films have strong β -phase crystals after the annealing process.²⁵⁵⁻²⁵⁶

The working mechanism of TESs with the multilayer PVDF-TrFE/BTO film is based on the conjugation of triboelectrification and electrostatic induction effects (Figure 4.1d). When the Al electrode and PVDF-TrFE/BTO multilayered films are in contact under external forces, the Al surface is positively charged, and the multilayered film is negatively charged owing to the triboelectrification effect (I). Once the external force is released, a potential difference appears between the two materials. Owing to the electrostatic induction effect, the free electrons in the bottom electrode will flow to the top electrode through the external circuit to compensate for this potential difference, creating an output pulse (II). This current flow continues until it is neutralized (III). When two materials are in contact again, the triboelectric potential difference disappears, and the free electrons flow back into the circuit, creating an opposite output pulse (IV). Figure 4.1e exhibits typical output voltage ($\sim 45.7 \text{ V}$) and current density ($\sim 1.92 \mu\text{Acm}^{-2}$) signals of the 4-layered TESs.

Ferroelectric materials such as PVDF-TrFE with a residual dielectric polarization after the electrical poling process can improve the triboelectric output performance by enhancing the quantity of triboelectric charges on the surface through the coupling of residual dielectric polarization and surface polarization during the triboelectrification.²⁴⁶ In addition, BTO NPs with a high dielectric constant

additionally enhance the ferroelectric polarization of polymer and increase the capacitance of systems.^{246, 254} To investigate the effect of polarization and the addition of high-k BTO NPs, we measured the triboelectric performances of three different types of multilayered films: non-poled PVDF-TrFE, poled PVDF-TrFE, and poled PVDF-TrFE/BTO (Figure 4.4a). The current density and voltage of poled PVDF-TrFE films are enhanced by approximately 4.5 and 4 times compared to non-poled PVDF-TrFE films due to the effect of ferroelectric polarization, respectively (Figure 4.4b, c). These triboelectric performances match the surface potential analysis (Figure 4.4d), where the poled PVDF-TrFE film exhibits a higher surface potential (−2.85 V) than the non-poled PVDF-TrFE film (−0.65 V). Because the dipoles of non-poled PVDF-TrFE are randomly orientated, the sum of all dipole moments is not large. When an electric field of 30 MV/m is applied on the PVDF-TrFE during the poling process, the dipoles are aligned according to the direction of the applied electric field. The increased sum of the aligned dipoles provides a high surface potential in the PVDF-TrFE film and attract more surface charges to maintain the new equilibrium, leading to the enhanced surface charge density.²⁰ When alternating PVDF-TrFE and BTO NP layers are formed into multilayers, the 4-layered PVDF-TrFE film with BTO interlayers exhibits 2.3 and 1.8 times increased triboelectric current density and voltage compared to the one without BTO interlayer due to the high ferroelectric polarization induced by the high-k BTO NPs (Figure 4.4b, c). Therefore, the surface potential (−5.15 V) of poled PVDF-TrFE/BTO film is higher than that of poled PVDF-TrFE film (−2.85 V) (Figure 4.4d). Owing to the large difference of permittivity between PVDF-TrFE and BTO NPs, the local electric field is concentrated in the PVDF-TrFE, resulting in enhanced ferroelectric polarization.²⁵⁷ Moreover, the high permittivity of BTO NPs increases their ability to attract charges owing to increased capacitance of the composite film, leading to the improved triboelectric output performance.^{62, 111}

The triboelectric properties depend on the surface density of the BTO NPs. The surface density of BTO NPs can be controlled by the concentration (1, 3, 5 and 7 wt%) of BTO/EtOH solutions (Figure 4.5). Figure 4.5a shows the SEM images of BTO NP interlayers and the corresponding surface density analysis *via* the ImageJ software program. The average output current density of the multilayered PVDF-TrFE/BTO film increases with an increase in the surface density of BTO NPs up to 4.3 %, and then decreases up to 11.5 % (Figure 4.5b). The dielectric constant shows the same tendency as the output performances (Figure 4.5c). This critical surface density at 4.3% can be attributed to the competition between the enhanced dielectric constant with the addition of high-k BTO NPs and the increased aggregation with the increase in surface density of BTO NPs. The average size of the BTO NPs provides the degree of aggregation of the NPs (Figure 4.5d), which increases with the surface density of BTO NPs. The larger aggregation of BTO NPs leads to a decrease in dielectric breakdown strength, resulting in a decrease in the dielectric constant.¹⁴⁹ Therefore, a high dielectric constant with

optimized surface density and homogeneously dispersed BTO NPs with little aggregation enhances the triboelectric output performances.

The number of stacking layers affects the triboelectric property. Figure 4.6a and 4.6b show the output current density and voltage of the multilayered PVDF-TrFE films with and without BTO interlayers according to the number of stacking layers, which vary from 1 to 7 layers. The output performances of multilayered PVDF-TrFE films with BTO interlayers increase up to the 4-layered film and then slightly decrease. This result can be attributed to a thickness-dependent dielectric constant in the film. The thin dielectric film causes the leakage of current between the top and bottom electrodes, leading to a decrease in triboelectric surface charges. While the output is increased with increasing thickness of film due to reduced leakage current,²⁵⁸ the output with a thickness above 4 layers is rather decreased owing to the reduced dielectric constant of the film.²⁴⁵ The dielectric constant of the multilayered PVDF-TrFE/BTO film is increased up to that of the 4-layered film owing to reduced leakage current and then slightly reduced to a value close to that of the 7-layered film (Figure 4.6c, d). Multilayered PVDF-TrFE films without the BTO interlayer displayed a similar behavior. These results indicate that the output performances of PVDF-TrFE/BTO films critically depend on the thickness of the PVDF-TrFE film. In addition, the output performances of all multilayered PVDF-TrFE films with a BTO interlayer were higher than those of those without BTO owing to the high-k BTO NPs. The maximum output current density ($1.92 \mu\text{Acm}^{-2}$) and voltage (45.7 V) of the 4-layered PVDF-TrFE/BTO film were ~ 3 times higher than those ($0.6 \mu\text{A}$, 15 V) of the 1-layered film (Figure 4.7a, b).

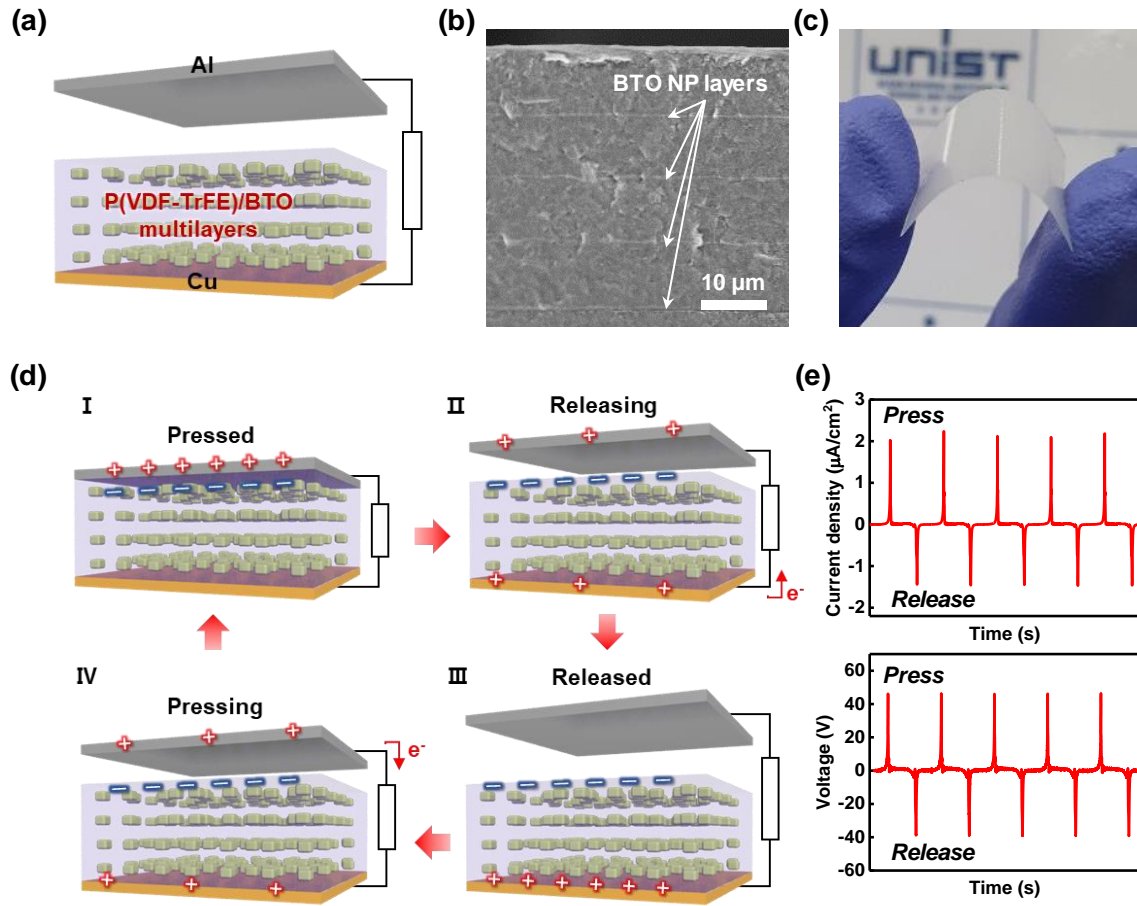


Figure 4.1. Multilayered TESs with aligned BTO NPs. (a) Schematic of the multilayered PVDF-TrFE/BTO based TESs. (b) Cross-sectional SEM image of the 4-layered film. (c) Photo of the 4-layered PVDF-TrFE/BTO film. (d) Working mechanism of the TESs with multilayered ferroelectric materials. (e) Output current density and voltage of multilayered TESs (4-layered film).

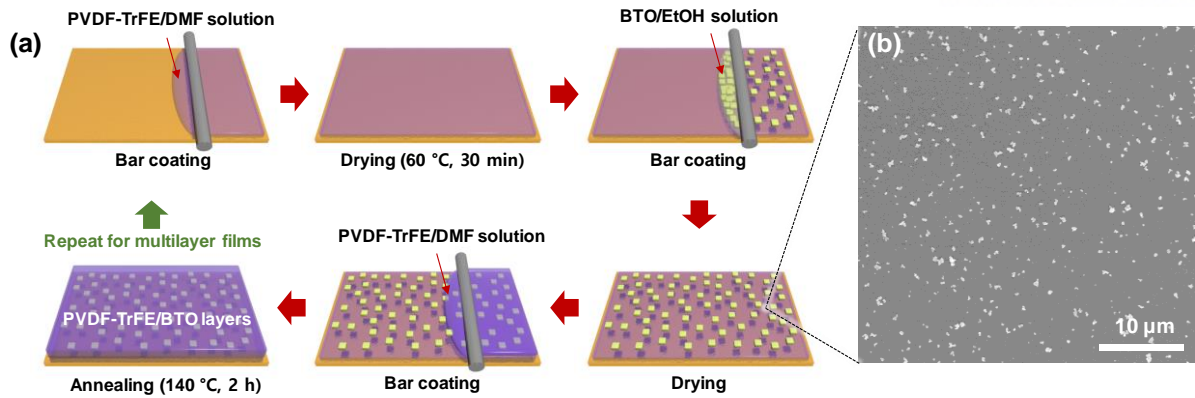


Figure 4.2. (a) Schematic illustrating the fabrication process of the multilayered PVDF-TrFE/BTO film. (b) SEM image of the BTO NPs coated on the PVDF-TrFE layer.

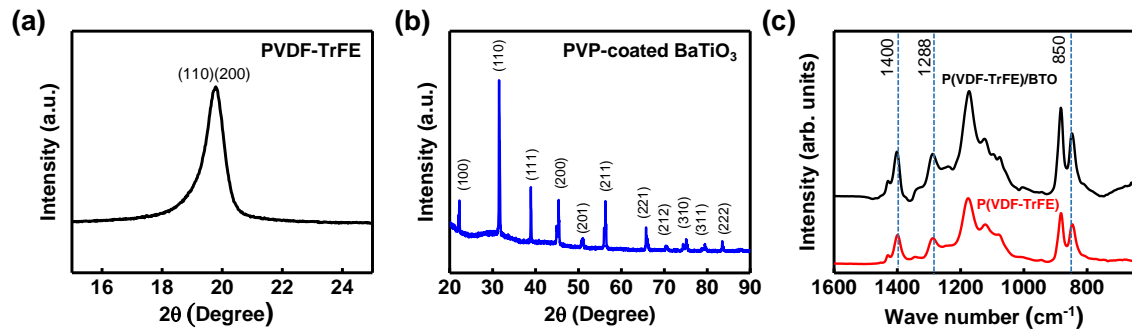


Figure 4.3. (a) X-ray diffraction (XRD) result of the PVDF-TrFE film with strong β -phase (110/200); (b) XRD patterns of the tetragonal BTO NPs; and (c) FT-IR spectrum of PVDF-TrFE and PVDF-TrFE/BTO film.

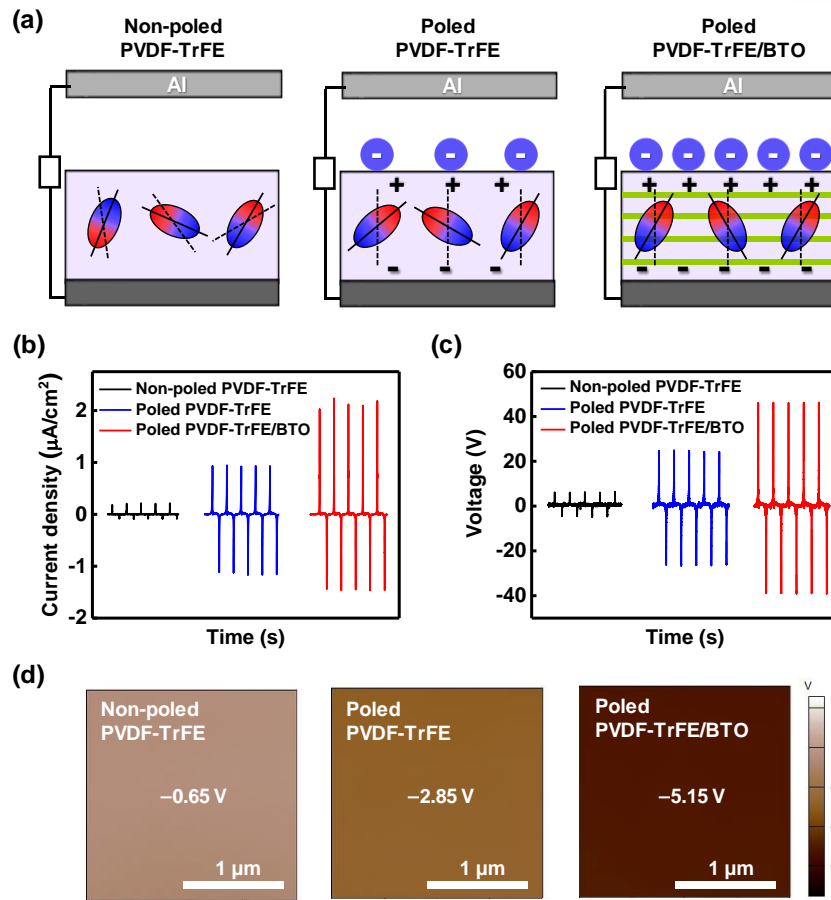


Figure 4.4. (a) Schematic of the three different TESSs: non-poled PVDF-TrFE, poled PVDF-TrFE, and poled PVDF-TrFE/BTO. Comparison of (b) the output current density and (c) voltage of the above three different types of 4-layered films under a vertical pressure of 98 kPa with 2 Hz. (d) Surface potential of different types of films measured by SKPM.

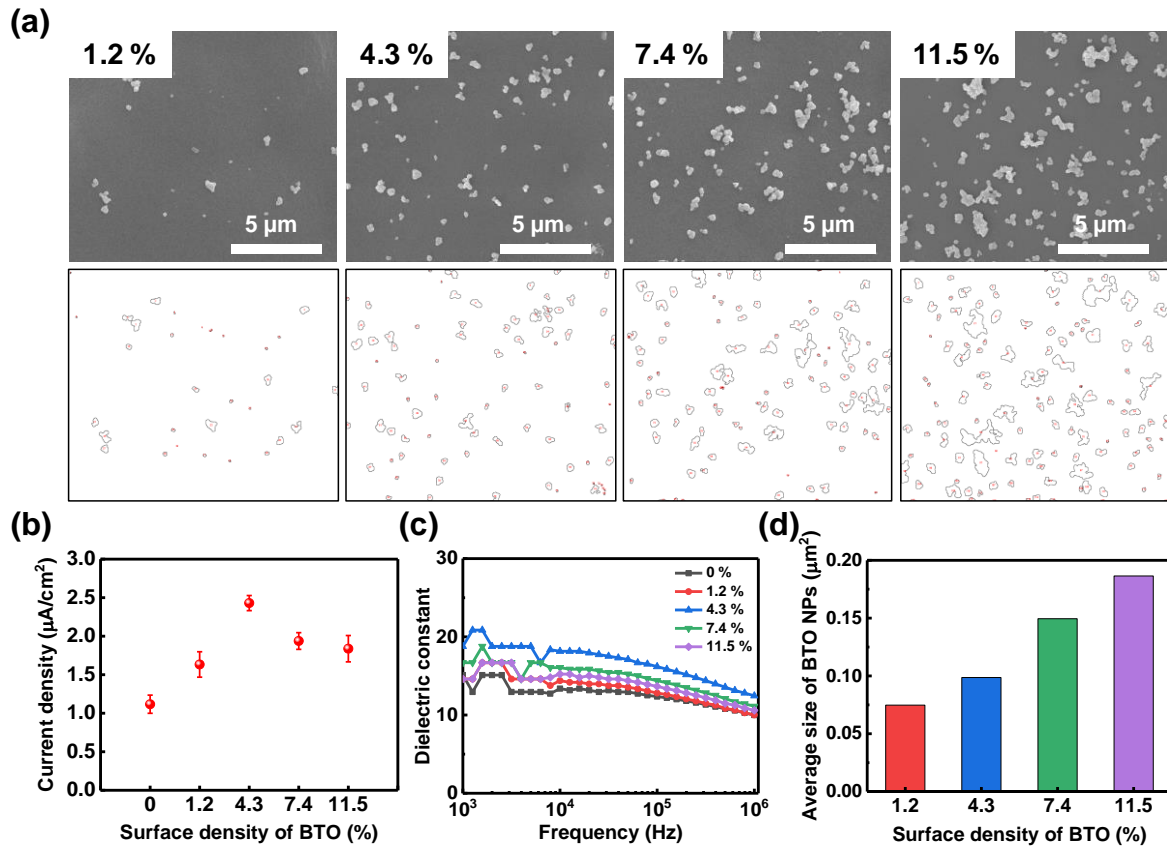


Figure 4.5. (a) SEM images of BTO interlayers coated on the PVDF-TrFE layer with a different surface density of BTO NPs; (b) output current density and (c) dielectric constant for the 4-layered PVDF-TrFE/BTO films with a different surface density. (d) Average size of BTO NPs at different surface densities of BTO NPs; ImageJ was used to approximate the surface densities.

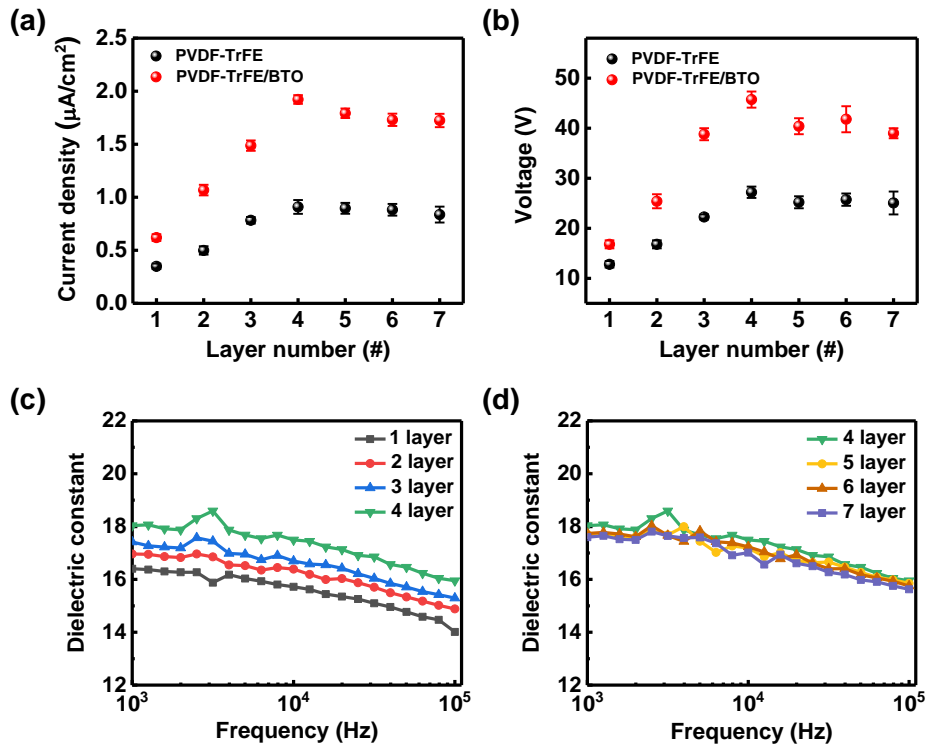


Figure 4.6. (a) Output current density and (b) voltage of the multilayered PVDF-TrFE films with and without BTO interlayers by increasing the number of layers, which range from 1 to 7. (c, d) Dielectric constant of the poled PVDF-TrFE/BTO for a various number of layers.

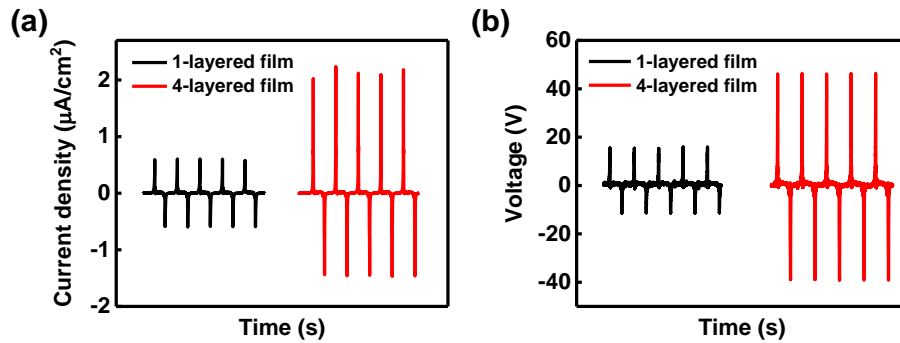


Figure 4.7. Comparison of (a) the output current density and (b) voltage of the 1-layered (black) and 4-layered PVDF-TrFE/BTO film (red).

Systematic investigation of BTO alignment effect on triboelectric properties

To investigate the effect of BTO NP interlayers on the triboelectric properties, we compared the triboelectric performance of three different types of films: single PVDF-TrFE, single PVDF-TrFE/BTO composite, and multilayered PVDF-TrFE/BTO films (Figure 4.8a). All the films had the same thickness as the 4-layered multilayer films ($\sim 50 \mu\text{m}$). The BTO concentration of the single PVDF-TrFE/BTO composite was the same as that of the multilayered PVDF-TrFE with the 6.5 wt% BTO NPs as measured by thermogravimetric analysis (TGA) (Figure 4.9). Figure 4.8b shows the average output current density and voltage of PVDF-TrFE and PVDF-TrFE/BTO films with single composite and multilayer structures. The multilayered PVDF-TrFE/BTO films exhibit an output current density of $1.77 \mu\text{Acm}^{-2}$ and voltage of 44.5 V, which are 1.5 and 1.3 times higher than those ($1.2 \mu\text{Acm}^{-2}$ and 35.4 V) of the composite film without a multilayer structure. The higher output performance of multilayered PVDF-TrFE/BTO films compared to that of the single composite film is attributed to the multilayer structure of alternating PVDF-TrFE/BTO layers, which increases the stress-induced polarization. In addition, the enhanced local field induced by the effective interfacial polarization in the multilayered PVDF-TrFE/BTO film can enhance the output performances. The large difference in dielectric constants between the high-k BTO and low-k PVDF-TrFE polymer induces interfacial polarization at the interface between BTO and PVDF-TrFE, resulting in concentration of the local field in the PVDF-TrFE near the BTO NPs under the triboelectric field. Additionally, the interfacial polarization between polymer and particle intensifies the local field in the polymer along the electric field direction, resulting in an increase in the ferroelectric polarization of the PVDF-TrFE polymer.^{257, 259} We simulated the resultant electric field distribution under applied voltage of 1.5 kV using the finite element method (FEM) based on COMSOL Multiphysics to compare the single and multilayer PVDF-TrFE/BTO composite structures (Figure 4.8c and 4.10). In this simulation, the film thickness of $50 \mu\text{m}$ and BTO particle size of 200 nm are used in the simulation in both structures, which are the same as in the experimental results. From the electric field distribution in Figure 4.8c, it is evident that compared to the composites with randomly dispersed BTO NPs, the multilayer structure with BTO NPs on the coplanar layer provides more efficiently connected interfacial charges with closer distances, resulting in a drastically enhanced local field, and thus increasing the ferroelectric polarization of polymer.²⁶⁰ In addition, the polarization simulation results in Figure 4.11 show that the interfacial polarization in the multilayer (8.4 mC/m^2) is higher than the single composite (8.06 mC/m^2). Therefore, enhanced polarization increases the dielectric constant of the multilayered film. Figure 4.8d shows the dielectric constant versus the frequency for different films. While the PVDF-TrFE/BTO films show a higher dielectric constant (15.9 at 10 kHz) than the PVDF-TrFE film (13.9 at 10 kHz) due to the high-k BTO NPs, the multilayered PVDF-TrFE/BTO film exhibits the largest dielectric constant (17.06 at 10 kHz) owing to the alignment and

closer distance of BTO NPs on the coplanar layer in the multilayered structure.²⁶⁰ In order to understand the effect of particle distribution on dielectric constant, we simulated the capacitance of the single and the multilayer structures of PVDF-TrFE/BTO composites with the same particle concentration within the frequency range of 102–105 Hz (Figure 4.12). The simulated capacitance of a multilayered PVDF-TrFE/BTO film (101.2 pF at 102 Hz) is found to be higher than that of a single PVDF-TrFE/BTO composite (89.7 pF at 102 Hz). In addition, the polymer interlayers between inorganic NP layers in multilayered films enhance the breakdown strength owing to the reduced leakage current in the insulating polymer layers, resulting in higher dielectric property than that of single composite (Figure 4.8a, d).^{257, 259} In this multilayer structure, the interfacial charges effectively trap the injected electrons from the metal electrode, preventing the leakage current and enhancing the dielectric breakdown strength.²⁵⁹ However, in random composites, when more than three particles form a chain with the direction aligned in the external field direction, the local field is further enhanced and form hot spots, which lead to the electron pathway for electron tunneling or conduction and decrease the dielectric breakdown strength of random composites. Therefore, the multilayer structures exhibited lower dielectric loss than the single composite with random NP dispersion (Figure 4.13).

The multilayered PVDF-TrFE/BTO films with alternating soft and hard layers can enhance the stress transfer and concentration around the BTO NPs. Due to the large difference in Young's moduli between the polymer and ceramic materials, the localized stress can be concentrated at the interface between two dissimilar materials, inducing an effective stress-induced polarization. In multilayered structures, the vertical stress is effectively transferred to the BTO NP coplanar layers owing to their horizontally aligned structure, efficiently enhancing the stress-induced polarization, resulting in the formation of increased surface potential in the PVDF-TrFE/BTO film. The enhanced stress-induced polarization in multilayer structures can be confirmed by comparing the piezoelectric property, which is dominantly affected by the stress-induced polarization.^{92, 125} For the piezoelectric devices (Figure 4.14a), the bottom surface of the film is attached on the Cu electrode, and the top surface of the film is deposited with the Pt electrode. The ferroelectric films with oriented dipoles produce the piezoelectric potential under the external pressure, inducing electron flow between two electrodes to balance the piezoelectric potential difference. Figure 4.14b exhibits the piezoelectric output current density of three different films. The PVDF-TrFE films including the BTO NPs exhibit higher output performance than the pure PVDF-TrFE films owing to the high piezoelectric properties of BTO NPs. On the other hand, the multilayer PVDF-TrFE/BTO films show higher output current density (8 nAcm⁻²) than the output (1 nAcm⁻²) of single PVDF-TrFE/BTO films. These results indicate that the alternating soft and hard layers can enhance the stress localization around the BTO NPs, resulting in a higher stress-induced piezoelectric potential in the multilayered film than in randomly dispersed BTO

NPs under the same external force.

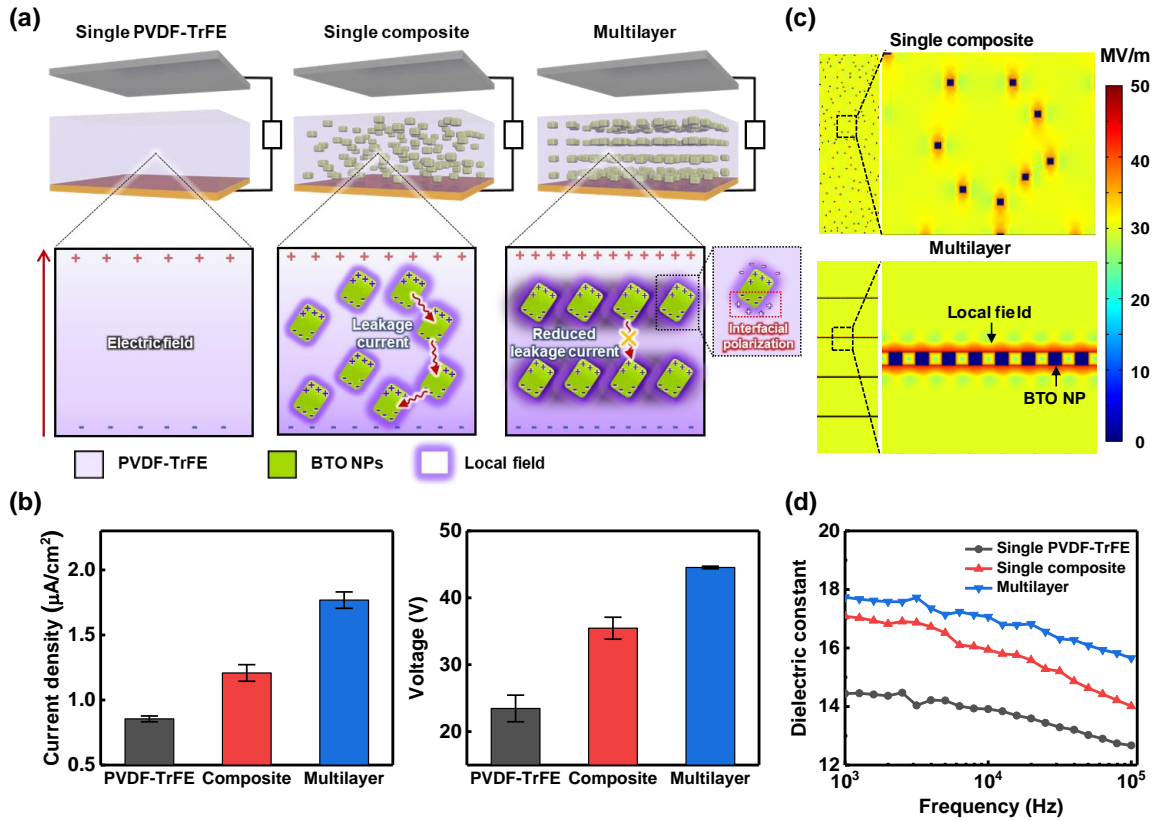


Figure 4.8. (a) Schematic of the three different types of samples with the same thickness: a PVDF-TrFE film, single PVDF-TrFE/BTO composite, and multilayered PVDF-TrFE/BTO film. Comparison of (b) the output current density and voltage under a vertical pressure of 98 kPa with 2 Hz. (c) FEM simulations of electric field distribution in the single and multilayered PVDF-TrFE/BTO composite films under Dirichlet boundary condition. (d) Comparison of the dielectric constant of the three different types of films.

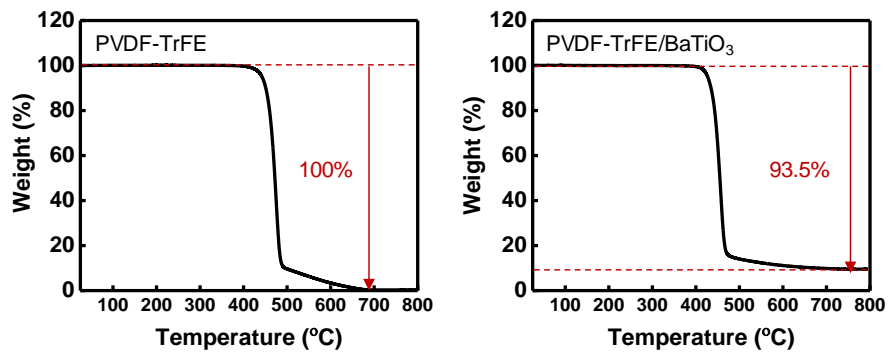


Figure 4.9. Thermogravimetric analysis (TGA) of the PVDF-TrFE and the PVDF-TrFE/BTO film.

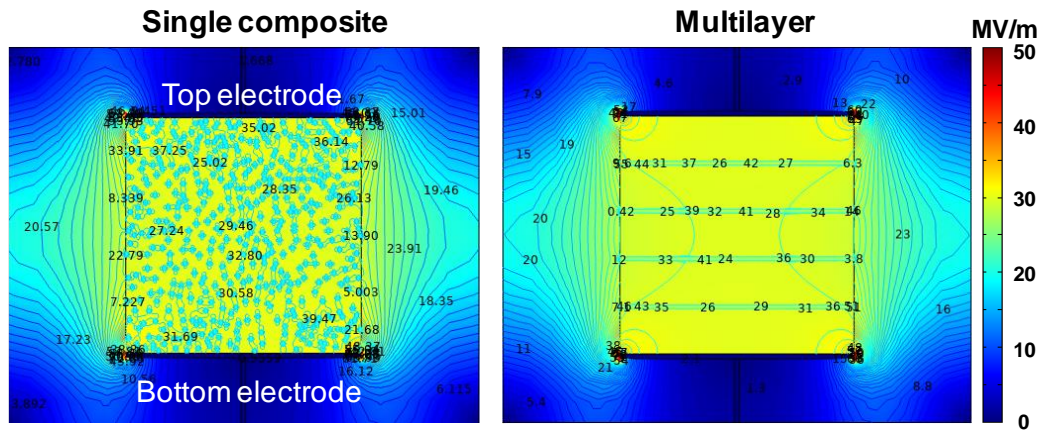


Figure 4.10. The contour plot of simulated electric field distribution in the single PVDF-TrFE/BTO composite and the multilayered PVDF-TrFE/BTO film having plate electrodes.

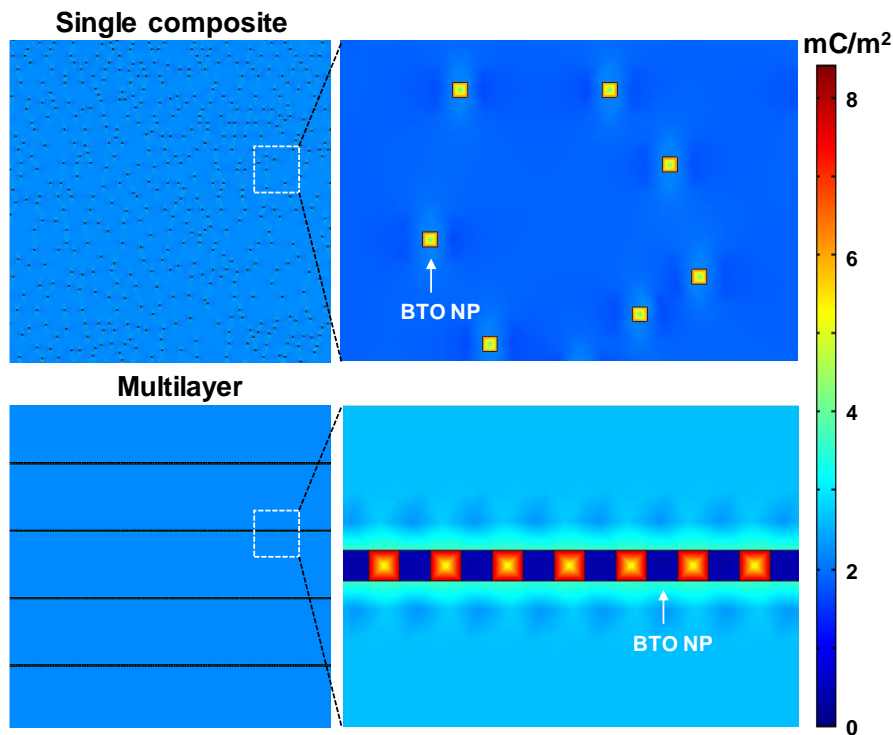


Figure 4.11. FEM Simulations of interfacial polarization in the single PVDF-TrFE/BTO composite and multilayered PVDF-TrFE/BTO film using Gauss's law under Dirichlet boundary condition.

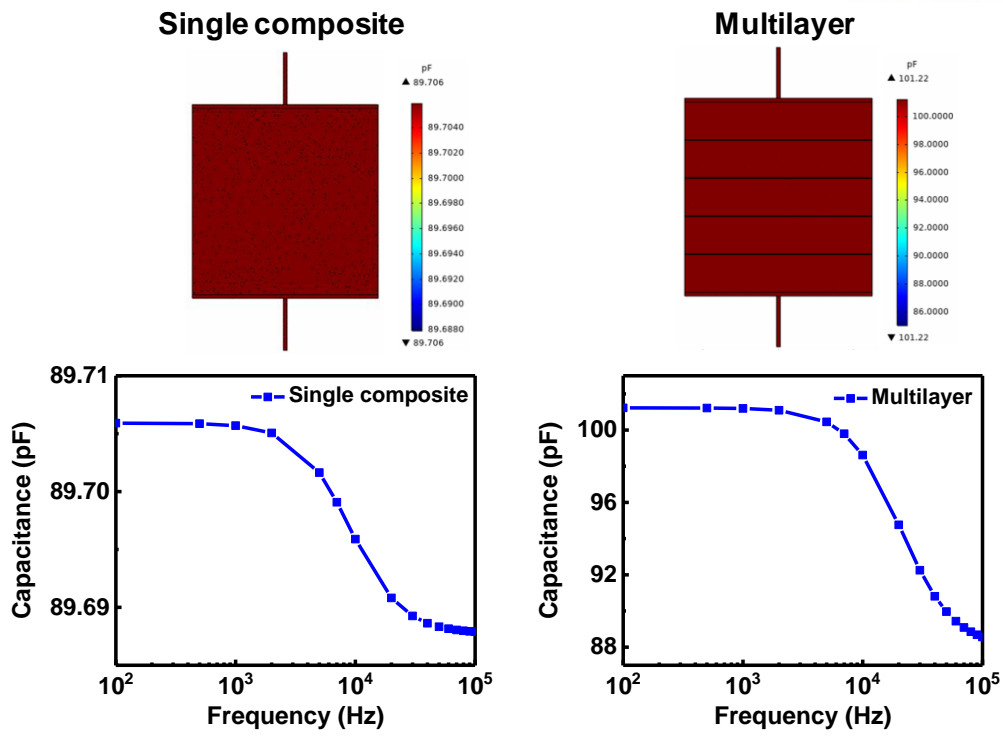


Figure 4.12. Simulations of capacitance in the single PVDF-TrFE/BTO composite and multilayered PVDF-TrFE/BTO film at frequency ranging from 10^2 – 10^5 Hz.

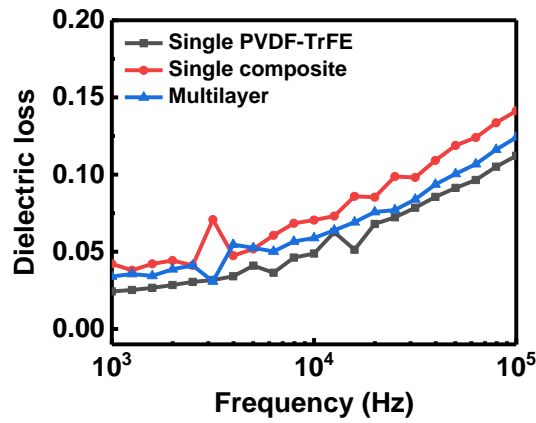


Figure 4.13. Dielectric loss of poled films for pure PVDF-TrFE, single PVDF-TrFE/BTO composite, and multilayered PVDF-TrFE/BTO composite films.

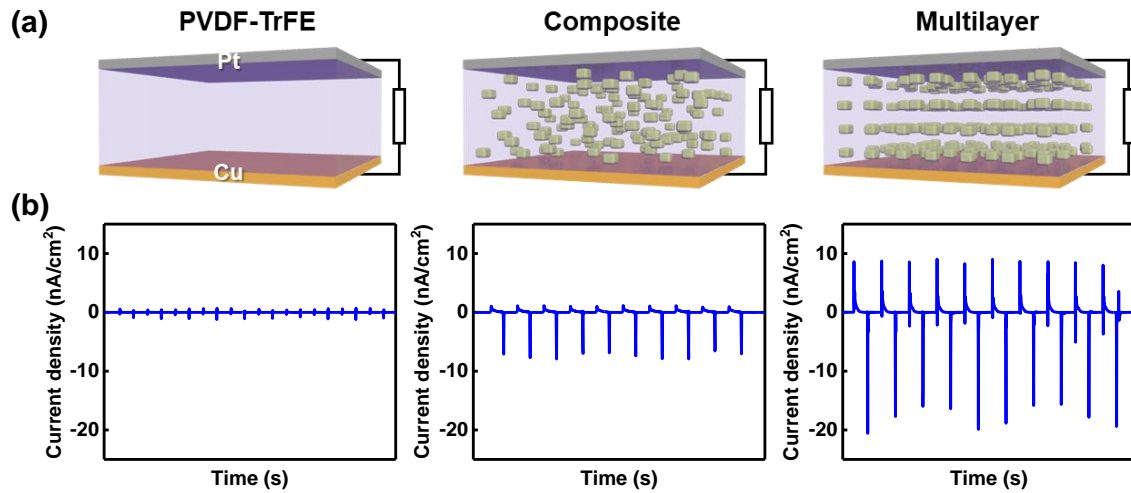


Figure 4.14. (a) Schematics of the three different types of samples: single PVDF-TrFE, single PVDF-TrFE/BTO composite, multilayered PVDF-TrFE/BTO. (b) Piezoelectric current density of the three different types of films. All the samples had the same thickness.

Performances of TESs based on multilayered ferroelectric films

To validate that the measured electrical current truly comes from the triboelectric effects of materials,¹⁷² we measured the triboelectric current density according to forward and reverse connection modes (Figure 4.15), which resulted in opposite peak signals with the same intensity for the forward and reverse connection modes. To evaluate the effect of mechanical pressure on power generation ability, we measured the output voltage and current of the multilayered PVDF-TrFE/BTO film under different loading pressures. Under the application of mechanical pressure with a constant frequency of 2 Hz, the output currents increased with pressure sensitivities of 48.7 nA/kPa (< 9.8 kPa) and 10.1 nA/kPa (> 9.8 kPa), respectively (Figure 4.16a). Similarly, the output voltage gradually increased with sensitivities of 0.94 V/kPa (< 9.8 kPa) and 0.22 V/kPa (> 9.8 kPa) (Figure 4.16b). Our TES device exhibited a competitive pressure sensitivity compared to other thin-film based TESs (Table 4.1). Although some papers have reported that TESs have higher pressure sensitivity, they have a narrow pressure range and a relatively lower power density.²⁶¹⁻²⁶² The multilayered PVDF-TrFE/BTO film exhibited a high reversibility during the cyclic test of 10,000 times. The current density under different pressure remains constant without any degradation (Figure 4.17). We further investigated the energy harvesting performances of TESs. For loading resistance from 1 k Ω to 750 M Ω , the current density signal decreased and the voltage increased with increasing load resistance (Figure 4.16c). As a result, the output power density reached the maximum value of 29.4 μWcm^{-2} at a load resistance of 100 M Ω (Figure 4.16d). The power density of our TES is comparable with the other thin-film based TESs (Table 4.1). For practical applications of the TESs, we connected a commercial rectifier to the TESs to convert the AC voltage into a DC voltage output, and a commercial green emission light-emitting device (LEDs) is connected to the rectifier. The rectified output voltage is displayed in Figure 4.18a. The periodic vertical force turns on the green LED light by using the rectified electricity (Figure 4.18b).

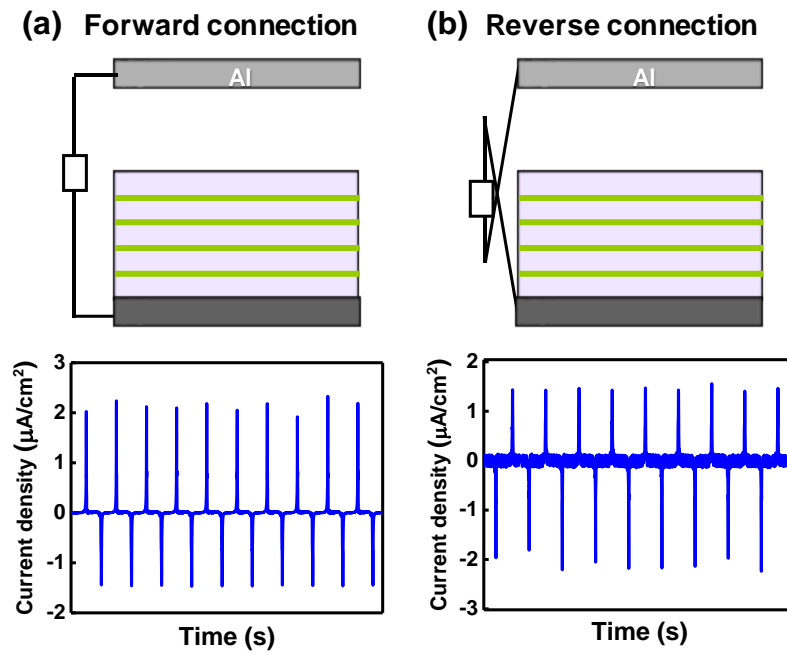


Figure 4.15. Schematic and output current density of the TESs (a) in the forward connection and (b) in the reverse connection.

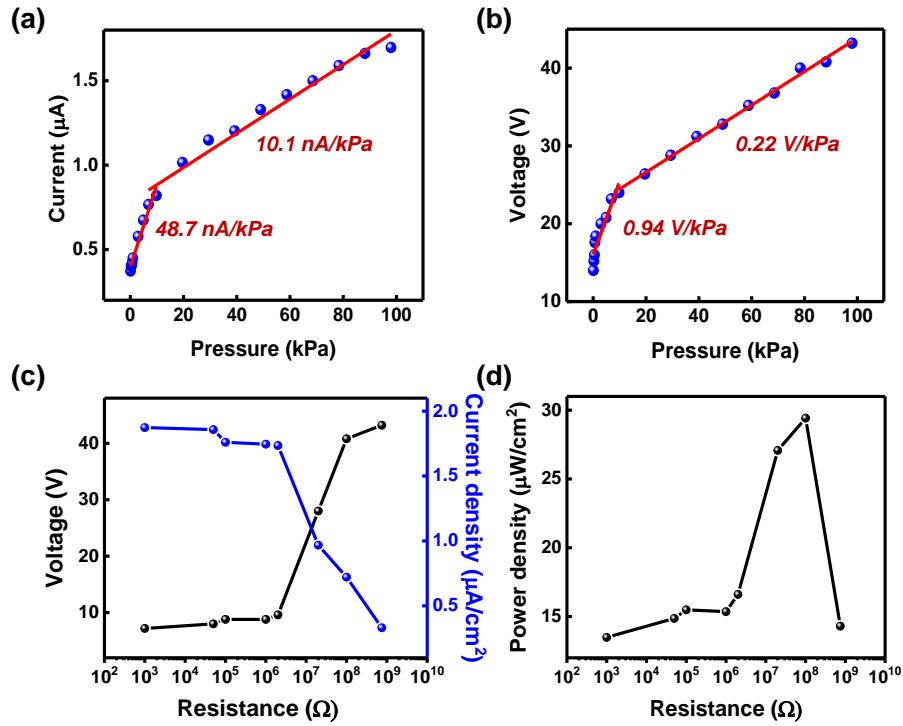


Figure 4.16. (a) Output current and (b) voltage of the four-layered PVDF-TrFE/BTO film depending on the applied pushing force up to 98 kPa. (c) Output voltage and current density at loading resistances ranging from 1 k Ω to 750 M Ω . (d) Optimized maximum output power density at 100 M Ω .

Table 4.1. Summary of thin-film based triboelectric sensors and their pressure sensitivities.

Ref.	Major materials	Pressure sensitivity	Pressure range	Power density ($\mu\text{W cm}^{-2}$)
241	Latex membrane, FEP	0.04 V kPa^{-1}	3–6.2 kPa	—
197	PDMS, Al	0.06 kPa^{-1}	1–80 kPa	—
231	PDMS, ITO	$0.00282 \text{ V kPa}^{-1}$	<428.8 kPa	0.13
196	PTFE, Cu-deposited hemispheres structured film	0.5 V N^{-1}	0–40 N	2.45
207	PDMS, Cu NWs	0.028 V N^{-1}	40–140 N	—
240	Hybridizing elastomer, dielectric film	0.013 kPa^{-1}	1.3–70 kPa	3.5
201	Self-polarized PVDF-TrFE, PDMS	0.104 V kPa^{-1} (0.05–5 kPa) 0.055 V kPa^{-1} (5–60 kPa) 0.049 V kPa^{-1} (60–600 kPa)	0.05–600 kPa	—
205	Patterned PDMS, Al	0.006 kPa^{-1}	0.6–200 kPa	—
263	PDMS, metal layer	0.414 V N^{-1} (0–100 N) 0.204 V N^{-1} (100–200 N)	<200 N	11
262	PDMS, PDMS/CNT nanocomposites	0.51 V kPa^{-1}	5–450 kPa	7
75	Hierarchical PDMS, P(VDF-TrFE)	0.55 V kPa^{-1} (< 19.8 kPa) 0.2 V kPa^{-1} (19.8–100 kPa)	<100 kPa	46.7
261	PTFE, ITO	1.75 V kPa^{-1}	10–40 kPa	16
This work	Multilayered PVDF-TrFE/BTO, Al	0.94 V kPa^{-1} (0.098–9.8 kPa) 0.22 V kPa^{-1} (9.8–98 kPa)	<100 kPa	29.4

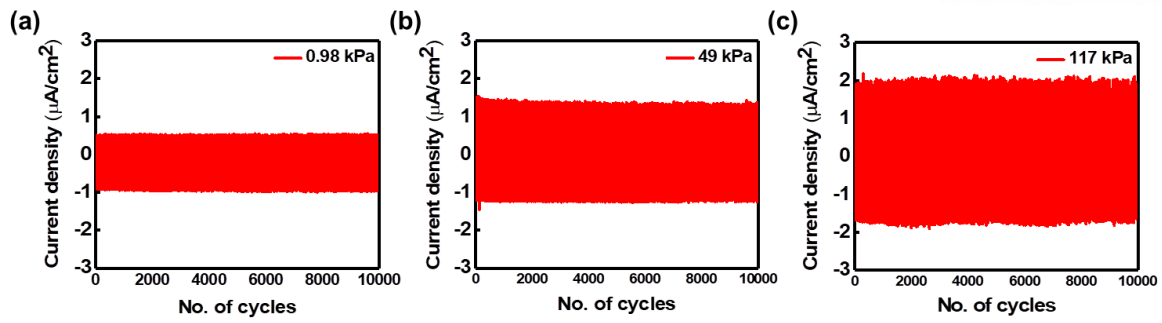


Figure 4.17. Stability of poled PVDF-TrFE/BTO multilayer film for (a) low-pressure of 0.98 kPa (b) medium-pressure of 49 kPa, and (c) high-pressure of 117 kPa.

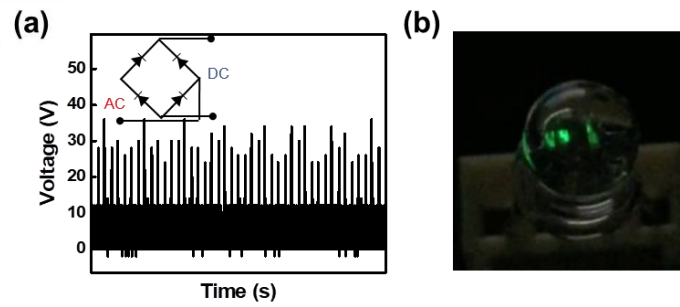


Figure 4.18. (a) Rectified voltage of the four-layered PVDF-TrFE/BTO film and (b) a photograph showing the ability of TESs to drive LEDs.

Application of multilayered TESs in healthcare monitoring devices

Our thin-film multilayered TESs with a high sensitivity and flexibility are beneficial for applications in self-powered and skin-attachable healthcare devices to detect bio-signals such as carotid and radial artery pulse pressures, human breath, and an acoustic wave. Figure 4.19a illustrates the triboelectric device structure consisting of the multilayered PVDF-TrFE/BTO film sputtered with a Pt electrode and an Al-coated PET film, where the triboelectric outputs are achieved by contact and separation between Al and the multilayered films. The polyimide (PI) tape as a spacer is attached to each side of the film to separate the two contact surfaces. The TES detects the radial artery pressure on the wrist, the carotid artery pressure on the neck and the human breath pressure on the nostrils. In Figure 4.19b, the periodic electrical signals show a heart rate of 80 beats/min. In addition, three distinct peaks of P_1 , P_2 , and P_3 are observable, where P_1 is the pulse wave, P_2 and P_3 are the reflected wave from the hand and lower body, respectively.²⁶⁴⁻²⁶⁵ From these parameters, we obtained an artery augmentation index ($AI_r = P_2/P_1$) of 0.4 and a radial diastolic augmentation index ($DAI = P_3/P_1$) of 0.2, which are similar to that of a healthy 25-year-old woman.²¹³ In addition, our sensor can accurately recognize the carotid artery pressure and human breath. In Figure 4.19c, distinct peaks of P_1 and P_2 provide a pressure augmentation index ($PAI = (P_2 - P_1)/(P_2 - P_0)$). The PAI increases linearly with age, providing information about cardiovascular conditions. The PAI value obtained was that of the healthy 25-year-old woman ($PAI = -2$).²⁶⁶ For repeated human breathing, we observed periodical opposite direction peaks indicating inspiration and exhalation (Figure 4.19d). The multilayered film and Al-coated PET film contact with each other and generate the output via airflow during the inspiration. Then, the opposite direction peak appears due to the separation process during the exhalation. These results indicate that our TES has a great potential for applications in health monitoring devices.²⁶⁷

Multilayered TESs with the capability of high-frequency stimuli detection can be used for flexible acoustic sensors (Figure 4.19e). We compared the output voltage with three different types (non-poled PVDF-TrFE, poled PVDF-TrFE, and poled multilayered PVDF-TrFE/BTO films) of sensors in the frequency range from 100 Hz to 8 kHz (Figure 4.19f). All sensors have a maximum output voltage at a resonance frequency of 400 Hz. Similar to the triboelectric output performances, the poled multilayered PVDF-TrFE/BTO sensor exhibits a higher output voltage than the non-poled and poled PVDF-TrFE sensors. When the sound source of a “Triboelectric sensor” is applied on the sensor, the sound waveform and short-time Fourier transform (STFT) signals of multilayered sensors match well with those of the original source compared to other non-poled and poled PVDF-TrFE sensors (Figure 4.19g). We additionally confirmed the detection of different sound pressure levels (SPL) under a fixed frequency of 400 Hz (Figure 4.20). The output voltage of the multilayered TESs gradually increased with an increase in SPL. These results suggest that multilayered TESs can find various applications in self-powered microphones and voice security systems.

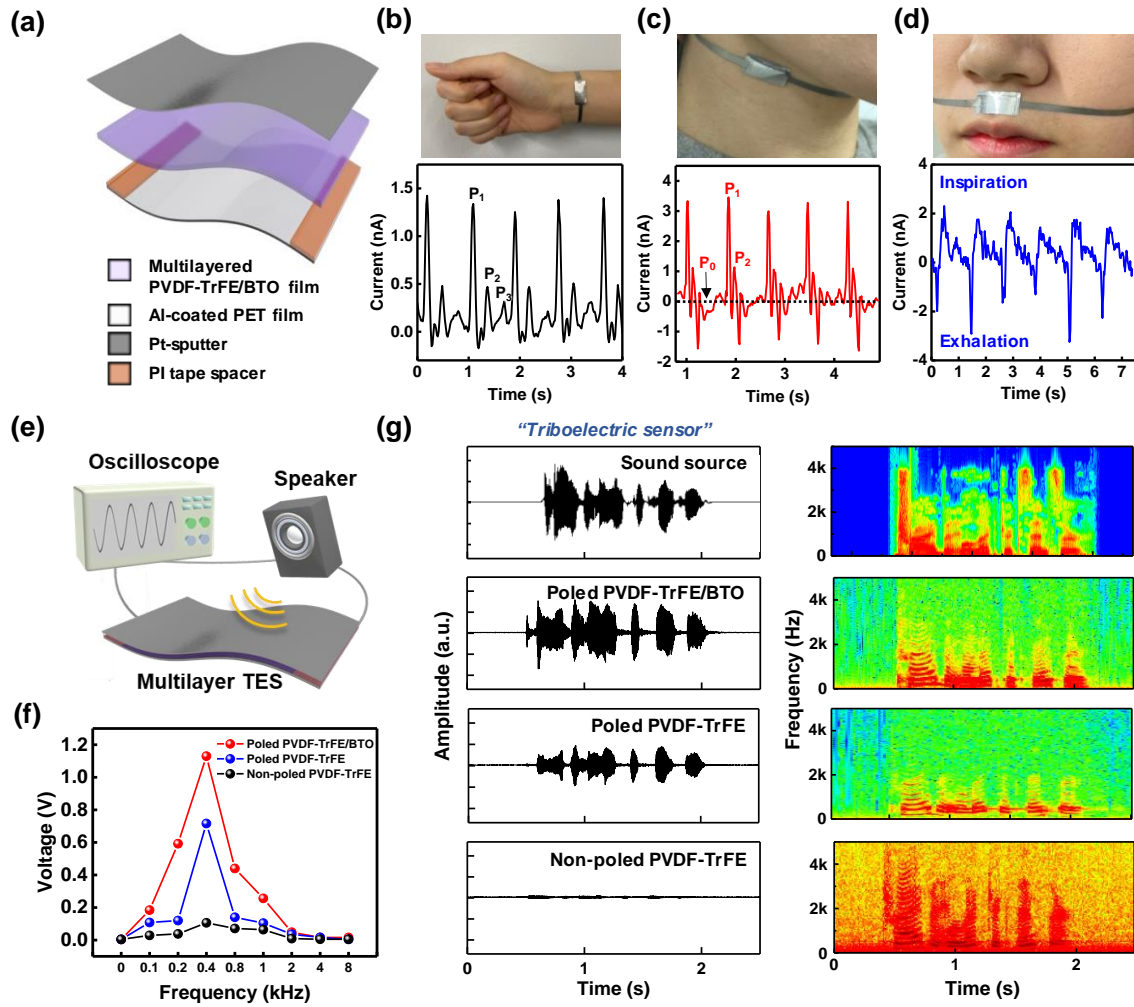


Figure 4.19. (a) Schematic of the multilayered PVDF-TrFE/BTO TES device. Current signals and photographs of the multilayered TESs in response to (b) radial artery pressure on the wrist and (c) carotid pulse pressure on the neck. (d) Current signals and photographs of the multilayered TESs in response to human breath on the area below the nose. (e) Measurement system for acoustic sound wave detection. (f) Voltage signals of three different types of TESs as a function of a sound frequency. (g) Time-dependent sound waveforms and short-time Fourier transform (STFT) signals of the sound source ("Triboelectric sensor") and three types of TES: non-poled and poled PVDF-TrFE TES, and poled PVDF-TrFE/BTO TES.

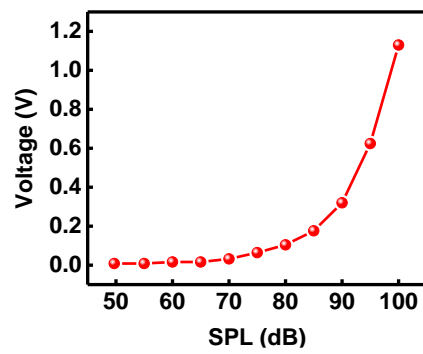


Figure 4.20. Voltage signals of a poled multilayered PVDF-TrFE/BTO sensor as a function of sound pressure level.

4.4 Conclusions

We developed high-performance triboelectric devices through the structural design of ferroelectric multilayers with alternating PVDF-TrFE and BTO NP layers for enhanced polarization and stress concentration effects. The output performances of the TESs with alternating organic/inorganic ferroelectric multilayers were largely increased by the large stress-induced polarization and enhanced dielectric constant of ferroelectric multilayers. The ferroelectric multilayers exhibited an enhanced dielectric constant (17.06) compared to those of pure PVDF-TrFE films (13.9) and single PVDF-TrFE/BTO composites (15.9) at 10 kHz. Consequently, the multilayered TESs exhibited 2.3 and 1.5 times increased triboelectric current density compared to those pure PVDF-TrFE and PVDF-TrFE/BTO composites without a multilayer structure, respectively. The multilayered TESs exhibited a high pressure sensitivity of 0.94 V/kPa (48.7 nA/kPa) and power density ($29.4 \mu\text{Wcm}^{-2}$). For practical applications of multilayered TESs, we demonstrated flexible healthcare monitoring devices that can precisely detect the pulse pressure and human breath; furthermore, we demonstrated a possibility for flexible and high-performance acoustic sensors. The design of ferroelectric multilayers with alternating soft and hard layers can be an efficient platform for the development of high-performance triboelectric devices for applications in self-powered sensors and wearable devices.

Chapter 5. Summary and future perspective

In this thesis, we demonstrate advanced sustainable wearable sensors with better wearing sensation, multimodality, and enhanced sensory functions through structure design and modification of material characteristics. Moreover, we suggested promising applications such as body motion detection, healthcare monitoring, acoustic detection, and simultaneous multiple tactile sensing. In particular, triboelectric sensors which do not rely on an external power source have been intensely studied for self-powered wearable sensors, leading to advantages of high efficiency, facile fabrication, as well as sustainability. In addition, ferroelectric polymers have been used for enhanced wearing sensation, high sensitivity and multimodality. Especially, PVDF and its copolymer have been utilized for advanced wearable sensors which are developed *via* structure design (textile based on as-spun fiber, ultrathin film, alternating multilayer structure) and property modification (switchable polarity and controlled permittivity).

In Chapter 1, we provided a brief introduction of wearable sensors including definition of wearable sensors, recent research progress and potential applications. Especially, we suggested fundamental working principles for self-powered sensing systems, and strategies for enhanced performance to go along with each principle. In addition, we explained ferroelectric polymer which is promising material for high performance wearable sensors in terms of fundamental characteristics, functionality, and potential uses.

In Chapter 2, PVDF-stitch-based triboelectric sensors were demonstrated by using a sewing machine for the practical uses of wearable sensors. Due to the all-stitched structures, PVDF stitch sensors exhibited high mechanical properties including flexible, light weight, comfortable, and wearable forms. Furthermore, the sensing performances were stable without significant decrease after tens of times repeated washing cycle, which provides the possibility for practical uses. The proposed PVDF stitch sensor can detect and distinguish various hand gestures, body motions, and pulse pressure in real time. Our PVDF stitch sensors can be easily fabricated onto commercial fabrics using a sewing machine. Therefore, our suggested strategy can be readily extended for other functional applications when integrating with diverse stitch patterns, and functional materials, paving a new way for the facile, low-cost and large-scale fabrication of self-powered wearable sensors in commercial clothes and garments.

In Chapter 3, we provided an efficient strategy for high-performance triboelectric and pyroelectric-based multimodal sensors *via* modulation of triboelectric polarity of the ferroelectric copolymer by electrical polarization. Compared to conventional triboelectric devices, identical material was used as the contact pair materials, which is attributed to the switchable triboelectric polarity resulting from the aligned dipole direction in P(VDF-TrFE) depending on the applied polarization bias direction.

Consequently, the device with inversely polarized films has noticeably enhanced triboelectric and pyroelectric output performances compared to the device with non-polarized ones. Our sensor can be utilized for the monitoring of weak pulse pressure and simultaneous tactile detection under multiple stimuli without interference signals. Our strategy provides a feasible route to remarkably enhance the output performances of multimodal sensors based on identical material *via* modulation of triboelectric polarity without any additional chemical functionalization or mechanical modification on the opposite materials in a contact pair.

In Chapter 4, we demonstrated high performance triboelectric sensors through the novel design of structure with alternating P(VDF-TrFE) and BTO NP layers for enhanced polarization and stress concentration effects. Consequently, the output performances of P(VDF-TrFE)/BTO NP multi-layer structures were noticeably increased, which is attributed to the large stress-induced polarization and enhanced dielectric constant of ferroelectric multilayers. Due to the high pressure sensitivity of 0.94 V/kPa (48.7 nA/kPa) and power density ($29.4 \mu\text{Wcm}^{-2}$), we demonstrated the flexible healthcare monitoring for pulse pressure as well as respiration. Moreover, our sensor can be used for acoustic sensing, resulting from high flexibility and sensitivity. Our strategy provides a novel design of ferroelectric multilayers with alternating soft and hard layers, which can be an efficient platform for the development of high-performance triboelectric devices for applications in self-powered sensors and wearable devices

Overall, this thesis suggested the strategy for high performance self-powered wearable sensors with enhanced wearing sensation, high sensitivity, high stability/durability, and multimodality without signal interference, resulting from a unique structure design and facile approach for material characteristic modification. For the proof-of-concept, we successfully showed our wearable sensors to various applications such as body motion monitoring, real-time gait pattern monitoring, healthcare monitoring, acoustic sensing, and simultaneous multiple tactile sensing. We believe that our research will contribute to improving the technical advancement in wearable electronics which can be utilized in various practical applications for smart life and wellness.

Reference

1. Takei, K.; Honda, W.; Harada, S.; Arie, T.; Akita, S., Toward flexible and wearable human-interactive health-monitoring devices. *Adv. Healthcare Mater.* **2015**, *4* (4), 487-500.
2. Khan, Y.; Ostfeld, A. E.; Lochner, C. M.; Pierre, A.; Arias, A. C., Monitoring of vital signs with flexible and wearable medical devices. *Adv. Mater.* **2016**, *28* (22), 4373-4395.
3. Heikenfeld, J.; Jajack, A.; Rogers, J.; Gutruf, P.; Tian, L.; Pan, T.; Li, R.; Khine, M.; Kim, J.; Wang, J., Wearable sensors: modalities, challenges, and prospects. *Lab Chip* **2018**, *18* (2), 217-248.
4. Trung, T. Q.; Lee, N. E., Flexible and stretchable physical sensor integrated platforms for wearable human-activity monitoring and personal healthcare. *Adv. Mater.* **2016**, *28* (22), 4338-4372.
5. Hammock, M. L.; Chortos, A.; Tee, B. C. K.; Tok, J. B. H.; Bao, Z., 25th anniversary article: the evolution of electronic skin (e-skin): a brief history, design considerations, and recent progress. *Adv. Mater.* **2013**, *25* (42), 5997-6038.
6. Kim, D.-H.; Lu, N.; Ma, R.; Kim, Y.-S.; Kim, R.-H.; Wang, S.; Wu, J.; Won, S. M.; Tao, H.; Islam, A., Epidermal electronics. *Science* **2011**, *333* (6044), 838-843.
7. Herbert, R.; Kim, J.-H.; Kim, Y. S.; Lee, H. M.; Yeo, W.-H., Soft material-enabled, flexible hybrid electronics for medicine, healthcare, and human-machine interfaces. *Materials* **2018**, *11* (2), 187.
8. Liu, Y.; Pharr, M.; Salvatore, G. A., Lab-on-skin: a review of flexible and stretchable electronics for wearable health monitoring. *ACS Nano* **2017**, *11* (10), 9614-9635.
9. Lim, H. R.; Kim, H. S.; Qazi, R.; Kwon, Y. T.; Jeong, J. W.; Yeo, W. H., Advanced soft materials, sensor integrations, and applications of wearable flexible hybrid electronics in healthcare, energy, and environment. *Adv. Mater.* **2020**, *32* (15), 1901924.
10. Lee, B.-Y.; Kim, D. H.; Park, J.; Park, K.-I.; Lee, K. J.; Jeong, C. K., Modulation of surface physics and chemistry in triboelectric energy harvesting technologies. *Sci. Technol. Adv. Mater.* **2019**, *20* (1), 758-773.
11. Kim, S. Y.; Park, S.; Park, H. W.; Park, D. H.; Jeong, Y.; Kim, D. H., Highly sensitive and multimodal all-carbon skin sensors capable of simultaneously detecting tactile and biological stimuli. *Adv. Mater.* **2015**, *27* (28), 4178-4185.
12. Tien, N. T.; Jeon, S.; Kim, D. I.; Trung, T. Q.; Jang, M.; Hwang, B. U.; Byun, K. E.; Bae, J.; Lee, E.; Tok, J. B. H., A flexible bimodal sensor array for simultaneous sensing of pressure and temperature. *Adv. Mater.* **2014**, *26* (5), 796-804.
13. Amjadi, M.; Kyung, K. U.; Park, I.; Sitti, M., Stretchable, skin-mountable, and wearable

- strain sensors and their potential applications: a review. *Adv. Funct. Mater.* **2016**, 26 (11), 1678-1698.
14. Wang, Z. L., Triboelectric nanogenerators as new energy technology for self-powered systems and as active mechanical and chemical sensors. *ACS Nano* **2013**, 7 (11), 9533-9557.
 15. Liu, W.; Wang, Z.; Wang, G.; Liu, G.; Chen, J.; Pu, X.; Xi, Y.; Wang, X.; Guo, H.; Hu, C., Integrated charge excitation triboelectric nanogenerator. *Nat. Commun.* **2019**, 10 (1), 1-9.
 16. Kang, H.; Zhao, C.; Huang, J.; Ho, D. H.; Megra, Y. T.; Suk, J. W.; Sun, J.; Wang, Z. L.; Sun, Q.; Cho, J. H., Fingerprint-Inspired Conducting Hierarchical Wrinkles for Energy-Harvesting E-Skin. *Adv. Funct. Mater.* **2019**, 29 (43), 1903580.
 17. Chen, F.; Wu, Y.; Ding, Z.; Xia, X.; Li, S.; Zheng, H.; Diao, C.; Yue, G.; Zi, Y., A novel triboelectric nanogenerator based on electrospun polyvinylidene fluoride nanofibers for effective acoustic energy harvesting and self-powered multifunctional sensing. *Nano Energy* **2019**, 56, 241-251.
 18. Wang, Z. L.; Song, J., Piezoelectric nanogenerators based on zinc oxide nanowire arrays. *Science* **2006**, 312 (5771), 242-246.
 19. Hu, Y.; Lin, L.; Zhang, Y.; Wang, Z. L., Replacing a battery by a nanogenerator with 20 V output. *Adv. Mater.* **2012**, 24 (1), 110-114.
 20. Yang, Y.; Jung, J. H.; Yun, B. K.; Zhang, F.; Pradel, K. C.; Guo, W.; Wang, Z. L., Flexible pyroelectric nanogenerators using a composite structure of lead-free KNbO₃ nanowires. *Adv. Mater.* **2012**, 24 (39), 5357-5362.
 21. Yang, Y.; Guo, W.; Pradel, K. C.; Zhu, G.; Zhou, Y.; Zhang, Y.; Hu, Y.; Lin, L.; Wang, Z. L., Pyroelectric nanogenerators for harvesting thermoelectric energy. *Nano Lett.* **2012**, 12 (6), 2833-2838.
 22. Kraemer, D.; Poudel, B.; Feng, H.-P.; Caylor, J. C.; Yu, B.; Yan, X.; Ma, Y.; Wang, X.; Wang, D.; Muto, A., High-performance flat-panel solar thermoelectric generators with high thermal concentration. *Nat. Mater.* **2011**, 10 (7), 532.
 23. Hochbaum, A. I.; Chen, R.; Delgado, R. D.; Liang, W.; Garnett, E. C.; Najarian, M.; Majumdar, A.; Yang, P., Enhanced thermoelectric performance of rough silicon nanowires. *Nature* **2008**, 451 (7175), 163.
 24. Ryu, H.; Yoon, H. J.; Kim, S. W., Hybrid energy harvesters: Toward sustainable energy harvesting. *Adv. Mater.* **2019**, 31 (34), 1802898.
 25. i-SCOOP Home page. <https://www.i-scoop.eu/industry-4-0/> (accessed May 11).
 26. UbuntuPIT home page. <https://www.ubuntupit.com/top-20-emerging-iot-trends-that-will-shape-your-future-soon/> (accessed May 12).
 27. i-scoop home page. <https://www.i-scoop.eu/industry-4-0/>, (accessed May 12).

28. Medallia Strikedeck home page. <https://strikedeck.com/will-customer-insights-and-customer-success-converge/> (accessed May 12).
29. HUFFPOST home page. https://www.huffpost.com/entry/lesia-trubat_n_6148618 (accessed May 12).
30. Top gadgets daily home page. <https://topgadgetsdaily.com/article/topgadgetsfb.php?affId=76E606D5> (accessed May 12).
31. Smart Gadget Genius home page. <http://smartgadgetgenius.com/wearable-technology/> (accessed May 12).
32. European Pharmaceutical Review (EPR) home page. <https://www.europeanpharmaceuticalreview.com/news/64021/breathable-wearable-electronics/> (accessed May 12).
33. BBN Times home page. <http://www.bbntimes.com/technology/at-fashionable-ces-wearable-electronics-are-the-new-black> (accessed May 12).
34. Wearable Ltd. home page. <https://www.wearable.com/smart-clothing/thin-ice-system-weight-loss-clothing-line-2710> (accessed May 12).
35. Digital free images home page. <https://www.freepik.com/macrovector> (accessed May 12).
36. Wan, C.; Bowen, C. R., Multiscale-structuring of polyvinylidene fluoride for energy harvesting: the impact of molecular-, micro-and macro-structure. *J. Mater. Chem. A* **2017**, 5 (7), 3091-3128.
37. Jiang, B.; Iocozzia, J.; Zhao, L.; Zhang, H.; Harn, Y.-W.; Chen, Y.; Lin, Z., Barium titanate at the nanoscale: controlled synthesis and dielectric and ferroelectric properties. *Chem. Soc. Rev.* **2019**, 48 (4), 1194-1228.
38. Sundaram, S.; Kellnhofer, P.; Li, Y.; Zhu, J.-Y.; Torralba, A.; Matusik, W., Learning the signatures of the human grasp using a scalable tactile glove. *Nature* **2019**, 569 (7758), 698-702.
39. Webb, R. C.; Bonifas, A. P.; Behnaz, A.; Zhang, Y.; Yu, K. J.; Cheng, H.; Shi, M.; Bian, Z.; Liu, Z.; Kim, Y.-S., Ultrathin conformal devices for precise and continuous thermal characterization of human skin. *Nat. Mater.* **2013**, 12 (10), 938-944.
40. Bae, G. Y.; Han, J. T.; Lee, G.; Lee, S.; Kim, S. W.; Park, S.; Kwon, J.; Jung, S.; Cho, K., Pressure/temperature sensing bimodal electronic skin with stimulus discriminability and linear sensitivity. *Adv. Mater.* **2018**, 30 (43), 1803388.
41. Wang, S.; Xu, J.; Wang, W.; Wang, G.-J. N.; Rastak, R.; Molina-Lopez, F.; Chung, J. W.; Niu, S.; Feig, V. R.; Lopez, J., Skin electronics from scalable fabrication of an intrinsically stretchable transistor array. *Nature* **2018**, 555 (7694), 83-88.
42. Wang, C.; Li, X.; Hu, H.; Zhang, L.; Huang, Z.; Lin, M.; Zhang, Z.; Yin, Z.; Huang, B.; Gong,

- H., Monitoring of the central blood pressure waveform via a conformal ultrasonic device. *Nat. Biomed. Eng.* **2018**, 2 (9), 687.
43. Zhu, C.; Chortos, A.; Wang, Y.; Pfattner, R.; Lei, T.; Hinckley, A. C.; Pochorovski, I.; Yan, X.; To, J. W.-F.; Oh, J. Y., Stretchable temperature-sensing circuits with strain suppression based on carbon nanotube transistors. *Nat. Electron.* **2018**, 1 (3), 183-190.
 44. Shin, J.; Jeong, B.; Kim, J.; Nam, V. B.; Yoon, Y.; Jung, J.; Hong, S.; Lee, H.; Eom, H.; Yeo, J., Sensitive Wearable Temperature Sensor with Seamless Monolithic Integration. *Adv. Mater.* **2019**, 1905527.
 45. Liu, M.; Pu, X.; Jiang, C.; Liu, T.; Huang, X.; Chen, L.; Du, C.; Sun, J.; Hu, W.; Wang, Z. L., Large-area all-textile pressure sensors for monitoring human motion and physiological signals. *Adv. Mater.* **2017**, 29 (41), 1703700.
 46. Jin, H.; Matsuhisa, N.; Lee, S.; Abbas, M.; Yokota, T.; Someya, T., Enhancing the Performance of Stretchable Conductors for E-Textiles by Controlled Ink Permeation. *Adv. Mater.* **2017**, 29 (21), 1605848.
 47. Liu, L.; Pan, J.; Chen, P.; Zhang, J.; Yu, X.; Ding, X.; Wang, B.; Sun, X.; Peng, H., A triboelectric textile templated by a three-dimensionally penetrated fabric. *J. Mater. Chem. A* **2016**, 4 (16), 6077-6083.
 48. Dong, K.; Deng, J.; Zi, Y.; Wang, Y. C.; Xu, C.; Zou, H.; Ding, W.; Dai, Y.; Gu, B.; Sun, B., 3D orthogonal woven triboelectric nanogenerator for effective biomechanical energy harvesting and as self-powered active motion sensors. *Adv. Mater.* **2017**, 29 (38), 1702648.
 49. Chen, J.; Guo, H.; Pu, X.; Wang, X.; Xi, Y.; Hu, C., Traditional weaving craft for one-piece self-charging power textile for wearable electronics. *Nano Energy* **2018**, 50, 536-543.
 50. Kim, K. N.; Chun, J.; Kim, J. W.; Lee, K. Y.; Park, J.-U.; Kim, S.-W.; Wang, Z. L.; Baik, J. M., Highly stretchable 2D fabrics for wearable triboelectric nanogenerator under harsh environments. *ACS Nano* **2015**, 9 (6), 6394-6400.
 51. Sim, H. J.; Choi, C.; Kim, S. H.; Kim, K. M.; Lee, C. J.; Kim, Y. T.; Lepró, X.; Baughman, R. H.; Kim, S. J., Stretchable triboelectric fiber for self-powered kinematic sensing textile. *Sci. Rep.* **2016**, 6 (1), 1-7.
 52. Dong, K.; Wang, Y.-C.; Deng, J.; Dai, Y.; Zhang, S. L.; Zou, H.; Gu, B.; Sun, B.; Wang, Z. L., A highly stretchable and washable all-yarn-based self-charging knitting power textile composed of fiber triboelectric nanogenerators and supercapacitors. *ACS Nano* **2017**, 11 (9), 9490-9499.
 53. Kwak, S. S.; Kim, H.; Seung, W.; Kim, J.; Hinchet, R.; Kim, S.-W., Fully stretchable textile triboelectric nanogenerator with knitted fabric structures. *ACS Nano* **2017**, 11 (11), 10733-10741.

54. Gibney, E., The inside story on wearable electronics. *Nature* **2015**, 528 (7580), 26-28.
55. Kaltenbrunner, M.; Sekitani, T.; Reeder, J.; Yokota, T.; Kuribara, K.; Tokuhara, T.; Drack, M.; Schwödiauer, R.; Graz, I.; Bauer-Gogonea, S., An ultra-lightweight design for imperceptible plastic electronics. *Nature* **2013**, 499 (7459), 458-463.
56. Schwartz, G.; Tee, B. C.-K.; Mei, J.; Appleton, A. L.; Kim, D. H.; Wang, H.; Bao, Z., Flexible polymer transistors with high pressure sensitivity for application in electronic skin and health monitoring. *Nat. Commun.* **2013**, 4 (1), 1-8.
57. Zheng, Q.; Shi, B.; Fan, F.; Wang, X.; Yan, L.; Yuan, W.; Wang, S.; Liu, H.; Li, Z.; Wang, Z. L., In vivo powering of pacemaker by breathing-driven implanted triboelectric nanogenerator. *Adv. Mater.* **2014**, 26 (33), 5851-5856.
58. Wu, C.; Wang, A. C.; Ding, W.; Guo, H.; Wang, Z. L., Triboelectric nanogenerator: a foundation of the energy for the new era. *Adv. Energy Mater.* **2019**, 9 (1), 1802906.
59. Niu, S.; Wang, Z. L., Theoretical systems of triboelectric nanogenerators. *Nano Energy* **2015**, 14, 161-192.
60. Niu, S.; Wang, S.; Lin, L.; Liu, Y.; Zhou, Y. S.; Hu, Y.; Wang, Z. L., Theoretical study of contact-mode triboelectric nanogenerators as an effective power source. *Energy Environ. Sci.* **2013**, 6 (12), 3576-3583.
61. Kim, S.; Ha, J.; Kim, J.-B., Theoretical study on the dielectric effect on triboelectric nanogenerators. *Integr. Ferroelectr.* **2016**, 176 (1), 283-290.
62. Seung, W.; Yoon, H. J.; Kim, T. Y.; Ryu, H.; Kim, J.; Lee, J. H.; Lee, J. H.; Kim, S.; Park, Y. K.; Park, Y. J., Boosting power-generating performance of triboelectric nanogenerators via artificial control of ferroelectric polarization and dielectric properties. *Adv. Energy Mater.* **2017**, 7 (2), 1600988.
63. Chen, L.; Shi, Q.; Sun, Y.; Nguyen, T.; Lee, C.; Soh, S., Controlling surface charge generated by contact electrification: Strategies and applications. *Adv. Mater.* **2018**, 30 (47), 1802405.
64. Ryu, H.; Lee, J. H.; Kim, T. Y.; Khan, U.; Lee, J. H.; Kwak, S. S.; Yoon, H. J.; Kim, S. W., High-performance triboelectric nanogenerators based on solid polymer electrolytes with asymmetric pairing of ions. *Adv. Energy Mater.* **2017**, 7 (17), 1700289.
65. Yu, Y.; Li, Z.; Wang, Y.; Gong, S.; Wang, X., Sequential infiltration synthesis of doped polymer films with tunable electrical properties for efficient triboelectric nanogenerator development. *Adv. Mater.* **2015**, 27 (33), 4938-4944.
66. Zhang, X.; Huang, X.; Kwok, S. W.; Soh, S., Designing non-charging surfaces from non-conductive polymers. *Adv. Mater.* **2016**, 28 (15), 3024-3029.
67. Lee, J. W.; Cho, H. J.; Chun, J.; Kim, K. N.; Kim, S.; Ahn, C. W.; Kim, I. W.; Kim, J.-Y.; Kim, S.-W.; Yang, C., Robust nanogenerators based on graft copolymers via control of dielectrics

- for remarkable output power enhancement. *Sci. Adv.* **2017**, 3 (5), e1602902.
68. Shin, S.-H.; Bae, Y. E.; Moon, H. K.; Kim, J.; Choi, S.-H.; Kim, Y.; Yoon, H. J.; Lee, M. H.; Nah, J., Formation of triboelectric series via atomic-level surface functionalization for triboelectric energy harvesting. *ACS Nano* **2017**, 11 (6), 6131-6138.
 69. Wang, S.; Zi, Y.; Zhou, Y. S.; Li, S.; Fan, F.; Lin, L.; Wang, Z. L., Molecular surface functionalization to enhance the power output of triboelectric nanogenerators. *J. Mater. Chem. A* **2016**, 4 (10), 3728-3734.
 70. Shin, S.-H.; Kwon, Y. H.; Kim, Y.-H.; Jung, J.-Y.; Lee, M. H.; Nah, J., Triboelectric charging sequence induced by surface functionalization as a method to fabricate high performance triboelectric generators. *ACS Nano* **2015**, 9 (4), 4621-4627.
 71. Kim, M. P.; Lee, Y.; Hur, Y. H.; Park, J.; Kim, J.; Lee, Y.; Ahn, C. W.; Song, S. W.; Jung, Y. S.; Ko, H., Molecular structure engineering of dielectric fluorinated polymers for enhanced performances of triboelectric nanogenerators. *Nano Energy* **2018**, 53, 37-45.
 72. Fan, F.-R.; Lin, L.; Zhu, G.; Wu, W.; Zhang, R.; Wang, Z. L., Transparent triboelectric nanogenerators and self-powered pressure sensors based on micropatterned plastic films. *Nano Lett.* **2012**, 12 (6), 3109-3114.
 73. Seol, M. L.; Woo, J. H.; Lee, D. I.; Im, H.; Hur, J.; Choi, Y. K., Nature-replicated nano-in-micro structures for triboelectric energy harvesting. *Small* **2014**, 10 (19), 3887-3894.
 74. Bae, J.; Lee, J.; Kim, S.; Ha, J.; Lee, B.-S.; Park, Y.; Choong, C.; Kim, J.-B.; Wang, Z. L.; Kim, H.-Y., Flutter-driven triboelectrification for harvesting wind energy. *Nat. Commun.* **2014**, 5 (1), 1-9.
 75. Ha, M.; Lim, S.; Cho, S.; Lee, Y.; Na, S.; Baig, C.; Ko, H., Skin-inspired hierarchical polymer architectures with gradient stiffness for spacer-free, ultrathin, and highly sensitive triboelectric sensors. *ACS Nano* **2018**, 12 (4), 3964-3974.
 76. Lee, K. Y.; Chun, J.; Lee, J. H.; Kim, K. N.; Kang, N. R.; Kim, J. Y.; Kim, M. H.; Shin, K. S.; Gupta, M. K.; Baik, J. M., Hydrophobic sponge structure-based triboelectric nanogenerator. *Adv. Mater.* **2014**, 26 (29), 5037-5042.
 77. Stadlober, B.; Zirkel, M.; Irimia-Vladu, M., Route towards sustainable smart sensors: ferroelectric polyvinylidene fluoride-based materials and their integration in flexible electronics. *Chem. Soc. Rev.* **2019**, 48 (6), 1787-1825.
 78. Bowen, C. R.; Taylor, J.; LeBoulbar, E.; Zabek, D.; Chauhan, A.; Vaish, R., Pyroelectric materials and devices for energy harvesting applications. *Energy Environ. Sci.* **2014**, 7 (12), 3836-3856.
 79. Ryu, H.; Kim, S. W., Emerging Pyroelectric Nanogenerators to Convert Thermal Energy into Electrical Energy. *Small* **2019**, 1903469.

80. Ge, Z.-H.; Zhao, L.-D.; Wu, D.; Liu, X.; Zhang, B.-P.; Li, J.-F.; He, J., Low-cost, abundant binary sulfides as promising thermoelectric materials. *Mater. Today* **2016**, *19* (4), 227-239.
81. Snyder, G. J.; Snyder, A. H., Figure of merit ZT of a thermoelectric device defined from materials properties. *Energy Environ. Sci.* **2017**, *10* (11), 2280-2283.
82. Lines, M. E.; Glass, A. M., *Principles and applications of ferroelectrics and related materials*. Oxford university press: 2001.
83. Ruan, L.; Yao, X.; Chang, Y.; Zhou, L.; Qin, G.; Zhang, X., Properties and Applications of the β Phase Poly (vinylidene fluoride). *Polymers* **2018**, *10* (3), 228.
84. Furukawa, T., Structure and functional properties of ferroelectric polymers. *Adv. Colloid Interface Sci.* **1997**, *71*, 183-208.
85. Ribeiro, C.; Costa, C. M.; Correia, D. M.; Nunes-Pereira, J.; Oliveira, J.; Martins, P.; Goncalves, R.; Cardoso, V. F.; Lanceros-Mendez, S., Electroactive poly (vinylidene fluoride)-based structures for advanced applications. *Nat. Protoc.* **2018**, *13* (4), 681.
86. Su, R.; Tseng, J.-K.; Lu, M.-S.; Lin, M.; Fu, Q.; Zhu, L., Ferroelectric behavior in the high temperature paraelectric phase in a poly (vinylidene fluoride-co-trifluoroethylene) random copolymer. *Polymer* **2012**, *53* (3), 728-739.
87. Martins, P.; Lopes, A.; Lanceros-Mendez, S., Electroactive phases of poly (vinylidene fluoride): Determination, processing and applications. *Prog. Polym. Sci.* **2014**, *39* (4), 683-706.
88. Shepelin, N. A.; Glushenkov, A. M.; Lussini, V. C.; Fox, P. J.; Dicinoski, G. W.; Shapter, J. G.; Ellis, A. V., New developments in composites, copolymer technologies and processing techniques for flexible fluoropolymer piezoelectric generators for efficient energy harvesting. *Energy Environ. Sci.* **2019**, *12* (4), 1143-1176.
89. Shin, S.-H.; Kim, Y.-H.; Lee, M. H.; Jung, J.-Y.; Nah, J., Hemispherically aggregated BaTiO₃ nanoparticle composite thin film for high-performance flexible piezoelectric nanogenerator. *ACS Nano* **2014**, *8* (3), 2766-2773.
90. Zhao, Y.; Liao, Q.; Zhang, G.; Zhang, Z.; Liang, Q.; Liao, X.; Zhang, Y., High output piezoelectric nanocomposite generators composed of oriented BaTiO₃ NPs@ PVDF. *Nano Energy* **2015**, *11*, 719-727.
91. Alam, M. M.; Sultana, A.; Sarkar, D.; Mandal, D., Electroactive β -crystalline phase inclusion and photoluminescence response of a heat-controlled spin-coated PVDF/TiO₂ free-standing nanocomposite film for a nanogenerator and an active nanosensor. *Nanotechnology* **2017**, *28* (36), 365401.
92. Park, J.; Kim, M.; Lee, Y.; Lee, H. S.; Ko, H., Fingertip skin-inspired microstructured ferroelectric skins discriminate static/dynamic pressure and temperature stimuli. *Sci. Adv.*

- 2015**, *I* (9), e1500661.
93. Lee, J. H.; Yoon, H. J.; Kim, T. Y.; Gupta, M. K.; Lee, J. H.; Seung, W.; Ryu, H.; Kim, S. W., Micropatterned P (VDF-TrFE) film-based piezoelectric nanogenerators for highly sensitive self-powered pressure sensors. *Adv. Funct. Mater.* **2015**, *25* (21), 3203-3209.
 94. Hansen, B. J.; Liu, Y.; Yang, R.; Wang, Z. L., Hybrid nanogenerator for concurrently harvesting biomechanical and biochemical energy. *ACS Nano* **2010**, *4* (7), 3647-3652.
 95. Lu, X.; Qu, H.; Skorobogatiy, M., Piezoelectric microstructured fibers via drawing of multimaterial preforms. *Sci. Rep.* **2017**, *7* (1), 1-12.
 96. Persano, L.; Dagdeviren, C.; Su, Y.; Zhang, Y.; Girardo, S.; Pisignano, D.; Huang, Y.; Rogers, J. A., High performance piezoelectric devices based on aligned arrays of nanofibers of poly (vinylidene fluoride-co-trifluoroethylene). *Nat. Commun.* **2013**, *4* (1), 1-10.
 97. Soin, N.; Shah, T. H.; Anand, S. C.; Geng, J.; Pornwannachai, W.; Mandal, P.; Reid, D.; Sharma, S.; Hadimani, R. L.; Bayramol, D. V., Novel “3-D spacer” all fibre piezoelectric textiles for energy harvesting applications. *Energy Environ. Sci.* **2014**, *7* (5), 1670-1679.
 98. Fang, K.; Fang, F.; Wang, S.; Yang, W.; Sun, W.; Li, J., Hybridizing CNT/PMMA/PVDF towards high-performance piezoelectric nanofibers. *J. Phys. D: Appl. Phys.* **2018**, *51* (26), 265305.
 99. Ke, K.; Pötschke, P.; Jehnichen, D.; Fischer, D.; Voit, B., Achieving β -phase poly (vinylidene fluoride) from melt cooling: Effect of surface functionalized carbon nanotubes. *Polymer* **2014**, *55* (2), 611-619.
 100. Chang, C.; Tran, V. H.; Wang, J.; Fuh, Y.-K.; Lin, L., Direct-write piezoelectric polymeric nanogenerator with high energy conversion efficiency. *Nano Lett.* **2010**, *10* (2), 726-731.
 101. Whatmore, R., Pyroelectric devices and materials. *Rep. Prog. Phys.* **1986**, *49* (12), 1335.
 102. Erhart, J., Experiments to demonstrate piezoelectric and pyroelectric effects. *Phys. Educ.* **2013**, *48* (4), 438.
 103. Lang, S. B.; Muensit, S., Review of some lesser-known applications of piezoelectric and pyroelectric polymers. *Appl. Phys. A* **2006**, *85* (2), 125-134.
 104. Zabek, D.; Taylor, J.; Boulbar, E. L.; Bowen, C. R., Micropatterning of flexible and free standing polyvinylidene difluoride (PVDF) films for enhanced pyroelectric energy transformation. *Adv. Energy Mater.* **2015**, *5* (8), 1401891.
 105. Zabek, D.; Seunarine, K.; Spacie, C.; Bowen, C., Graphene ink laminate structures on poly (vinylidene difluoride)(pvdf) for pyroelectric thermal energy harvesting and waste heat recovery. *ACS Appl. Mater. Interfaces* **2017**, *9* (10), 9161-9167.
 106. Zhao, T.; Jiang, W.; Liu, H.; Niu, D.; Li, X.; Liu, W.; Li, X.; Chen, B.; Shi, Y.; Yin, L., An infrared-driven flexible pyroelectric generator for non-contact energy harvester. *Nanoscale*

- 2016**, 8 (15), 8111-8117.
107. Ghosh, S. K.; Xie, M.; Bowen, C. R.; Davies, P. R.; Morgan, D. J.; Mandal, D., A hybrid strain and thermal energy harvester based on an infra-red sensitive Er ³⁺ modified poly (vinylidene fluoride) ferroelectret structure. *Sci. Rep.* **2017**, 7 (1), 1-13.
 108. Lee, J. H.; Lee, K. Y.; Gupta, M. K.; Kim, T. Y.; Lee, D. Y.; Oh, J.; Ryu, C.; Yoo, W. J.; Kang, C. Y.; Yoon, S. J., Highly stretchable piezoelectric-pyroelectric hybrid nanogenerator. *Adv. Mater.* **2014**, 26 (5), 765-769.
 109. Gan, W.; Majid, W. A., Effect of TiO₂ on enhanced pyroelectric activity of PVDF composite. *Smart Mater. Struct.* **2014**, 23 (4), 045026.
 110. Mokhtari, F.; Latifi, M.; Shamshirsaz, M., Electrospinning/electrospray of polyvinylidene fluoride (PVDF): piezoelectric nanofibers. *J. Text. Inst.* **2016**, 107 (8), 1037-1055.
 111. Kim, J.; Lee, J. H.; Ryu, H.; Lee, J. H.; Khan, U.; Kim, H.; Kwak, S. S.; Kim, S. W., High-Performance Piezoelectric, Pyroelectric, and Triboelectric Nanogenerators Based on P (VDF-TrFE) with Controlled Crystallinity and Dipole Alignment. *Adv. Funct. Mater.* **2017**, 27 (22), 1700702.
 112. Qin, Z.; Yin, Y.; Zhang, W.; Li, C.; Pan, K., Wearable and stretchable triboelectric nanogenerator based on crumpled nanofibrous membranes. *ACS Appl. Mater. Interfaces* **2019**, 11 (13), 12452-12459.
 113. Kim, M.; Park, D.; Alam, M. M.; Lee, S.; Park, P.; Nah, J., Remarkable output power density enhancement of triboelectric nanogenerators via polarized ferroelectric polymers and bulk MoS₂ composites. *ACS Nano* **2019**, 13 (4), 4640-4646.
 114. Bai, P.; Zhu, G.; Zhou, Y. S.; Wang, S.; Ma, J.; Zhang, G.; Wang, Z. L., Dipole-moment-induced effect on contact electrification for triboelectric nanogenerators. *Nano Res.* **2014**, 7 (7), 990-997.
 115. Lee, J. H.; Hinchet, R.; Kim, T. Y.; Ryu, H.; Seung, W.; Yoon, H. J.; Kim, S. W., Control of skin potential by triboelectrification with ferroelectric polymers. *Adv. Mater.* **2015**, 27 (37), 5553-5558.
 116. Lee, K. Y.; Kim, S. K.; Lee, J. H.; Seol, D.; Gupta, M. K.; Kim, Y.; Kim, S. W., Controllable charge transfer by ferroelectric polarization mediated triboelectricity. *Adv. Funct. Mater.* **2016**, 26 (18), 3067-3073.
 117. Šutka, A.; Mālnieks, K.; Linarts, A.; Timusk, M.; Jurkāns, V.; Gorņevs, I.; Blūms, J.; Bērziņa, A.; Joost, U.; Knite, M., Inversely polarised ferroelectric polymer contact electrodes for triboelectric-like generators from identical materials. *Energy Environ. Sci.* **2018**, 11 (6), 1437-1443.
 118. OMNEXUS home page. <https://omnexus.specialchem.com/selection-guide/polyvinylidene->

- fluoride-pvdf-plastic (accessed May 12).
119. Yokota, T.; Zalar, P.; Kaltenbrunner, M.; Jinno, H.; Matsuhisa, N.; Kitanosako, H.; Tachibana, Y.; Yukita, W.; Koizumi, M.; Someya, T., Ultraflexible organic photonic skin. *Sci. Adv.* **2016**, 2 (4), e1501856.
 120. Gao, L.; Zhang, Y.; Malyarchuk, V.; Jia, L.; Jang, K.-I.; Webb, R. C.; Fu, H.; Shi, Y.; Zhou, G.; Shi, L., Epidermal photonic devices for quantitative imaging of temperature and thermal transport characteristics of the skin. *Nat. Commun.* **2014**, 5 (1), 1-10.
 121. Kim, E. H.; Cho, S. H.; Lee, J. H.; Jeong, B.; Kim, R. H.; Yu, S.; Lee, T.-W.; Shim, W.; Park, C., Organic light emitting board for dynamic interactive display. *Nat. Commun.* **2017**, 8 (1), 1-8.
 122. Kang, S.; Cho, S.; Shanker, R.; Lee, H.; Park, J.; Um, D.-S.; Lee, Y.; Ko, H., Transparent and conductive nanomembranes with orthogonal silver nanowire arrays for skin-attachable loudspeakers and microphones. *Sci. Adv.* **2018**, 4 (8), eaas8772.
 123. Morin, S. A.; Shepherd, R. F.; Kwok, S. W.; Stokes, A. A.; Nemiroski, A.; Whitesides, G. M., Camouflage and display for soft machines. *Science* **2012**, 337 (6096), 828-832.
 124. Lee, Y.; Park, J.; Choe, A.; Cho, S.; Kim, J.; Ko, H., Mimicking Human and Biological Skins for Multifunctional Skin Electronics. *Adv. Funct. Mater.* **2019**, 1904523.
 125. Lee, Y.; Park, J.; Cho, S.; Shin, Y.-E.; Lee, H.; Kim, J.; Myoung, J.; Cho, S.; Kang, S.; Baig, C., Flexible ferroelectric sensors with ultrahigh pressure sensitivity and linear response over exceptionally broad pressure range. *ACS Nano* **2018**, 12 (4), 4045-4054.
 126. Kim, T.-H.; Lee, C.-S.; Kim, S.; Hur, J.; Lee, S.; Shin, K. W.; Yoon, Y.-Z.; Choi, M. K.; Yang, J.; Kim, D.-H., Fully stretchable optoelectronic sensors based on colloidal quantum dots for sensing photoplethysmographic signals. *ACS Nano* **2017**, 11 (6), 5992-6003.
 127. Razak, A.; Hadi, A.; Zayegh, A.; Begg, R. K.; Wahab, Y., Foot plantar pressure measurement system: A review. *Sensors* **2012**, 12 (7), 9884-9912.
 128. Uswatte, G.; Giuliani, C.; Winstein, C.; Zeringue, A.; Hobbs, L.; Wolf, S. L., Validity of accelerometry for monitoring real-world arm activity in patients with subacute stroke: evidence from the extremity constraint-induced therapy evaluation trial. *Arch. Phys. Med. Rehabil.*, **2006**, 87 (10), 1340-1345.
 129. Patel, S.; Park, H.; Bonato, P.; Chan, L.; Rodgers, M., A review of wearable sensors and systems with application in rehabilitation. *J. Neuroeng. Rehabil.* **2012**, 9 (1), 21.
 130. Jain, A. K.; Ross, A.; Prabhakar, S., An introduction to biometric recognition. *IEEE Trans. Circ. Syst. Video Technol.* **2004**, 14 (1), 4-20.
 131. Yang, J.; Chen, J.; Su, Y.; Jing, Q.; Li, Z.; Yi, F.; Wen, X.; Wang, Z.; Wang, Z. L., Eardrum-Inspired active sensors for self-powered cardiovascular system characterization and throat-

- attached anti-Interference voice recognition. *Adv. Mater.* **2015**, 27 (8), 1316-1326.
132. Lee, S.; Kim, J.; Yun, I.; Bae, G. Y.; Kim, D.; Park, S.; Yi, I.-M.; Moon, W.; Chung, Y.; Cho, K., An ultrathin conformable vibration-responsive electronic skin for quantitative vocal recognition. *Nat. Commun.* **2019**, 10 (1), 1-11.
 133. An, B. W.; Heo, S.; Ji, S.; Bien, F.; Park, J.-U., Transparent and flexible fingerprint sensor array with multiplexed detection of tactile pressure and skin temperature. *Nat. Commun.* **2018**, 9 (1), 1-10.
 134. Busselaar, E., Improved pores detection in fingerprints by applying ring led's (525 nm) *Opt. Appl.* **2010**, 40, 843-861.
 135. Tordera, D.; Peeters, B.; Akkerman, H. B.; van Breemen, A. J.; Maas, J.; Shanmugam, S.; Kronemeijer, A. J.; Gelinck, G. H., A High-Resolution Thin-Film Fingerprint Sensor Using a Printed Organic Photodetector. *Adv. Mater. Technol.* **2019**, 4 (11), 1900651.
 136. Castano, L. M.; Flatau, A. B., Smart fabric sensors and e-textile technologies: a review. *Smart Mater. Struct.* **2014**, 23 (5), 053001.
 137. Gong, W.; Hou, C.; Guo, Y.; Zhou, J.; Mu, J.; Li, Y.; Zhang, Q.; Wang, H., A wearable, fibroid, self-powered active kinematic sensor based on stretchable sheath-core structural triboelectric fibers. *Nano Energy* **2017**, 39, 673-683.
 138. Zhao, Z.; Yan, C.; Liu, Z.; Fu, X.; Peng, L. M.; Hu, Y.; Zheng, Z., Machine-washable textile triboelectric nanogenerators for effective human respiratory monitoring through loom weaving of metallic yarns. *Adv. Mater.* **2016**, 28 (46), 10267-10274.
 139. Zhu, M.; Huang, Y.; Ng, W. S.; Liu, J.; Wang, Z.; Wang, Z.; Hu, H.; Zhi, C., 3D spacer fabric based multifunctional triboelectric nanogenerator with great feasibility for mechanized large-scale production. *Nano Energy* **2016**, 27, 439-446.
 140. Zi, Y.; Lin, L.; Wang, J.; Wang, S.; Chen, J.; Fan, X.; Yang, P. K.; Yi, F.; Wang, Z. L., Triboelectric-pyroelectric-piezoelectric hybrid cell for high-efficiency energy-harvesting and self-powered sensing. *Adv. Mater.* **2015**, 27 (14), 2340-2347.
 141. Zhao, S.; Zhu, R., Electronic skin with multifunction sensors based on thermosensation. *Adv. Mater.* **2017**, 29 (15), 1606151.
 142. Zhang, Q.; Liang, Q.; Zhang, Z.; Kang, Z.; Liao, Q.; Ding, Y.; Ma, M.; Gao, F.; Zhao, X.; Zhang, Y., Electromagnetic shielding hybrid nanogenerator for health monitoring and protection. *Adv. Funct. Mater.* **2018**, 28 (1), 1703801.
 143. Ho, D. H.; Sun, Q.; Kim, S. Y.; Han, J. T.; Kim, D. H.; Cho, J. H., Stretchable and multimodal all graphene electronic skin. *Adv. Mater.* **2016**, 28 (13), 2601-2608.
 144. Chun, S.; Son, W.; Choi, C.; Min, H.; Kim, J.; Lee, H. J.; Kim, D.; Kim, C.; Koh, J.-s.; Pang, C., Bioinspired hairy skin electronics for detecting the direction and incident angle of airflow.

- ACS Appl. Mater. Interfaces* **2019**, *11* (14), 13608-13615.
145. Song, K.; Zhao, R.; Wang, Z. L.; Yang, Y., Conjoined Pyro-Piezoelectric Effect for Self-Powered Simultaneous Temperature and Pressure Sensing. *Adv. Mater.* **2019**, *31* (36), 1902831.
 146. Lai, M.; Cheng, L.; Xi, Y.; Wu, Y.; Hu, C.; Guo, H.; Du, B.; Liu, G.; Liu, Q.; Liu, R., Enhancing the performance of NaNbO₃ triboelectric nanogenerators by dielectric modulation and electronegative modification. *J. Phys. D: Appl. Phys.* **2017**, *51* (1), 015303.
 147. Chen, J.; Guo, H.; He, X.; Liu, G.; Xi, Y.; Shi, H.; Hu, C., Enhancing performance of triboelectric nanogenerator by filling high dielectric nanoparticles into sponge PDMS film. *ACS Appl. Mater. Interfaces* **2016**, *8* (1), 736-744.
 148. Park, K. I.; Lee, M.; Liu, Y.; Moon, S.; Hwang, G. T.; Zhu, G.; Kim, J. E.; Kim, S. O.; Kim, D. K.; Wang, Z. L., Flexible nanocomposite generator made of BaTiO₃ nanoparticles and graphitic carbons. *Adv. Mater.* **2012**, *24* (22), 2999-3004.
 149. Park, H.-W.; Huynh, N. D.; Kim, W.; Hwang, H. J.; Hong, H.; Choi, K.; Song, A.; Chung, K.-B.; Choi, D., Effects of Embedded TiO₂-x Nanoparticles on Triboelectric Nanogenerator Performance. *Micromachines* **2018**, *9* (8), 407.
 150. Gao, X.; Zheng, M.; Yan, X.; Fu, J.; Zhu, M.; Hou, Y., The alignment of BCZT particles in PDMS boosts the sensitivity and cycling reliability of a flexible piezoelectric touch sensor. *J. Mater. Chem. C* **2019**, *7* (4), 961-967.
 151. Shin, Y.-E.; Lee, J.-E.; Park, Y.; Hwang, S.-H.; Chae, H. G.; Ko, H., Sewing machine stitching of polyvinylidene fluoride fibers: programmable textile patterns for wearable triboelectric sensors. *J. Mater. Chem. A* **2018**, *6* (45), 22879-22888.
 152. Shin, Y.-E.; Sohn, S.-D.; Han, H.; Park, Y.; Shin, H.-J.; Ko, H., Self-Powered Triboelectric/Pyroelectric Multimodal Sensors with Enhanced Performances via Ferroelectric Polarization. *Nano Energy* **2020**, 104671.
 153. Wang, C.; Li, X.; Gao, E.; Jian, M.; Xia, K.; Wang, Q.; Xu, Z.; Ren, T.; Zhang, Y., Carbonized silk fabric for ultrastretchable, highly sensitive, and wearable strain sensors. *Adv. Mater.* **2016**, *28* (31), 6640-6648.
 154. Lee, J.; Kwon, H.; Seo, J.; Shin, S.; Koo, J. H.; Pang, C.; Son, S.; Kim, J. H.; Jang, Y. H.; Kim, D. E., Conductive fiber-based ultrasensitive textile pressure sensor for wearable electronics. *Adv. Mater.* **2015**, *27* (15), 2433-2439.
 155. Hamedi, M.; Forchheimer, R.; Inganäs, O., Towards woven logic from organic electronic fibres. *Nat. Mater.* **2007**, *6* (5), 357-362.
 156. Kim, H. M.; Kang, H. W.; Hwang, D. K.; Lim, H. S.; Ju, B. K.; Lim, J. A., Metal-Insulator-Semiconductor Coaxial Microfibers Based on Self-Organization of Organic Semiconductor:

- Polymer Blend for Weavable, Fibriform Organic Field-Effect Transistors. *Adv. Funct. Mater.* **2016**, *26* (16), 2706-2714.
157. Le, V. T.; Kim, H.; Ghosh, A.; Kim, J.; Chang, J.; Vu, Q. A.; Pham, D. T.; Lee, J.-H.; Kim, S.-W.; Lee, Y. H., Coaxial fiber supercapacitor using all-carbon material electrodes. *ACS Nano* **2013**, *7* (7), 5940-5947.
 158. Sun, H.; Xie, S.; Li, Y.; Jiang, Y.; Sun, X.; Wang, B.; Peng, H., Large-Area Supercapacitor Textiles with Novel Hierarchical Conducting Structures. *Adv. Mater.* **2016**, *28* (38), 8431-8438.
 159. Weng, W.; Chen, P.; He, S.; Sun, X.; Peng, H., Smart electronic textiles. *Angew. Chem. Int. Ed.* **2016**, *55* (21), 6140-6169.
 160. Heo, J. S.; Eom, J.; Kim, Y. H.; Park, S. K., Recent progress of textile-based wearable electronics: a comprehensive review of materials, devices, and applications. *Small* **2018**, *14* (3), 1703034.
 161. Zeng, W.; Shu, L.; Li, Q.; Chen, S.; Wang, F.; Tao, X. M., Fiber-based wearable electronics: a review of materials, fabrication, devices, and applications. *Adv. Mater.* **2014**, *26* (31), 5310-5336.
 162. Ahn, Y.; Song, S.; Yun, K.-S., Woven flexible textile structure for wearable power-generating tactile sensor array. *Smart Mater. Struct.* **2015**, *24* (7), 075002.
 163. Park, J. J.; Hyun, W. J.; Mun, S. C.; Park, Y. T.; Park, O. O., Highly stretchable and wearable graphene strain sensors with controllable sensitivity for human motion monitoring. *ACS Appl. Mater. Interfaces* **2015**, *7* (11), 6317-6324.
 164. Zhong, J.; Zhang, Y.; Zhong, Q.; Hu, Q.; Hu, B.; Wang, Z. L.; Zhou, J., Fiber-based generator for wearable electronics and mobile medication. *ACS Nano* **2014**, *8* (6), 6273-6280.
 165. Pu, X.; Song, W.; Liu, M.; Sun, C.; Du, C.; Jiang, C.; Huang, X.; Zou, D.; Hu, W.; Wang, Z. L., Wearable power-textiles by integrating fabric triboelectric nanogenerators and fiber-shaped dye-sensitized solar cells. *Adv. Energy Mater.* **2016**, *6* (20), 1601048.
 166. Cheng, Y.; Lu, X.; Chan, K. H.; Wang, R.; Cao, Z.; Sun, J.; Ho, G. W., A stretchable fiber nanogenerator for versatile mechanical energy harvesting and self-powered full-range personal healthcare monitoring. *Nano Energy* **2017**, *41*, 511-518.
 167. Pu, X.; Li, L.; Liu, M.; Jiang, C.; Du, C.; Zhao, Z.; Hu, W.; Wang, Z. L., Wearable self-charging power textile based on flexible yarn supercapacitors and fabric nanogenerators. *Adv. Mater.* **2016**, *28* (1), 98-105.
 168. Guo, H.; Pu, X.; Chen, J.; Meng, Y.; Yeh, M.-H.; Liu, G.; Tang, Q.; Chen, B.; Liu, D.; Qi, S., A highly sensitive, self-powered triboelectric auditory sensor for social robotics and hearing aids. *Sci. Robot.* **2018**, *3* (20), eaat2516.

169. Pu, X.; Guo, H.; Chen, J.; Wang, X.; Xi, Y.; Hu, C.; Wang, Z. L., Eye motion triggered self-powered mechnosensational communication system using triboelectric nanogenerator. *Sci. Adv.* **2017**, *3* (7), e1700694.
170. Wang, S.; Lin, L.; Wang, Z. L., Triboelectric nanogenerators as self-powered active sensors. *Nano Energy* **2015**, *11*, 436-462.
171. Lin, L.; Xie, Y.; Wang, S.; Wu, W.; Niu, S.; Wen, X.; Wang, Z. L., Triboelectric active sensor array for self-powered static and dynamic pressure detection and tactile imaging. *ACS Nano* **2013**, *7* (9), 8266-8274.
172. Fan, F.-R.; Tian, Z.-Q.; Wang, Z. L., Flexible triboelectric generator. *Nano Energy* **2012**, *1* (2), 328-334.
173. Liu, X.; Lillehoj, P. B., Embroidered electrochemical sensors for biomolecular detection. *Lab on a Chip* **2016**, *16* (11), 2093-2098.
174. Post, E. R.; Orth, M.; Russo, P. R.; Gershenfeld, N., E-broidery: Design and fabrication of textile-based computing. *IBM Syst. J.* **2000**, *39* (3.4), 840-860.
175. Kiourti, A.; Volakis, J. L., Colorful textile antennas integrated into embroidered logos. *J. Sens. Actuator Netw.* **2015**, *4* (4), 371-377.
176. Quandt, B. M.; Braun, F.; Ferrario, D.; Rossi, R. M.; Scheel-Sailer, A.; Wolf, M.; Bona, G.-L.; Hufenus, R.; Scherer, L. J.; Boesel, L. F., Body-monitoring with photonic textiles: a reflective heartbeat sensor based on polymer optical fibres. *J. R. Soc., Interface* **2017**, *14* (128), 20170060.
177. Buechley, L.; Eisenberg, M., Fabric PCBs, electronic sequins, and socket buttons: techniques for e-textile craft. *Pers. Ubiquit. Comput.* **2009**, *13* (2), 133-150.
178. Wang, S.; Lin, L.; Xie, Y.; Jing, Q.; Niu, S.; Wang, Z. L., Sliding-triboelectric nanogenerators based on in-plane charge-separation mechanism. *Nano Lett.* **2013**, *13* (5), 2226-2233.
179. Seung, W.; Gupta, M. K.; Lee, K. Y.; Shin, K.-S.; Lee, J.-H.; Kim, T. Y.; Kim, S.; Lin, J.; Kim, J. H.; Kim, S.-W., Nanopatterned textile-based wearable triboelectric nanogenerator. *ACS Nano* **2015**, *9* (4), 3501-3509.
180. Zhang, L.; Yu, Y.; Eyer, G. P.; Suo, G.; Kozik, L. A.; Fairbanks, M.; Wang, X.; Andrew, T. L., All-Textile Triboelectric Generator Compatible with Traditional Textile Process. *Adv. Mater. Technol.* **2016**, *1* (9), 1600147.
181. Zhou, T.; Zhang, C.; Han, C. B.; Fan, F. R.; Tang, W.; Wang, Z. L., Woven structured triboelectric nanogenerator for wearable devices. *ACS Appl. Mater. Interfaces* **2014**, *6* (16), 14695-14701.
182. Choi, A. Y.; Lee, C. J.; Park, J.; Kim, D.; Kim, Y. T., Corrugated textile based triboelectric generator for wearable energy harvesting. *Sci. Rep.* **2017**, *7* (1), 1-6.

183. Huang, T.; Wang, C.; Yu, H.; Wang, H.; Zhang, Q.; Zhu, M., Human walking-driven wearable all-fiber triboelectric nanogenerator containing electrospun polyvinylidene fluoride piezoelectric nanofibers. *Nano Energy* **2015**, *14*, 226-235.
184. Cui, N.; Gu, L.; Liu, J.; Bai, S.; Qiu, J.; Fu, J.; Kou, X.; Liu, H.; Qin, Y.; Wang, Z. L., High performance sound driven triboelectric nanogenerator for harvesting noise energy. *Nano Energy* **2015**, *15*, 321-328.
185. Yu, H.; Huang, T.; Lu, M.; Mao, M.; Zhang, Q.; Wang, H., Enhanced power output of an electrospun PVDF/MWCNTs-based nanogenerator by tuning its conductivity. *Nanotechnology* **2013**, *24* (40), 405401.
186. Yang, J.; Chen, Q.; Chen, F.; Zhang, Q.; Wang, K.; Fu, Q., Realizing the full nanofiller enhancement in melt-spun fibers of poly (vinylidene fluoride)/carbon nanotube composites. *Nanotechnology* **2011**, *22* (35), 355707.
187. Wang, S.; Wang, Z. L.; Yang, Y., A one-structure-based hybridized nanogenerator for scavenging mechanical and thermal energies by triboelectric–piezoelectric–pyroelectric effects. *Adv. Mater.* **2016**, *28* (15), 2881-2887.
188. Hadimani, R. L.; Bayramol, D. V.; Sion, N.; Shah, T.; Qian, L.; Shi, S.; Siores, E., Continuous production of piezoelectric PVDF fibre for e-textile applications. *Smart Mater. Struct.* **2013**, *22* (7), 075017.
189. Baji, A.; Mai, Y.-W.; Abtahi, M.; Wong, S.-C.; Liu, Y.; Li, Q., Microstructure development in electrospun carbon nanotube reinforced polyvinylidene fluoride fibers and its influence on tensile strength and dielectric permittivity. *Compos. Sci. Technol.* **2013**, *88*, 1-8.
190. Zheng, J.; Yan, X.; Li, M.-M.; Yu, G.-F.; Zhang, H.-D.; Pisula, W.; He, X.-X.; Duvail, J.-L.; Long, Y.-Z., Electrospun aligned fibrous arrays and twisted ropes: fabrication, mechanical and electrical properties, and application in strain sensors. *Nanoscale research letters* **2015**, *10* (1), 475.
191. Seyedin, S.; Romano, M. S.; Minett, A. I.; Razal, J. M., Towards the knittability of graphene oxide fibres. *Sci. Rep.* **2015**, *5* (1), 1-12.
192. Zeng, X.; Chen, J.; Zhao, J.; Wu, C.; Pan, D.; Pan, N., Investigation the jet stretch in PAN fiber dry-jet wet spinning for PAN-DMSO-H₂O system. *J. Appl. Polym. Sci.* **2009**, *114* (6), 3621-3625.
193. Tascan, M.; Nohut, S., Effects of process parameters on the properties of wet-spun solid PVDF fibers. *Text. Res. J.* **2014**, *84* (20), 2214-2225.
194. Jeong, K.; Kim, D. H.; Chung, Y. S.; Hwang, S. K.; Hwang, H. Y.; Kim, S. S., Effect of processing parameters of the continuous wet spinning system on the crystal phase of PVDF fibers. *J. Appl. Polym. Sci.* **2018**, *135* (3), 45712.

195. Huang, T.; Lu, M.; Yu, H.; Zhang, Q.; Wang, H.; Zhu, M., Enhanced power output of a triboelectric nanogenerator composed of electrospun nanofiber mats doped with graphene oxide. *Sci. Rep.* **2015**, *5*, 13942.
196. Lee, K. Y.; Yoon, H. J.; Jiang, T.; Wen, X.; Seung, W.; Kim, S. W.; Wang, Z. L., Fully packaged self-powered triboelectric pressure sensor using hemispheres-array. *Adv. Energy Mater.* **2016**, *6* (11), 1502566.
197. Wang, X.; Zhang, H.; Dong, L.; Han, X.; Du, W.; Zhai, J.; Pan, C.; Wang, Z. L., Self-powered high-resolution and pressure-sensitive triboelectric sensor matrix for real-time tactile mapping. *Adv. Mater.* **2016**, *28* (15), 2896-2903.
198. Inaba, M.; Hoshino, Y.; Nagasaka, K.; Ninomiya, T.; Kagami, S.; Inoue, H. In *A full-body tactile sensor suit using electrically conductive fabric and strings*, Proceedings of IEEE/RSJ International Conference on Intelligent Robots and Systems. IROS'96, IEEE: 1996; pp 450-457.
199. Sergio, M.; Manaresi, N.; Campi, F.; Canegallo, R.; Tartagni, M.; Guerrieri, R., A dynamically reconfigurable monolithic CMOS pressure sensor for smart fabric. *IEEE J. Solid-State Circuits.* **2003**, *38* (6), 966-975.
200. Holleczech, T.; Rüegg, A.; Harms, H.; Tröster, G. In *Textile pressure sensors for sports applications*, SENSORS, 2010 IEEE, IEEE: 2010; pp 732-737.
201. Parida, K.; Bhavanasi, V.; Kumar, V.; Bendi, R.; Lee, P. S., Self-powered pressure sensor for ultra-wide range pressure detection. *Nano Research* **2017**, *10* (10), 3557-3570.
202. Hoffmann, T.; Eilebrecht, B.; Leonhardt, S., Respiratory monitoring system on the basis of capacitive textile force sensors. *IEEE Sens. J.* **2010**, *11* (5), 1112-1119.
203. Cheng, J.; Sundholm, M.; Zhou, B.; Hirsch, M.; Lukowicz, P., Smart-surface: Large scale textile pressure sensors arrays for activity recognition. *Pervasive Mob. Comput.* **2016**, *30*, 97-112.
204. Meyer, J.; Arnrich, B.; Schumm, J.; Troster, G., Design and modeling of a textile pressure sensor for sitting posture classification. *IEEE Sens. J.* **2010**, *10* (8), 1391-1398.
205. Wang, X.; Que, M.; Chen, M.; Han, X.; Li, X.; Pan, C.; Wang, Z. L., Full Dynamic-Range Pressure Sensor Matrix Based on Optical and Electrical Dual-Mode Sensing. *Adv. Mater.* **2017**, *29* (15), 1605817.
206. Shi, Q.; Wang, H.; Wang, T.; Lee, C., Self-powered liquid triboelectric microfluidic sensor for pressure sensing and finger motion monitoring applications. *Nano Energy* **2016**, *30*, 450-459.
207. Li, T.; Zou, J.; Xing, F.; Zhang, M.; Cao, X.; Wang, N.; Wang, Z. L., From dual-mode triboelectric nanogenerator to smart tactile sensor: a multiplexing design. *ACS Nano* **2017**, *11* (4), 3950-3956.

208. Wang, Z. L.; Chen, J.; Lin, L., Progress in triboelectric nanogenerators as a new energy technology and self-powered sensors. *Energy Environ. Sci.* **2015**, *8* (8), 2250-2282.
209. Guo, H.; Li, T.; Cao, X.; Xiong, J.; Jie, Y.; Willander, M.; Cao, X.; Wang, N.; Wang, Z. L., Self-sterilized flexible single-electrode triboelectric nanogenerator for energy harvesting and dynamic force sensing. *ACS Nano* **2017**, *11* (1), 856-864.
210. Bacarin, T. A.; Sacco, I. C.; Hennig, E. M., Plantar pressure distribution patterns during gait in diabetic neuropathy patients with a history of foot ulcers. *Clinics* **2009**, *64* (2), 113-120.
211. Kimmeskamp, S.; Hennig, E. M., Heel to toe motion characteristics in Parkinson patients during free walking. *Clin.Biomech.* **2001**, *16* (9), 806-812.
212. Fuh, Y. K.; Wang, B. S.; Tsai, C.-Y., Self-Powered Pressure Sensor with fully encapsulated 3D printed wavy substrate and highly-aligned piezoelectric fibers array. *Sci. Rep.* **2017**, *7* (1), 1-7.
213. Nichols, W. W., Clinical measurement of arterial stiffness obtained from noninvasive pressure waveforms. *Am. J. Hypertens.* **2005**, *18* (S1), 3S-10S.
214. Kohara, K.; Tabara, Y.; Oshiumi, A.; Miyawaki, Y.; Kobayashi, T.; Miki, T., Radial augmentation index: a useful and easily obtainable parameter for vascular aging. *Am. J. Hypertens.* **2005**, *18* (S1), 11S-14S.
215. Lai, Y. C.; Deng, J.; Zhang, S. L.; Niu, S.; Guo, H.; Wang, Z. L., Single-thread-based wearable and highly stretchable triboelectric nanogenerators and their applications in cloth-based self-powered human-interactive and biomedical sensing. *Adv. Funct. Mater.* **2017**, *27* (1), 1604462.
216. Foroughi, J.; Spinks, G. M.; Aziz, S.; Mirabedini, A.; Jeiranikhameneh, A.; Wallace, G. G.; Kozlov, M. E.; Baughman, R. H., Knitted carbon-nanotube-sheath/spandex-core elastomeric yarns for artificial muscles and strain sensing. *ACS Nano* **2016**, *10* (10), 9129-9135.
217. Zheng, H.; Zi, Y.; He, X.; Guo, H.; Lai, Y.-C.; Wang, J.; Zhang, S. L.; Wu, C.; Cheng, G.; Wang, Z. L., Concurrent harvesting of ambient energy by hybrid nanogenerators for wearable self-powered systems and active remote sensing. *ACS Appl. Mater. Interfaces* **2018**, *10* (17), 14708-14715.
218. Lowell, J.; Rose-Innes, A., Contact electrification. *Adv. Phys.* **1980**, *29* (6), 947-1023.
219. Kwetkus, B., Particle triboelectrification and its use in the electrostatic separation process. *Particul. Sci. Technol.* **1998**, *16* (1), 55-68.
220. Greason, W. D., Investigation of a test methodology for triboelectrification. *J. Electrostat.* **2000**, *49* (3-4), 245-256.
221. Lovinger, A. J., Ferroelectric polymers. *Science* **1983**, *220* (4602), 1115-1121.
222. Xu, H.; Cheng, Z.-Y.; Olson, D.; Mai, T.; Zhang, Q.; Kavarnos, G., Ferroelectric and electromechanical properties of poly (vinylidene-fluoride-trifluoroethylene-

- chlorotrifluoroethylene) terpolymer. *Appl. Phys. Lett.* **2001**, 78 (16), 2360-2362.
223. Sultana, A.; Ghosh, S. K.; Alam, M. M.; Sadhukhan, P.; Roy, K.; Xie, M.; Bowen, C. R.; Sarkar, S.; Das, S.; Middya, T. R., Methylammonium Lead Iodide Incorporated Poly (vinylidene fluoride) Nanofibers for Flexible Piezoelectric–Pyroelectric Nanogenerator. *ACS Appl. Mater. Interfaces* **2019**, 11 (30), 27279-27287.
 224. Ma, M.; Zhang, Z.; Zhao, Z.; Liao, Q.; Kang, Z.; Gao, F.; Zhao, X.; Zhang, Y., Self-powered flexible antibacterial tactile sensor based on triboelectric-piezoelectric-pyroelectric multi-effect coupling mechanism. *Nano Energy* **2019**, 66, 104105.
 225. Sun, F.-C.; Dongare, A. M.; Asandei, A. D.; Alpay, S. P.; Nakhmanson, S., Temperature dependent structural, elastic, and polar properties of ferroelectric polyvinylidene fluoride (PVDF) and trifluoroethylene (TrFE) copolymers. *J. Mater. Chem. C* **2015**, 3 (32), 8389-8396.
 226. Lang, S. B., Static and dynamic pyroelectric coefficients of polyvinylidene fluoride over a 90–370 K temperature range. *J. Appl. Phys.* **1979**, 50 (8), 5554-5556.
 227. Fukada, E.; Furukawa, T., Piezoelectricity and ferroelectricity in polyvinylidene fluoride. *Ultrasonics* **1981**, 19 (1), 31-39.
 228. Lin, M.-F.; Xiong, J.; Wang, J.; Parida, K.; Lee, P. S., Core-shell nanofiber mats for tactile pressure sensor and nanogenerator applications. *Nano Energy* **2018**, 44, 248-255.
 229. Garcia, C.; Trendafilova, I.; de Villoria, R. G.; del Rio, J. S., Self-powered pressure sensor based on the triboelectric effect and its analysis using dynamic mechanical analysis. *Nano Energy* **2018**, 50, 401-409.
 230. Fan, Y. J.; Meng, X. S.; Li, H. Y.; Kuang, S. Y.; Zhang, L.; Wu, Y.; Wang, Z. L.; Zhu, G., Stretchable Porous Carbon Nanotube-Elastomer Hybrid Nanocomposite for Harvesting Mechanical Energy. *Adv. Mater.* **2017**, 29 (2), 1603115.
 231. Jiang, X.-Z.; Sun, Y.-J.; Fan, Z.; Zhang, T.-Y., Integrated flexible, waterproof, transparent, and self-powered tactile sensing panel. *ACS Nano* **2016**, 10 (8), 7696-7704.
 232. Yuan, Z.; Zhou, T.; Yin, Y.; Cao, R.; Li, C.; Wang, Z. L., Transparent and flexible triboelectric sensing array for touch security applications. *ACS Nano* **2017**, 11 (8), 8364-8369.
 233. Zhu, G.; Yang, W. Q.; Zhang, T.; Jing, Q.; Chen, J.; Zhou, Y. S.; Bai, P.; Wang, Z. L., Self-powered, ultrasensitive, flexible tactile sensors based on contact electrification. *Nano Lett.* **2014**, 14 (6), 3208-3213.
 234. Lai, Y. C.; Deng, J.; Liu, R.; Hsiao, Y. C.; Zhang, S. L.; Peng, W.; Wu, H. M.; Wang, X.; Wang, Z. L., Actively Perceiving and Responsive Soft Robots Enabled by Self-Powered, Highly Extensible, and Highly Sensitive Triboelectric Proximity-and Pressure-Sensing Skins. *Adv. Mater.* **2018**, 30 (28), 1801114.
 235. Liu, Z.; Zhao, Z.; Zeng, X.; Fu, X.; Hu, Y., Expandable microsphere-based triboelectric

- nanogenerators as ultrasensitive pressure sensors for respiratory and pulse monitoring. *Nano Energy* **2019**, *59*, 295-301.
236. Hou, C.; Wang, H.; Zhang, Q.; Li, Y.; Zhu, M., Highly Conductive, Flexible, and Compressible All-Graphene Passive Electronic Skin for Sensing Human Touch. *Adv. Mater.* **2014**, *26* (29), 5018-5024.
 237. Ma, Y.; Zheng, Q.; Liu, Y.; Shi, B.; Xue, X.; Ji, W.; Liu, Z.; Jin, Y.; Zou, Y.; An, Z., Self-powered, one-stop, and multifunctional implantable triboelectric active sensor for real-time biomedical monitoring. *Nano Lett.* **2016**, *16* (10), 6042-6051.
 238. Chen, J.; Guo, H.; Wu, Z.; Xu, G.; Zi, Y.; Hu, C.; Wang, Z. L., Actuation and sensor integrated self-powered cantilever system based on TENG technology. *Nano Energy* **2019**, *64*, 103920.
 239. Ha, M.; Park, J.; Lee, Y.; Ko, H., Triboelectric generators and sensors for self-powered wearable electronics. *ACS Nano* **2015**, *9* (4), 3421-3427.
 240. Pu, X.; Liu, M.; Chen, X.; Sun, J.; Du, C.; Zhang, Y.; Zhai, J.; Hu, W.; Wang, Z. L., Ulstretchable, transparent triboelectric nanogenerator as electronic skin for biomechanical energy harvesting and tactile sensing. *Sci. Adv.* **2017**, *3* (5), e1700015.
 241. Bai, P.; Zhu, G.; Jing, Q.; Yang, J.; Chen, J.; Su, Y.; Ma, J.; Zhang, G.; Wang, Z. L., Membrane-based self-powered triboelectric sensors for pressure change detection and its uses in security surveillance and healthcare monitoring. *Adv. Funct. Mater.* **2014**, *24* (37), 5807-5813.
 242. Song, G.; Kim, Y.; Yu, S.; Kim, M.-O.; Park, S.-H.; Cho, S. M.; Velusamy, D. B.; Cho, S. H.; Kim, K. L.; Kim, J., Molecularly engineered surface triboelectric nanogenerator by self-assembled monolayers (METS). *Chem. Mater.* **2015**, *27* (13), 4749-4755.
 243. Jang, D.; Kim, Y.; Kim, T. Y.; Koh, K.; Jeong, U.; Cho, J., Force-assembled triboelectric nanogenerator with high-humidity-resistant electricity generation using hierarchical surface morphology. *Nano Energy* **2016**, *20*, 283-293.
 244. Feng, Y.; Zheng, Y.; Ma, S.; Wang, D.; Zhou, F.; Liu, W., High output polypropylene nanowire array triboelectric nanogenerator through surface structural control and chemical modification. *Nano Energy* **2016**, *19*, 48-57.
 245. He, X.; Guo, H.; Yue, X.; Gao, J.; Xi, Y.; Hu, C., Improving energy conversion efficiency for triboelectric nanogenerator with capacitor structure by maximizing surface charge density. *Nanoscale* **2015**, *7* (5), 1896-1903.
 246. Wang, J.; Wu, C.; Dai, Y.; Zhao, Z.; Wang, A.; Zhang, T.; Wang, Z. L., Achieving ultrahigh triboelectric charge density for efficient energy harvesting. *Nat. Commun.* **2017**, *8* (1), 1-8.
 247. Chen, S.-N.; Chen, C.-H.; Lin, Z.-H.; Tsao, Y.-H.; Liu, C.-P., On enhancing capability of tribocharge transfer of ZnO nanorod arrays by Sb doping for anomalous output performance

- improvement of triboelectric nanogenerators. *Nano Energy* **2018**, *45*, 311-318.
248. Wang, Y.; Duan, J.; Yang, X.; Liu, L.; Zhao, L.; Tang, Q., The unique dielectricity of inorganic perovskites toward high-performance triboelectric nanogenerators. *Nano Energy* **2020**, *69*, 104418.
 249. Lin, Z.-H.; Xie, Y.; Yang, Y.; Wang, S.; Zhu, G.; Wang, Z. L., Enhanced triboelectric nanogenerators and triboelectric nanosensor using chemically modified TiO₂ nanomaterials. *ACS Nano* **2013**, *7* (5), 4554-4560.
 250. Park, J.; Lee, Y.; Barbee, M. H.; Cho, S.; Cho, S.; Shanker, R.; Kim, J.; Myoung, J.; Kim, M. P.; Baig, C., A Hierarchical Nanoparticle-in-Micropore Architecture for Enhanced Mechanosensitivity and Stretchability in Mechanochromic Electronic Skins. *Adv. Mater.* **2019**, *31* (25), 1808148.
 251. Mao, Y.; Zhao, P.; McConohy, G.; Yang, H.; Tong, Y.; Wang, X., Sponge-like piezoelectric polymer films for scalable and integratable nanogenerators and self-powered electronic systems. *Adv. Energy Mater.* **2014**, *4* (7), 1301624.
 252. Li, J.; Inukai, K.; Takahashi, Y.; Shin, W., Synthesis and size control of monodispersed BaTiO₃-PVP nanoparticles. *J. Asian Ceram. Soc.* **2016**, *4* (4), 394-402.
 253. Li, J.; Inukai, K.; Takahashi, Y.; Tsuruta, A.; Shin, W., Thin film coating with highly dispersible barium titanate-polyvinylpyrrolidone nanoparticles. *Materials* **2018**, *11* (5), 712.
 254. Kwon, Y. H.; Shin, S.-H.; Kim, Y.-H.; Jung, J.-Y.; Lee, M. H.; Nah, J., Triboelectric contact surface charge modulation and piezoelectric charge inducement using polarized composite thin film for performance enhancement of triboelectric generators. *Nano Energy* **2016**, *25*, 225-231.
 255. Sharma, M.; Quamara, J. K.; Gaur, A., Behaviour of multiphase PVDF in (1- x) PVDF/(x) BaTiO₃ nanocomposite films: structural, optical, dielectric and ferroelectric properties. *J. Mater. Sci. Mater. Electron.* **2018**, *29* (13), 10875-10884.
 256. Mayeen, A.; Kala, M.; Jayalakshmy, M.; Thomas, S.; Rouxel, D.; Philip, J.; Bhowmik, R.; Kalarikkal, N., Dopamine functionalization of BaTiO₃: an effective strategy for the enhancement of electrical, magnetoelectric and thermal properties of BaTiO₃-PVDF-TrFE nanocomposites. *Dalton Trans.* **2018**, *47* (6), 2039-2051.
 257. Baer, E.; Zhu, L., 50th anniversary perspective: dielectric phenomena in polymers and multilayered dielectric films. *Macromolecules* **2017**, *50* (6), 2239-2256.
 258. Peng, J.; Kang, S. D.; Snyder, G. J., Optimization principles and the figure of merit for triboelectric generators. *Sci. Adv.* **2017**, *3* (12), eaap8576.
 259. Zhu, L., Exploring strategies for high dielectric constant and low loss polymer dielectrics. *J. Phys. Chem. Lett.* **2014**, *5* (21), 3677-3687.

260. Shen, Z.-H.; Wang, J.-J.; Zhang, X.; Lin, Y.; Nan, C.-W.; Chen, L.-Q.; Shen, Y., Space charge effects on the dielectric response of polymer nanocomposites. *Appl. Phys. Lett.* **2017**, *111* (9), 092901.
261. Zou, J.; Zhang, M.; Huang, J.; Bian, J.; Jie, Y.; Willander, M.; Cao, X.; Wang, N.; Wang, Z. L., Coupled supercapacitor and triboelectric nanogenerator boost biomimetic pressure sensor. *Adv. Energy Mater.* **2018**, *8* (10), 1702671.
262. Rasel, M. S.; Maharjan, P.; Salauddin, M.; Rahman, M. T.; Cho, H. O.; Kim, J. W.; Park, J. Y., An impedance tunable and highly efficient triboelectric nanogenerator for large-scale, ultra-sensitive pressure sensing applications. *Nano Energy* **2018**, *49*, 603-613.
263. Tcho, I.-W.; Kim, W.-G.; Jeon, S.-B.; Park, S.-J.; Lee, B. J.; Bae, H.-K.; Kim, D.; Choi, Y.-K., Surface structural analysis of a friction layer for a triboelectric nanogenerator. *Nano Energy* **2017**, *42*, 34-42.
264. Li, S.-X.; Xia, H.; Xu, Y.-S.; Lv, C.; Wang, G.; Dai, Y.-Z.; Sun, H.-B., Gold nanoparticle densely packed micro/nanowire-based pressure sensors for human motion monitoring and physiological signal detection. *Nanoscale* **2019**, *11* (11), 4925-4932.
265. Huang, C.-M.; Chang, H.-C.; Kao, S.-T.; Li, T.-C.; Wei, C.-C.; Chen, C.; Liao, Y.-T.; Chen, F.-J., Radial pressure pulse and heart rate variability in heat-and cold-stressed humans. *Evid. Based Complement. Alternat. Med.* **2011**, 2011.
266. Hirata, K.; Yaginuma, T.; O'Rourke, M. F.; Kawakami, M., Age-related changes in carotid artery flow and pressure pulses: possible implications for cerebral microvascular disease. *Stroke* **2006**, *37* (10), 2552-2556.
267. Park, J.; Kim, J.; Hong, J.; Lee, H.; Lee, Y.; Cho, S.; Kim, S.-W.; Kim, J. J.; Kim, S. Y.; Ko, H., Tailoring force sensitivity and selectivity by microstructure engineering of multidirectional electronic skins. *NPG Asia Mater.* **2018**, *10* (4), 163-176.

*Chapter 2 is reproduced in part with permission of “Sewing machine stitching of polyvinylidene fluoride fibers: programmable textile patterns for wearable triboelectric sensors, *J. Mater. Chem. A*, **2018**, *6*, 22879-22888. DOI: 10.1039/c8ta08485h”. Copyright 2018 Royal Society of Chemistry.

*Chapter 3 is reproduced in part with permission of “Self-powered triboelectric/pyroelectric multimodal sensors with enhanced performances and decoupled multiple stimuli, *Nano Energy* **2020**, *72*, 104671. DOI: 10.1016/j.nanoen.2020.104671”. Copyright 2020 Elsevier Ltd.

*Chapter 4 is reproduced in part with permission of “Ferroelectric multilayer nanocomposites with polarization and stress concentration structures for enhanced triboelectric performances, *ACS Nano*, **2020**, *14*, 7101–7110. DOI: 10.1021/acsnano.0c01865”. Copyright 2020 American Chemical Society.

Appendix A: List of achievements

The results of this dissertation have been published in: (†: equal contribution)

1. **Young-Eun Shin**, Jeong-Eun Lee, Yoojeong Park, Sang-Ha Hwang, Han Gi Chae, and Hyunhyub Ko, Sewing machine stitching of polyvinylidene fluoride fibers: programmable textile patterns for wearable triboelectric sensors, *J. Mater. Chem. A*, **2018**, 6, 22879-22888. DOI: 10.1039/c8ta08485h. Copyright 2018 Royal Society of Chemistry.
2. **Young-Eun Shin**, So-Dam Sohn, Huijun Han, Yoojeong Park, Hyung-Joon Shin, Hyunhyub Ko; Self-powered triboelectric/pyroelectric multimodal sensors with enhanced performances and decoupled multiple stimuli, *Nano Energy* **2020**, 72, 104671. DOI: 10.1016/j.nanoen.2020.104671. Copyright 2020 Elsevier Ltd.
3. Yoojeong Park, † **Young-Eun Shin**, † Jonghwa Park, Youngsu Lee, Minsoo P. Kim, Young-Ryul Kim, Sangyun Na, Sujoy Kumar Ghosh and Hyunhyub Ko, Ferroelectric multilayer nanocomposites with polarization and stress concentration structures for enhanced triboelectric performances, *ACS Nano*, **2020**, 14, 7101–7110. DOI: 10.1021/acsnano.0c01865. Copyright 2020 American Chemical Society. (†These authors contributed equally to this work.)

The other related results have been published in:

1. Dongwoo Kang, **Young-Eun Shin**, Hye Jin Jo, Hyunhyub Ko and Hyeon Suk Shin, Mechanical properties of poly(dopamine)-coated graphene oxide and poly(vinyl alcohol) composite fibers coated with reduced graphene oxide and their use for piezoresistive sensing, *Part. Part. Syst. Charact.* **2017**, 34, 1600382. DOI: 10.1002/ppsc.201600382.
2. Youngoh Lee, Jonghwa Park, Soowon Cho, **Young-Eun Shin**, Hochan Lee, Jinyoung Kim, Jinyoung Myoung, Seungse Cho, Saewon Kang, Chunggi Baig, Hyunhyub Ko, Flexible ferroelectric sensors with ultrahigh pressure sensitivity and linear response over exceptionally broad pressure range, *ACS Nano*, **2018**, 12, 4045-4054. DOI: 10.1021/acsnano.8b01805.
3. Jung-Eun Lee, Youngho Eom, **Young-Eun Shin**, Sang-Ha Hwang, Hyunhyub Ko, Han Gi Chae, Effect of interfacial interaction on the conformational variation of poly(vinylidene fluoride) (PVDF) chains in PVDF/graphene oxide (GO) nanocomposite fibers and corresponding mechanical properties, *ACS Appl. Mater. Inter.* **2019**, 11, 13665-13675. DOI: 10.1021/acsam.8b22586.

Conference Presentation:

International Conferences

1. **Young-Eun Shin**, Jeong-Eun Lee, Yoojeong Park, Han Gi Chae, and Hyunhyub Ko, “Triboelectric Wearable Sensors Based on Sewing Machine Stitching of Polyvinylidene Fluoride Fibers”, Poster Presentation, *European Materials Research Society (E-MRS 2018)*, Strasbourg, France.
2. **Young-Eun Shin**, So-Dam Sohn, Huijun Han, Hyung-Joon Shin, and Hyunhyub Ko, “Identical Material-Based Self-Powered Triboelectric Sensors *via* Ferroelectric Polarization”, Poster Presentation, *Materials Research Society (MRS 2019)*, Boston, USA.

Domestic Conferences

1. **Young-Eun Shin**, Jeong-Eun Lee, Yoojeong Park, Han Gi Chae, and Hyunhyub Ko, “Triboelectric Wearable Sensors Based on Sewing Machine Stitching of Polyvinylidene Fluoride Fibers”, Poster Presentation, *The Polymer Society of Korea (PSK 2018)*, Daejeon, Korea
2. **Young-Eun Shin**, Jeong-Eun Lee, Yoojeong Park, Han Gi Chae, and Hyunhyub Ko, “Triboelectric Wearable Sensors Based on Sewing Machine Stitching of Polyvinylidene Fluoride Fibers”, Poster Presentation, *International Union of Materials Research Societies-International Conference on Electronic Materials (IUMRS-ICEM 2018)*, Daejeon, Korea.
3. **Young-Eun Shin**, Jeong-Eun Lee, Yoojeong Park, Han Gi Chae, and Hyunhyub Ko, “Self-powered Triboelectric Sensors Based on Sewing Machine Stitching of Polyvinylidene Fluoride Fibers”, Poster Presentation, *The Korean Society for Composite Materials (KSCM 2019)*, Yeosu, Korea.
4. **Young-Eun Shin**, Jeong-Eun Lee, Yoojeong Park, Han Gi Chae, and Hyunhyub Ko, “Textile Patterns for Wearable Triboelectric Sensors Based on Sewing Machine Stitching of Polyvinylidene Fluoride Fibers”, Poster Presentation, *The Polymer Society of Korea (PSK 2019)*, Busan, Korea.

Acknowledgements

It is a great honor to successfully complete my Ph.D. course. This work would not have been possible without the guidance, encouragement, and support of many people, and I would like to express my sincere appreciation in this page.

First of all, I would like to express the deepest appreciation to Professor Hyunhyub Ko who expertly guided me through my graduate education. It has been a great honor to work under his supervision. I have learned a lot of things such as research ethics, scientific insight, and problem solving capability. Above all, he led me to be an independent researcher. Thanks to his help, support and patient, I have completed my doctoral course, successfully. In addition, I would like to thank my committee members, Prof. Seok Ju Kang, Prof. Han Gi Chae, Prof. Chang Young Lee, and Prof. Moon Kee Choi, *Ulsan National Institute of Science and Technology (UNIST)*, for their sincere encouragement and constructive reviews.

Furthermore, I would like to express my appreciation to Dr. Jiwon Lee, Dr. Jonghwa Park, Dr. Saewon Kang, Dr. Seungyoung Park, Dr. Youngoh Lee, and Seungse Cho, *previous and current lab leaders in our lab*. Thanks to their effort and dedication to our FNL (Functional Nanomaterials and Devices Laboratory), I was able to concentrate on my research. In addition, I would like to thank all our lab members, Dr. Minsoo Kim, Ayoung Choe, Youngsu Lee, Jeonghee Yeom, Young-Ryul Kim, Jinyoung Kim, Donghee Kang, Yeju Kwon, Hyejin Lee, Seungjae Lee, Yujung Ko, Geonyoung Jeong. With their great assistance, I have successfully completed my work in past years. Especially, I am grateful to Yoojeong Park, Dr. Sujoy Kumar Ghosh, Sangyun Na, and Yong-Jin Park for their considerable support as my team members. I wish all of you the best of luck in your endeavors.

Lastly, I appreciate my parents whose endless love and considerable trust help me to successfully complete my Ph.D. course. Their support gives me strength in difficult times. Moreover, I am grateful to my younger sister and brother who have always given me energy so I could complete my work.

Again, I would like to say thank you to all people who have encouraged and supported me until now.

